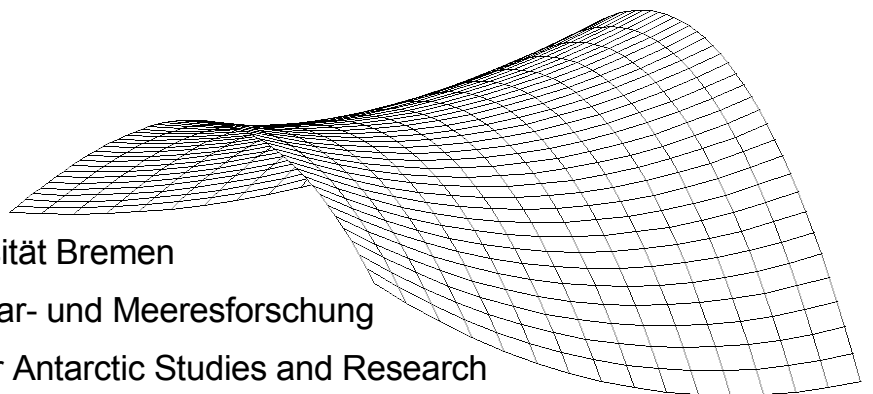# Surface Topography and Massflux of the Antarctic Ice Sheet in Dronning Maud Land, Based on Differential SAR Interferometry

Reinhard Drews

Fakultät für Physik der Universität Bremen

Alfred-Wegener-Institut für Polar- und Meeresforschung

Gateway Antarctica, Center for Antarctic Studies and Research

Universität Bremen

Fakultät für Physik

Diplomarbeit/Diploma Thesis:

Surface Topography and Massflux of the Antarctic Ice Sheet in Dronning Maud Land, Based on Differential SAR Interferometry

Author:
Reinhard Drews

Supervisor:
Dr. Wolfgang Rack

Referee:
Prof. Dr. P. Lemke
Prof. Dr. J. Notholt

October 20, 2007

Contents

7   Summary and future prospects   **82**

A   Appendix   **84**

Acknowledgments   **88**

List of Figures

1 Introduction

The ice sheet covering Antarctica, *the opposite of the Arctic*, is of high interest in recent debates of environmental sciences. With its circumference of about 1.3 times the size of Europe, it holds approximately 90 % of the world's ice in total and thus plays a crucial role in all questions concerning the cryosphere. With the ice sheet's high reflectivity, it influences the worlds radiation budget significantly, and the input of fresh water into the ocean serves as a booster for oceanic circulation and a potential change in sea level. Since ice particles have a long residence time in the ice sheet, a lot of information is archived in Antarctica. Ice cores show the incremental build up of annual layers through snow accumulation. It is possible to derive spatial and seasonal variations in the accumulation pattern. The analysis of encapsulated air bubbles enables the reconstruction of atmospheric composition in the past. This is done through the determination of isotope ratios from oxygen or hydrogen, and the quantification of trace gases as carbon dioxide or methane. For this process the dating of the different depth layers is crucial. Thereby the age-depth relation not only depends on a varying accumulation rate, but also on the surrounding flow field which transports the ice from the pole outwards. It is especially observable at outlet glaciers on the coast.

This leads to the interesting parameter of the overall mass balance, which addresses the question if the flow of ice formed through accumulation in the inland matches the outflow of ice on the coast. A positive or a negative mass balance leads to an increase or decrease of the overall ice stored in Antarctica. This influences the earth's radiation budget, as a change in ice coverage alters the overall albedo. A non zero mass balance is also followed by an altered fresh water input into the ocean, which stimulates circulation patterns and is also connected with the promotional sea level rise.

Parameters of the mass balance are velocity fields and ice thickness models. Closely related to velocity fields are elevation models which determine, together with the bedrock topography, the characteristic of the flow field. A huge problem in measuring these parameters is the inaccessibility of the Antarctic continent. All campaigns are accompanied by an extreme logistic effort which boarders their spatial coverage. Evaluating ground based experiments often faces the problem of interpolating over large unknown territory, considering the large extent of Antarctica, and even airborne campaigns are restricted to the larger vicinity of research stations for security reasons and in order to get fuel.

This is why a satellite based approach can be a valuable amendment. With its high

resolution it offers basically continuous and large scale information about surface as well as atmospheric conditions, and it is not necessarily bounded to the summer season for its operation. A good example is the Antarctic mapping mission with the satellite Radarsat-1: in less than three weeks the first map of the complete Antarctic continent was recorded at a 25 m resolution.

The problems when using satellites become evident, if quantitative data needs to be extracted. The complex interaction of snow with electromagnetic waves aggravates the interpretation of the images, and without using an altimeter it is hard to get height information from a single image. If an altimeter is used, again the interpolation between the different tracks blurs smaller scales undulations. This problem is addressed by an interferometric procedure, where two acquisitions are used to derived a digital elevation model with a very high spatial resolution. If the scenes are acquired one after the other, it is also possible to map changes on the surface. So high resolution digital elevation models as well as flowfields can be the valuable output of this approach.

Satellite based Radar Interferometry · In a physical context, interference describes the interaction of waves. Depending on their relative cycles, or phases, they can attenuate or amplify each other. It is a common physical phenomena, seen in every day life for instance in the appearance of rainbows.

In satellite based interferometry a special kind of radar, a SAR, is installed on a satellite and emits and records electromagnetic waves. It penetrates clouds and can be used during day or night time. In the processing, two acquisitions of the same scenes are evaluated with respect to their amplitude as well as their relative phase. Thereby it is decisive, that the scenes are recorded at a slightly differing geometry so that the change of phase can not only be attributed to displacement but also to topography.

The used wavelength is in the order of cm and so relative changes in phase below the cm level have to be resolved. This marks the crux of this approach. On the one hand it offers an extreme sensitivity, on the other hand it calls for an extensive and very accurate signal processing. If this can be achieved, the findings are remarkable: The motion of glaciers is in the order of 0.2 - 1 m a day and so well in the resolvable cm domain and digital elevation models can be derived in a higher resolution compared to the altimeter based procedure. In the end, height models and flowfields can be established over hundreds of kilometers at a resolution of approximately (50x50) m. For the signal processing ground control points are needed, and since real control points a sparse, a multi sensor approach combines the advantageous of a laser altimeters and a SAR.

The so derived displacement fields are a unique representation for glacier dynamics as no other method offers such a continuous and precise mapping of motion. In combination with ice thickness measurements, a local mass balance of the scene can be determined. On the other hand, only a limited amount of suitable satellite data is available and no long term time series exist. Therefore it is important to evaluated the accuracy of the procedure if different sets of data are to be compared: In this study, data from the

European Remote Sensing satellites from 1994 to 1996 is being used. In the near future, the launch of the CryoSAT 2 satellite will hopefully offer the possibility for comparison so that potential changes in the dynamics can be detected.

For the derivation of flowfields, a precise height model is needed. In theory it is possible to use external height models but since the currently available models show large deviations in coastal areas it was chosen to first focus on a derivation of a new height model. This height model then serves as an input for the derivation of flowfields. Seen as a single entity, the height model also carries valuable geophysical information. It can be used for the planning of traverse routes and also as a starting condition of a theoretical ice flow model. Also a potential comparison with the CryoSAT model could reveal changes in the surface topography. This could be useful to map changes of accumulation patterns, but therefore first the accuracy of the model needs to be determined so that it is clear to which order of magnitude such a comparison is reasonable.

The goals of this study · The goals of the thesis can be set as the following:

- Gain a thorough understanding of the method
- Evaluate the main steps of the processing chain
- Assign external and internal error sources
- Derive a larger scale DEM and the corresponding motion maps
- Evaluate the geophysical product and demonstrate its capabilities

The feasibility of such an interferometric approach in Antarctica has been shown in other studies (for example [BS05]) and commercial software packages exist for this kind of application. However, there is no example of a large scale DEM generation that comprises several tracks and frames, and no study has been performed in the vicinity of the German overwintering station Neumayer.

In a first step it is important to gain a good understanding of the method, so that it is possible to isolate critical parameters and their role in the processing chain. Thereby the question, if internal errors are introduced through the processing and if they can be separated from external error sources as for example atmospheric contributions, will be pursued. The goal is to develop an understanding on which critical parameters the DEM 's quality depends. In the end, the geophysical product will be evaluated and it will be shown how it can be used for a mass balance estimation and, as an interesting result, how it can also be used for the estimation of accumulation rates.

Geographical Setting · The region of interest is situated in north-western part of Antarctica. It is within the Dronning Maud Land (DML) area, which was named after
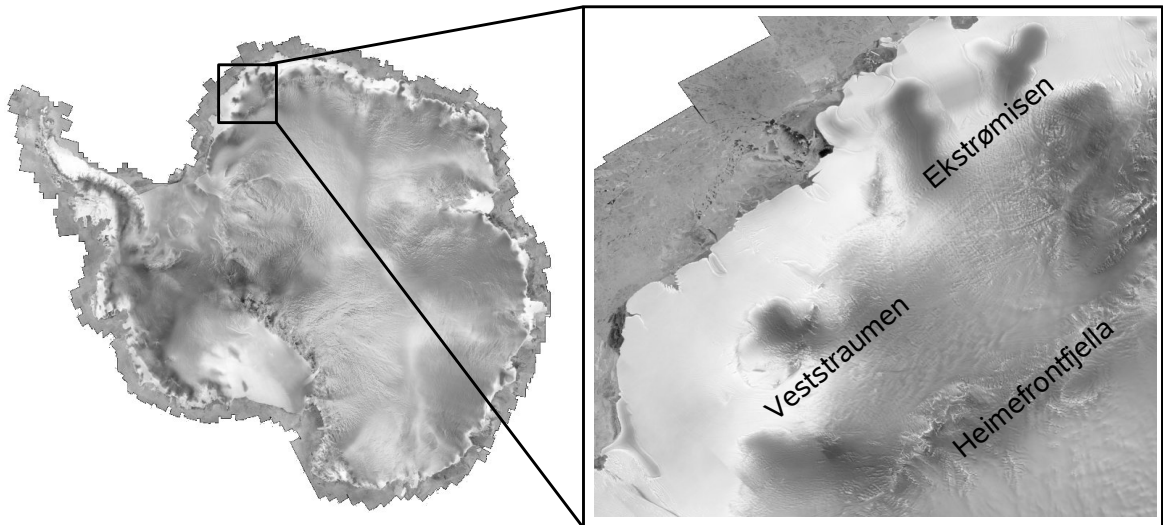
Figure 1.1: The geographical setting within the Dronning Maud Land area. The main ice flow originates in the mountain range Heimefrontfjella and migrates to outlet glaciers like the Veststraumen and to ice shelves like the Ekstrømisen.

the norwegian queen Maud. It hosts a number of research stations, amongst those the german station Neumayer, which is built on the ice shelf of the Ekstrømisen. It is claimed as a dependent territory by the Norwegian government, but at the same time it is part of the Antarctic Treaty system which does not recognize such claims by sovereign states. The DEM will be bounded in between 5 °W and 71°S as well as 15 °W and 75.5° S. It contains as the main outlet glaciers the Ekstrømisen on its eastern boundary and the Veststraumen on its western side. The main ice flow originates from the mountain range Heimefrontfjella towards the coast.

The genesis of this project · This master thesis is a joint project between the Alfred-Wegener Institute (AWI) of Polar and Marine Research in Bremerhaven, Germany with the Gateway Antarctica (GA) in Christchurch, New Zealand. It included a six month internship in New Zealand and is supervised by Dr. W. Rack in Christchurch as well as D. Steinhage in Bremerhaven. The overall project is supported by the Glaciology group in Bremerhaven and generally under the leadership of Prof. Dr. P. Lemke (AWI).
The processing of the data and considerations on possible internal errors are conducted in New Zealand, in order to benefit from the available know-how of SAR interferometry. An appreciated side effect is to gather experience on glaciers in New Zealand. The evaluation of the geophysical product is carried out in Bremerhaven, where external data like GPS measurements and ice thickness models as well as accumulation maps for the region of interest are being compiled.

2 Datasets

This section provides a short overview of the data sets that were used in this study. Thereby the images of the ERS-satellites were combined with IceSAT's laser altimeter to derive the DEM. For mass balance considerations, an ice thickness model derived from an airborne ice penetrating radar was used. Data from the Radarsat Antarctic Mapping Project was used for comparison and visualization.

2.1 ERS – satellites

The ERS-1 satellite was launched in July 1991 from the European Space Agency (ESA). It carried, amongst others, a radar altimeter and an active microwave instrument (AMI) which combines the functions of a SAR and a wind scatterometer. The latter is used to measure wind speed and direction at the sea surface but is not of further concern in this study.

The radar altimeter works with a frequency of 13.8 GHz, pointing directly downwards to the nadir point. It is designed to measure the satellite's height above ground. It can operate in two modes (ocean or ice). In ocean mode, it measures parameters like the sea surface elevation above a certain reference ellipsoid, wave heights or tides. In ice mode, it contributed to the creation of the RAMP [HL01] and JBL97 [JB01] DEMs of Antarctica. The antenna diameter is 1.2 m.

The SAR within the AMI can be operated in two modes as well (image and wave). In wave mode, the SAR acquires small scale images of (5x5) km, whereas in the image mode longer strips with a width of about 100 km are recorded. In this mode, the amount of the received data is too large to be stored onboard, and the image mode is thus limited to the availability of ground stations where the signal can be transmitted in real time. Here, only scenes acquired in image mode are considered.

The SAR works in a side looking geometry, with a look angle of $\gamma = 23°$ at the scene center (see figure 4.2). The ground range resolution is 20 m across track and 5 m along track. ERS-1 circles the earth in about 100 min., and a complete coverage of the Earth's surface is possible in three days. Since spring 2000 ERS-1 is out of order. It flew in several different missions, mostly characterized by different repeat pass cycles. Of special

interest here are the two ice phases:

· Ice Phase 1: 28 - Dec. 1991 to 03 - Mar. 1992

· Ice Phase 2: 23 - Dec. 1993 to 10 - Apr. 1994

During the Ice Phase 1 and 2 the repeat pass cycle was 3 days. This is a good time period for repeat pass interferometry, as the conditions for coherence over ice (see section 4.2) are relatively often met.
ERS-2 was launched in April 1995, essentially as a twin of ERS-1, and is currently still in use. Additionally, it carries an instrument for atmospheric ozone research, but this is not of further concern here. In the so called tandem mission, ERS-2 was setup to follow ERS-1's orbit with a 1 day time delay. Compared to ERS-1's ice phase, the repeat pass interval is 3 times shorter, which often leads to a better coherence.The tandem mission started on 17 - Aug. 1995 and lasted for 12 months.
All interferograms used in this study were derived from the tandem mission and from Ice Phase 2. All used ERS SAR image frames are shown in figure 2.1.

2.2 IceSAT

The ice, cloud and land elevation satellite IceSAT was launched on 12 - Jan. 2003 by the National Aeronautics and Space Administration (NASA). The most important instrument on board is the Geoscience Laser Altimeter System (GLAS). It is designed to measure ice-sheet elevation and temporal changes in topography via repeat pass. Also it detects clouds and other atmospheric properties. The laser can operate at two wavelengths of 1064 and 532 nm (infrared and green). The latter is used for the detection of aerosols and clouds, whereas infrared is used for the elevation data. The accuracy is in the order of cm. It flies at a height of 600 km with a 183 day repeat pattern. The footprint is approximately 70 m with a a spacing of 172 m along track. The IceSAT tracks cover all of Antarctica, but the track spacing decreases towards the coast.
The data is distributed by the National Snow and Ice Data Center at the University of Colorado (US). There, the GLAS/IceSAT DEM [JD07] of Antarctica, with a 500 m grid cell spacing was released in 2007. The main problem of processing the data for ice sheet elevation is to account for clouds in the area, which significantly influence the laster altimeter. The data used in this study was prefiltered by the NSDIC, and finally processed by C. Wesche (AWI).

2.3 Radio Echo Sounding

The knowledge of ice thickness is essential, amongst others, for ice-dynamic modeling and mass balance considerations. At the AWI, the system, which was developed by TU Hamburg-Harburg and 'Aerodata Flugmeßtechnik' in Braunschweig, is installed on the fixed wing aircraft Polar 2. In the upcoming season of 2007 a new plane, the Polar 5 will be used. The radar signal (150 MHz) can operate with different bursts of 60 and 600 ns and records 20 traces per second. The depth resolution is 50 to 500 m respectively. Because of the higher resolution, the shorter bursts are preferred, and longer bursts are only used if the bedrock is not reached otherwise. The short bursts are also preferably used to resolve internal layering. The maximum penetration depth is 4 km. A more detailed description of the RES can be found at [UN05]. The digital data processing of the ice thickness map was done by D. Steinhage (AWI). The spatial resolution depends at first on the availability of flight tracks in the region of interest. The coverage is most dense on the Ekstrømisen close to the Neumayer station. It becomes more sparse towards the Veststraumen.
Data from the Polar2 radar altimeter, as well as from the RES itself, can be used to derive DEMs. Especially in areas with good spatial coverage and in combination with external data, such as IceSAT or GPS, it is possible to derive precise DEMs. This is currently done by C. Wesche in the vicinity of Neumayer ([CW07]). However, profiles further away are sparse.

2.4 Radarsat Antarctic Mapping Project

This project is based on the acquisitions from the canadian satellite RADARSAT-1. It is a collaborative project of the Canadian Space Agency together with the NASA, the Byrd Polar Resarch Center (Vexcel Corporation), the Alaska Satellite Facility , and the Jet Propulsion Laboratory.
The main instrument is a SAR as well. Unlike the ERS satellites, the SAR operates in a right looking and a left looking geometry. This enables a coverage of the complete Antarctic continent with high resolution SAR images. The first mission (AMM-1) started on September 9 in 1997 and ended on October 20 of the same year. The outcome is the first complete radar mosaic of Antarctica. It revealed until then unknown variations of large-scale radar brightness and detailed surface features particularly in coastal areas. As an interferometric approach was proven to be feasible, the Antarctic Mapping Mission-2 (AMM-2) was started in fall 2000. Its goal was to remap the coastal areas with an interferometric background, similar to the objectives of the respective ERS missions. At this stage, the south looking mode of the SAR antenna was not used, due to concerns

of the spacecraft's condition. This is why the AMM-2 phase is also referred to as the modified Antarctic mapping mission (MAMM). In this study, mainly the mosaic from AMM-1 is used for visualization purposes. Figure 2.1 displays the processed tracks and frames from the ERS satellites with the mosaic of the AMM-1 in the background.
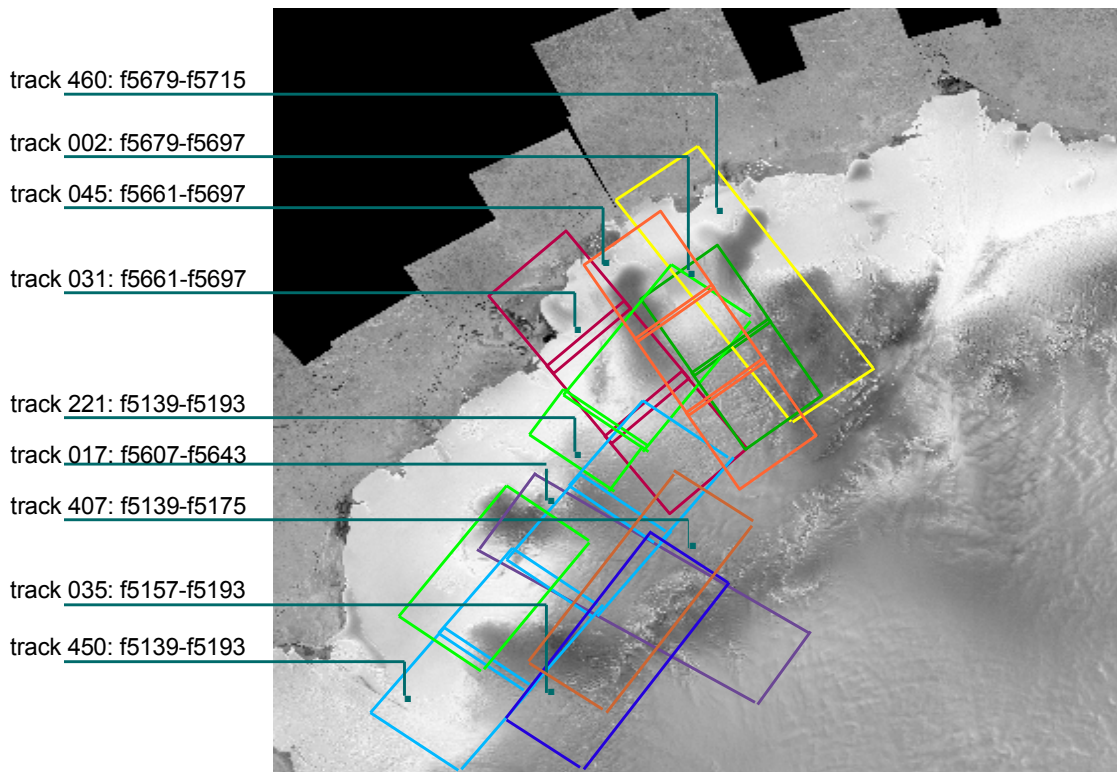

Figure 2.1: Overview of the used ERS SAR image tracks and frames. In the background is the mosaic from the Radarsat Antarctic Mapping Mission.

3 SAR Processing

Literature

J. Curlander & R. McDonough, *Synthetic Aperture Radar - Systems and Signal Processing*, p. 126-208.
M. Soumekh, *Synthetic Aperture Radar - Signal Processing with MATLAB Algorithms*, p. 1-47.
I. Cumming & F. Wong, *Digital Processing of Synthetic Aperture Radar Data.*

The SAR processing aims to focus the satellite's raw data into an image with the highest possible resolution and phase perseverance. It is usually the first step in an interferogram formation, and the result is called a single look complex image (SLC). As partly done in this study, the raw data processing can be performed by other institutions as for example the German processing and archiving facility (D-PAF). In that case, the raw data strips are subdivided into different frames, which after being processed, can be ordered by the customer. Particularly if more than one frame is of interest, it might be advantageous to process the raw data by oneself. The SAR processing is computational elaborate, and several steps require detailed background knowledge of signal processing. In this study the Modular SAR Processor (MSP) from the Gamma Remote Sensing [CW02] company is used. Using the MSP, it is possible to keep track of several processing parameters and to check for intermediate results.
The theoretical background will now be presented. Important parameters are introduced which are used later on for the accuracy evaluation. The reader who is more interested in the geophysical product might skip this chapter.

3.1 Reconstructing the Target Function

In a simple one dimensional model [Sou99] it becomes evident how the processing of the collected data raises the resolution significantly. In this model six targets are to be resolved. The radar is on a stationary point and emits a pulse $p(t)$ with velocity v. As soon as the pulse hits a target, one part gets reflected and another part propagates until it hits the next target and so on. The radar records the reflected echos. The amplitude of the reflected echo depends on the targets' reflectivity σ_n, the phase information is more or less arbitrary. This model is simplified, but it will demonstrate the basic idea

of a reconstruction.

The target function is represented by:

$$f(x) = \sum_{n=1}^{6} \sigma_n \delta(x - x_n) \tag{3.1}$$

which is a series of delta functions, representing ideal targets at position x . The goal of the processing is to recover that function from the recorded signal with the highest possible resolution. Traditionally, the radar's resolution depends on the pulse duration. It reaches its boundary as soon as the trailing edge of one echo merges with the leading edge of another. Therefore, a short pulse duration raises the radar's resolution. However, a shorter pulse carries less energy with it, and the signal to noise ratio (SNR) deteriorates. With the target function from equation 3.1 it is straight forward to write down the ideally reflected signal $s(t)$. It is just sum of the emitted pulses whereby each pulse is recorded with a certain runtime retardation:

$$s(t) = \sum_{n=1}^{6} \sigma_n p(t - \frac{2x_n}{v}) + n(t) = (f * p)(t) \tag{3.2}$$

or in a continuous case:

$$s(t) = \int_x f(x) p(t - \frac{2x}{v}) dx + n(t) = (f * p)(t). \tag{3.3}$$

where v stands for the signal's velocity and t for its runtime. In continuous as well as in the discrete case, the reflected signal is represented as the convolution of the target function f with the emitted pulse p plus some noise $n(t)$, which will be neglected in the following. As mentioned earlier, the goal is to extract the target function $f(x)$ from the recorded signal $s(t)$. By Fourier transforming $s(t) \rightarrow F_\omega(s)$ and $p(t) \rightarrow F_\omega(p)$, the convolution theorem can be applied:

$$F_\omega(s) = F_\omega(f) \cdot F_\omega(p) \tag{3.4}$$

which turns a convolution in the time domain into a simple multiplication in the frequency domain. In order to validate equation 3.4 one needs to insert the corresponding Fourier integrals and change the order of integration. If the Fourier transformations are known, thiss is a powerful tool because often multiplications are easier to handle than integrations. This is the case here as well, because the target function can be found by dividing through $F_\omega(p)$, and back-transforming the result:

$$F_\omega^{-1}\left(\frac{F_\omega(s)}{F_\omega(p)}\right) = f(x). \tag{3.5}$$

where $F_\omega^{-1}(\cdot)$ stands for the respective inverse Fourier transformation. However, equation 3.5 assumes that the Fourier transformation $F_\omega(p(t))$ does not have zeros. In other words

it means, that the emitted pulse $p(t)$ has an infinite bandwidth, which is of course not realistic. But it still shows that by means of a Fourier transformation, it is possible to transfer the problem into a problem of resolving frequencies, rather than resolving runtime delays. Consequently instead of shortening the pulse duration, it might be better to modify the frequencies in the pulse and to analyze the response with respect to these frequencies. Matched filtering is an example of such a frequency analysis.

3.2 Matched Filtering, Range Compression

The reconstruction via matched filtering is basically a cross-correlation of the emitted pulse $p(t)$ with the received signal $s(t)$. It represents a special method of pulse compression which means, that the original pulse is artificially shortened (through signal processing) to increase resolution. The cross-correlation can be performed in the time or in the frequency domain. In the MSP the range compression (e.g. compressing the image in range direction) is implemented in the frequency domain. In the time domain the correlation is performed by calculating:

$$s_c(t) = \int_{-\infty}^{\infty} s_r(\tau)h(t - \tau)d\tau \tag{3.6}$$

where s_c is the compressed signal and s_r is the recorded signal, which is affiliated with noise. The filter h is the complex conjugate and time reversed function of the outgoing signal's replica. Basically equation 3.6 expresses, that the recorded data is correlated with the emitted pulse.

In order to calculate the integral from equation 3.6, h has to be known first. Therefore a representation of the outgoing pulse is needed. In a SAR system, this pulse is often given by a linear frequency modulated signal [IC05]:

$$s(t) = \text{rect}(\frac{t}{T})e^{j\pi Kt^2} \tag{3.7}$$

It is called a linear frequency modulated pulse, because the frequency $\frac{1}{2\pi}\frac{\partial\Psi}{\partial t} = Kt$ is a linear function of time with the frequency rate K. The $\text{rect}(\cdot)$ function confines the signal to the time interval $[-\frac{T}{2}, \frac{T}{2}]$. If a pulse in the form of 3.7 is emitted, then the ideal recorded signal s_r can be expressed as:

$$s_r = \text{rect}(\frac{t - t_0}{T})e^{j\pi K(t-t_0)^2} \tag{3.8}$$

which incorporates only the time delay t_0. Then the filter h is given by:

$$h(t) = \text{rect}(\frac{t - t_0}{T})e^{-j\pi Kt^2} \tag{3.9}$$

12

and hence the integral from equation 3.6 turns into:

$$s_c(t) = \int_{-\infty}^{\infty} \text{rect}(\frac{\tau}{T}) e^{j\pi K(\tau)^2} \text{rect}(\frac{t-\tau}{T}) e^{-j\pi K(t-\tau)^2} \tag{3.10}$$

with t_0 set to 0 for simplification. The integral 3.10 is not difficult to calculate ([IC05] p.108), but it does not add to further understanding. The result is a sinc function:

$$s_c(t) = (T - |t|)\text{rect}(\frac{t}{2T})\text{sinc}(Kt(T - |t|) \approx T\text{sinc}(KT(t - t_0)) \tag{3.11}$$

which peaks at t=0 as expected since t_0 was set to zero. So through a cross-correlation with the correct filter h ideal targets can be localized. In real life no ideal targets in the form of equation 3.1 exist and the raw data s_r is a superposition of all scatterers in the scene combined with noise. In that case it can be shown that the matched filtering also optimizes the SNR ratio. The result of the compression can be seen in figure 3.1.

A look at the resolution of the compressed signal explains the strength of the matched filtering. There, the resolution is essentially defined by the width of the sinc function's main lobe, as indicated on the bottom of figure 3.1. More specifically, it is defined as the spread of the function at 0.707 (-3-dB) below its peak. With a Taylor expansion of 3.11 around t=0:

$$T\text{sinc}(KTt) \approx T(1 - \frac{1}{6}(KTt)^2 + ...) \tag{3.12}$$

the spread $\Delta\tau$ of the peak is:

$$\Delta\tau \sim \frac{1}{KT} \tag{3.13}$$

The resolution in time can be related to the resolution in space by multiplying with the speed of light. The product KT specifies the signal's bandwidth and indicates how many frequencies are contained in the pulse. In a traditional radar system, which is based on a pure runtime measurement, the resolution depends, as mentioned above, only on the pulse duration, and is thus proportional to T. The compression factor

$$C_r \sim \frac{T}{1/(K/T)} = KT^2 \tag{3.14}$$

compares the resolution before and after the matched filtering. Typical values ([IC05]) are for example $K = 4.1 \cdot 10^{12}\frac{Hz}{s}$ and $T = 42 \cdot 10^{-6}s$. This results in a compression ratio of 723. In other words, the synthesized pulse duration is 723 times shorter than the actual one, which leads to a significant increase in resolution.

Crucial for the whole process is the generation of the frequency modulated pulse (chirp) from equation 3.7. It is necessary to keep track on variations during the generation, so that a precise compression can be performed. A similar idea is used in order to compress the images in azimuth direction. The problem is that no azimuth chirp was actively send from the antenna. Instead this chirp must be generated from the history of several range chirps first, before a compression in azimuth direction is possible.

Real part of ideal signal
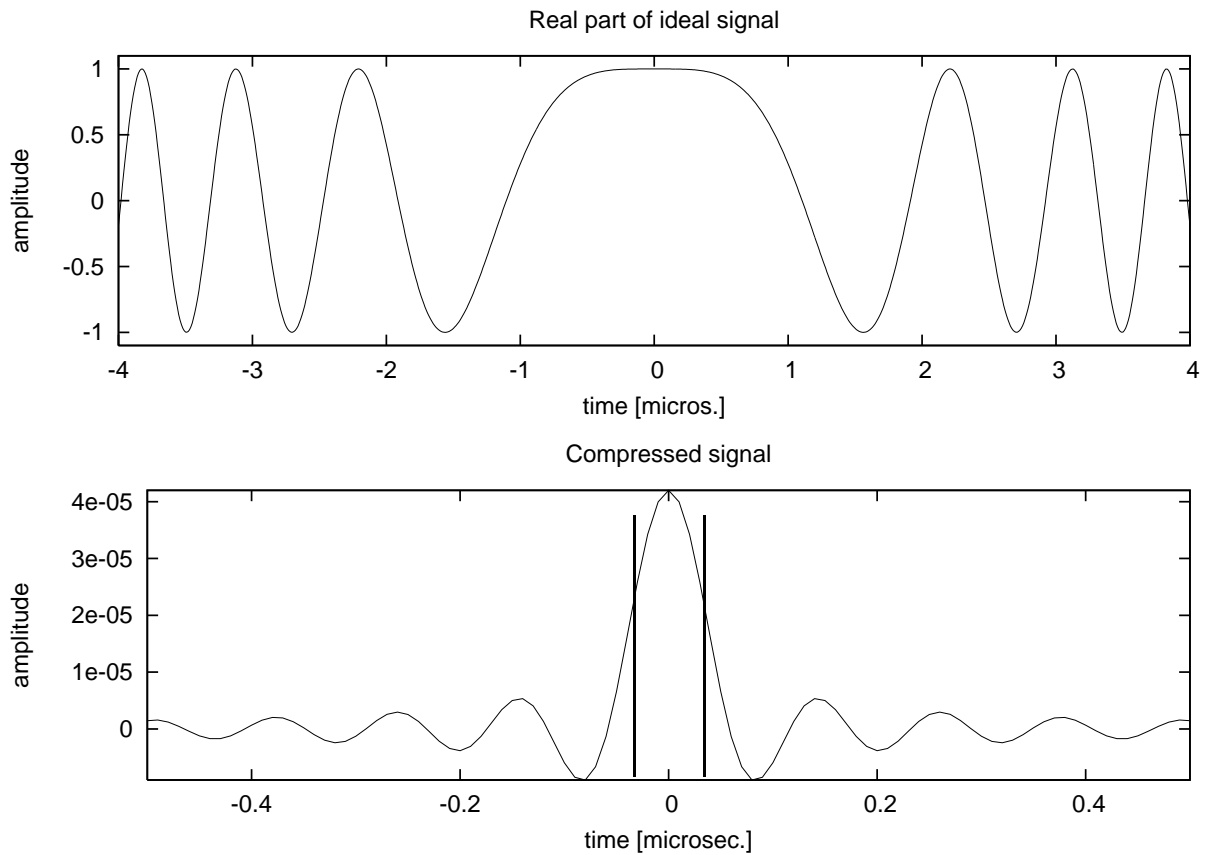
Compressed signal

Figure 3.1: top: The real part of the linear frequency modulated signal received from a point target. **bottom:** Compressed signal with two bars that indicate the resolution.

3.3 Azimuth Compression

To compress the signal not only in range but also in azimuth direction is the distinct difference between a real aperture radar (RAR) and a SAR. As mentioned before, the chirp in azimuth direction is created by looking at the history of several range chirps. Figure 3.2 illustrates the geometry for that. With usually a monostatic antenna, the satellite emits subsequent pulses to the earth's surface, and records the responses in-between emitting. The various footprints cover the same targets several times, and the frequency spectrum of that target is Doppler shifted, because of the relative velocity between platform and target. No Doppler shift is observed at the range of closest approach, because the relative velocity has no component perpendicular to the line of flight. In a squinted geometry, this point is not at the beam center. The coverage of targets by different footprints is defined by the pulse repetition frequency and the sensor's velocity. The azimuth direction is also referred to as the slow time domain, in

14
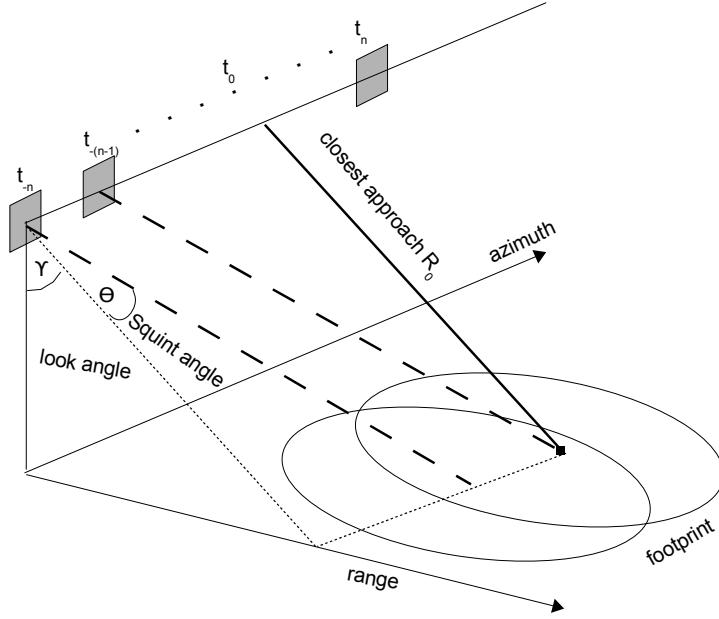
Figure 3.2: The satellite emits subsequent pulses which illuminate the target several times. Because of the relative velocity between target and satellite, the signal response is Doppler shifted. The squint angle is largely exaggerated, but plays a crucial role during the processing.

analogy to the fast time domain in range, which is defined by the speed of light. Traditionally, the resolution in azimuth is connected directly to the size of the footprint. Targets at equal range within the footprint cannot be resolved. The azimuth compression thus aims at synthesizing a small footprint. It is comparable to the range compression, where a shorter pulse is synthesized. For that a reference function as in equation 3.9 needs to be derived. This can be done by looking at the Doppler shifted phase history of one target that passes through the footprint:

$$\Psi(\tau) = \exp(\frac{i4\pi R(\tau)}{\lambda}) \tag{3.15}$$

Note that t now stands for the time in the slow time domain. The distance $R(t)$ can be calculated from figure 3.2 and the platform velocity v_p:

$$R(t) = \sqrt{(v_p t)^2 + R_0^2} \approx R_0 + \dot{R}_0(t - t_0) + \ddot{R}(t - t_0)^2 + ... \tag{3.16}$$

Differentiating $\frac{d}{dt}R^2 = 2R\frac{d}{dt}R$ and $\frac{d}{dt^2}R^2 = \frac{d}{dt}(2R\dot{R})$ values after some calculations:

$$\dot{R} = \frac{v_p^2 t}{R} \qquad \text{and} \qquad \ddot{R} = \frac{v_p^2}{R}\left(1 - \frac{v_p^2 t^2}{R^2}\right) \approx \frac{v_p^2}{R} \tag{3.17}$$

Under the assumption of a flat and non rotating earth, the range equation 3.16 predicts an approximately hyperbolic path of a point target which migrates through the satellite's footprint. In this case the phase of the signal response looks like:

$$s_r \sim \exp(\frac{i4\pi R_0^2}{\lambda})\exp(\frac{i2\pi v_p^2 t}{\lambda R_0}(t - t_0) + \frac{2v_p^2}{\lambda R_0}(t - t_0)^2/2) \qquad (3.18)$$

This is again a frequency modulated signal, as already observed during the range compression. It includes two parameters:

$$f_{DC} = \frac{-2Vt_0}{\lambda R_0} \qquad \text{and} \qquad f_R = \frac{2V^2}{\lambda R_0} \qquad (3.19)$$

the Doppler Centroid f_{DC} and the Doppler rate f_R. The Doppler Centroid is the Doppler frequency at the time when the target crosses the beam center. In a non-squint geometry this equals the line of zero Doppler. It depends on the overall relative velocity between platform and target, the distance between platform and target and the magnitude of squint. A more precise derivation, including a curved earth, all geometric parameters and a discussion of neglecting higher order terms in equation 3.16, can be found in [Hei04]. There, the Doppler Centroid frequency is expressed in satellite parameters for small squint angles:

$$f_{DC} = \frac{2}{\lambda} v_{res} \sin(\Theta) \qquad (3.20)$$

where Θ is the squint angle and v_{res} the relative velocity between satellite and target. The Doppler frequency rate $f_R = \frac{df_{DC}}{dt}$ describes the modulation of v_{res} in azimuth direction. Changes in azimuth as well as in range direction are possible.

When measuring the Doppler spectrum of a target which passes through the footprint, the measurements are taken with discrete samples. Therefore **aliasing** might occur. This generally happens in the frequency as well as in the time domain, but it is best pictured in the (fast) time domain:

Typically a radar system is tuned to a certain distance, where targets are to be expected: This is necessary, because a monostatic system, which uses the same antenna for emitting and receiving, cannot do both at the same time. The choice of the pulse repetition time (PRT) thus establishes a certain time window in which the response can be recorded. This simultaneously determines a certain distance interval $[a, b]$ where targets can be located uniquely. The maximum distance is then given by $b = R_{max} = \frac{1}{2} \cdot c \cdot PRT$, where the factor $\frac{1}{2}$ results from a two way travel time. All echos from targets outside $[a, b]$ cannot be allocated to a certain send pulse, but several possible solutions for those echos exist. For example, a strong reflector located at $r > R_{max}$ appears as an early echo from the subsequent pulse, and the response is folded back into the original interval $[a, b]$: The bright reflector far away appears suddenly as a ghost target, closer than its actual position. If that happens, the signal is aliased. The degree of aliasing is set by the PRT. There are various techniques to lessen the effect of aliasing, as for example
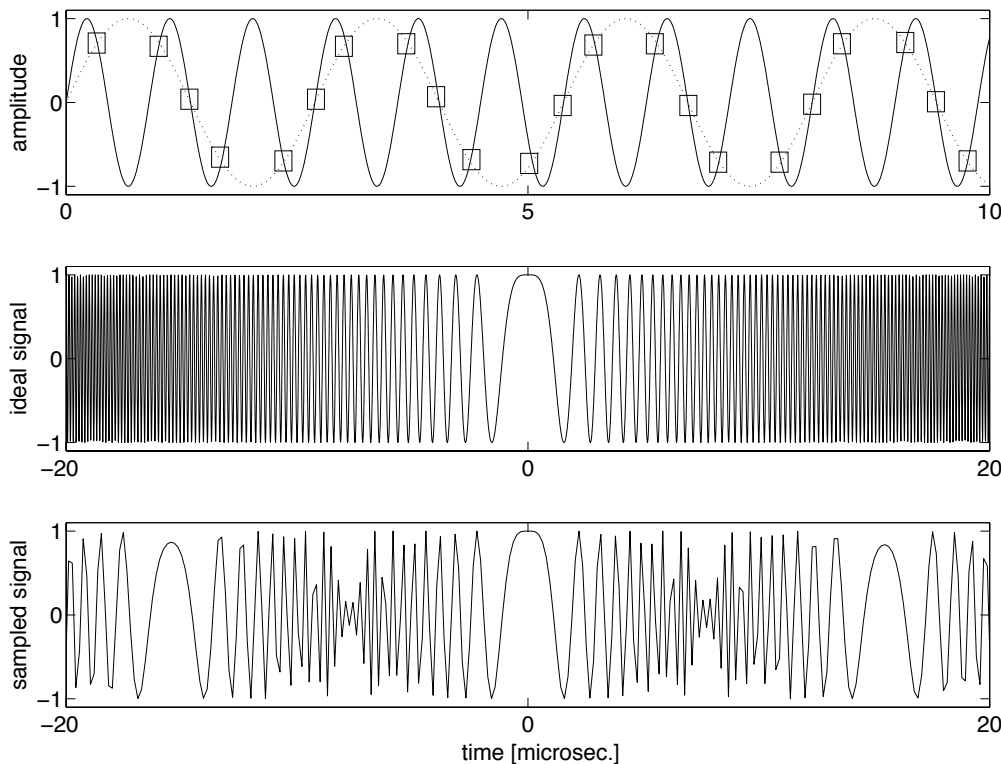
Figure 3.3: Aliasing of the azimuth signal, due to discrete sampling. Similar graphs can be found in [IC05] at page 184.

non uniform sampling rates, but this will not be discussed here.

A more general approach to this topic is given by the Nyquist theorem, which states that the highest frequency which can be accurately represented is less than one-half of the sampling rate. This is easily pictured in the frequency domain, as done in figure 3.3. There it is shown how the sampling rate affects the end result. In the case of a too low sampling frequency, the incoming signal cannot be fully resolved, but is projected on a lower base frequency instead. In order to fully resolve the incoming signal, the sampling rate needs to be increased to be at least $f_{sample} = 2 \cdot f_{max}$, where f_{max} is the highest frequency that should be resolved. This sampling frequency f_{sample} is also called the Nyquist rate.

The two lower plots of figure 3.3 show how a too low sampling rate can lead to ambiguities in the Doppler centroid. The ideal signal is the frequency modulated chirp from equation 3.18, which is generated by the Doppler shift of a target while passing through the satellites footprint. In a non squint case, the Doppler Centroid frequency is zero in the center of the footprint (at t = 0). In a squinted geometry, the Doppler

Centroid deviates from zero. With a too low sampling rate, as shown in the lowest part, the unique form of the signal becomes aliased. The signal repeats itself, and the Doppler centroid is ambiguous. In analogy to the range aliasing, one could say that the recorded Doppler frequency is trapped in an interval of $[-\frac{F_a}{2}, \frac{F_a}{2}]$, which is caused by the limited extend of the footprint. The highest resolvable frequency F_a is given by the pulse repetition frequency (by means of the Nyquist theorem). However, due to side-lobes of the antenna signal, it is possible to record a Doppler frequency outside this interval. This frequency is than folded back to the interval $[-\frac{F_a}{2}, \frac{F_a}{2}]$, and consequently leads to ambiguities. In the ERS system, range aliasing is negligible, especially because the signal is received in continuous time, but aliasing in the azimuth direction is not. This is why the absolute Doppler Centroid is often expressed in two parts: a fractional part (as multiples of the PRF) and an integer part. This means the Doppler Centroid is written as:

$$f_{DC} = \frac{f_{DC} \bmod PRF}{PRF} + \text{round}(\frac{f_{DC}}{PRF}) \cdot PRF \qquad (3.21)$$

For a more detailed treatment on Doppler Centroid aliasing refer to [IC05] in chapter 5, p. 182-188. The integer part is referred to as the ambiguity number. The ERS satellites use yaw steering to minimize the squint angle, in order to keep the ambiguity number close to zero. This is advantageous for later processing. Unfortunately, the beam steering deteriorates for the southern hemisphere ([WU97]), and larger ambiguity numbers are to be expected when data from Antarctica is considered.

It is also desirable that both scenes have a similar Doppler Centroid, for the same reasons as mentioned during the baseline decorrelation in section 4.2. Different incidence angles lead to a lower coherence. For interferometrical applications the Doppler Centroids of the two scenes are usually averaged ([Han01]).

The Doppler Centroid can be derived from a precise knowledge of the orbital geometry. However, mostly it is more accurate to derive it from the data itself. For that, various algorithms have been developed, which estimate the ambiguity number as well as the fractional part. This will be discussed below.

Another characteristic of the Doppler Centroid is its **range dependency**. The range dependency can be calculated from the recording geometry. Mostly it is caused by the curved earth surface which was neglected so far, as well as different pointing angles of the sensor (yaw, pitch). If all this is taken into account, the Doppler Centroid is expressed in a polynomial in range up to a third order. For more information on the range dependency and its derivation refer to [IC05] in chapter 5, p. 189-194.

With equation 3.18 the azimuth compression can be performed in the same way, and with the same benefits, as the range compression. Therefore, the SAR focusing can be viewed as consecutive one dimensional matched filtering, first in range and then in azimuth direction. However, if the range of a target changes over azimuth, as expressed in equation 3.16, the compression is actually a two dimensional process, because the migration is in the order of several pixel. In order to decouple the 2-D problem into two 1-D compressions, some algorithms (as for example the Range-Doppler-Algorithm)

correct the migration of targets over range before the azimuth compression. This is called the range cell migration correction (RCMC). If this is performed correctly, the computational effort is lessened, as two successive 1-D compressions are faster than the corresponding 2-D compression.

In terms of resolution, the problem shifted from resolving time intervals to the resolution of frequency intervals. By means of a Fourier transformation, the resolution of frequencies is inversely proportional to the time that is available to observe the signal. Thus $\delta f \sim \frac{1}{T}$, where T is the time needed to cross the complete footprint with a diameter d. The spatial extend of the footprint is mainly governed by the antenna length L_a in azimuth direction and can be approximated by:

$$\delta x = d = \frac{R_0 \lambda}{L_a} \tag{3.22}$$

This is the traditional boundary for a real aperture radar. From 3.22 the footprint crossing time T can be calculated:

$$T = \frac{R_0 \lambda}{L_a v} \qquad \rightarrow \qquad \delta f_{DC} \sim \frac{L_a v}{\lambda R_0} \tag{3.23}$$

For small squint angles equation 3.20 can be linearized:

$$f_{DC} = \frac{2}{\lambda} v \sin(\Theta) \approx \frac{2}{\lambda} v \Theta \tag{3.24}$$

and so the squint angle can be related with antenna length and the length of the look vector:

$$\delta \Theta \approx \frac{\lambda}{2v} \delta f_{DC} = \frac{L_a}{2 R_0} \tag{3.25}$$

Since the separation in azimuth δx is given by $\delta x = R_0 \delta \Theta$ the maximal attainable resolution is:

$$\delta x = \frac{L_a}{2} \tag{3.26}$$

In [Hei04] a more precise derivation of the resolution in azimuth can be found. However, the result is essentially the same, and also in reality SAR systems are close to that theoretical boundary. The result of equation 3.26 is at first counterintuitive, because a smaller antenna leads to a better resolution. This becomes clearer by the connection of a larger footprint with a larger Doppler history of the target. Moreover it is interesting that the resolution in azimuth is only a function of antenna length and independent of height. However, this is only the case in theory. Other parameters, as for example the pulse repetition frequency (PRF), limit the antenna properties. A discussion on optimal antenna properties can be found at [AF00].

To summarize: The azimuth compression makes use of the Doppler history of various targets at equal range. With the precise knowledge of orbital parameters (some parameters, as for example the Doppler Centroid, can also be derived from the raw data itself),

it is possible to create an azimuth reference function, similar to what was done during the range compression. The respective reference function is correlated with every single target response, which raises the resolution in azimuth significantly. The compression factor is even higher than the compression factor in range.

The idea of using the Doppler history of a target to increase the resolution is usually attributed to J. Wiley [Wil95] in 1956. Since than a lot of progress has been made, and SAR processors now take many more parameters into account. There are various books ([Hei04], [JCC91], [Sou99],[IC05]), which have been written on howto optimize the processing of SAR data. The complete background of this topic lies beyond the scope of this study. However, a few more details will be mentioned in the following paragraph that illustrates the main steps in the SAR focusing with the software used here.

3.4 SAR Processing - Overview

It will now be summarized which steps occur in the Gamma Modular SAR processor (MSP) [CW02] that was used in this study. A lot of the information that is summarized here can also be found in the documentation manual of the MSP [GAM06]. The MSP implements a version of the so-called Range-Doppler-Algorithm (RDA) to focus the SAR images. The flowchart from figure 3.4 gives an overview over the different steps, which will be briefly explained in the following.

Precise Orbit · For the processing it is necessary to get a good description of the satellite's trajectory. This is done via so-called **state vectors**. Here the precise state vectors from the Delft Institute for Earth-oriented Space Research (DEOS) in the Netherlands are used. The believed accuracy is in the order of 5 cm radial and about 15 cm in along and across track direction. The precise orbits are available free of charge for ERS-1 and ERS-2 until June 1996. After that, ERS-1's radar altimeter, which is needed for the precise orbit determination, stopped working. In this study all tracks ,except one (track 045, see also table in Appendix A), are covered with precise state vectors. For the track 045 state vectors from the Committee on Earth Observation Satellites (CEOS) are used. They are believed to be accurate in-between 2-10 meters. The Delft state vectors are derived using satellite laser ranging as well as through the analysis of altimeter crossovers. It also uses a precise gravity model, the Delft Gravity Model (DGM-E04). More information about the derivation can be found at [SR93]. The original time interval of the precise vectors is 60 seconds. The flight time to record a strip of 3 frames is about 45 seconds and usually the state vectors are subsampled to a 10 seconds interval or shorter.

Doppler Centroid estimation · Because every line in the raw data contains the contributions of all targets in that line plus a significant amount of noise, it is not trivial to get a correct estimate of the Doppler Centroid. It is required to resolve the Doppler
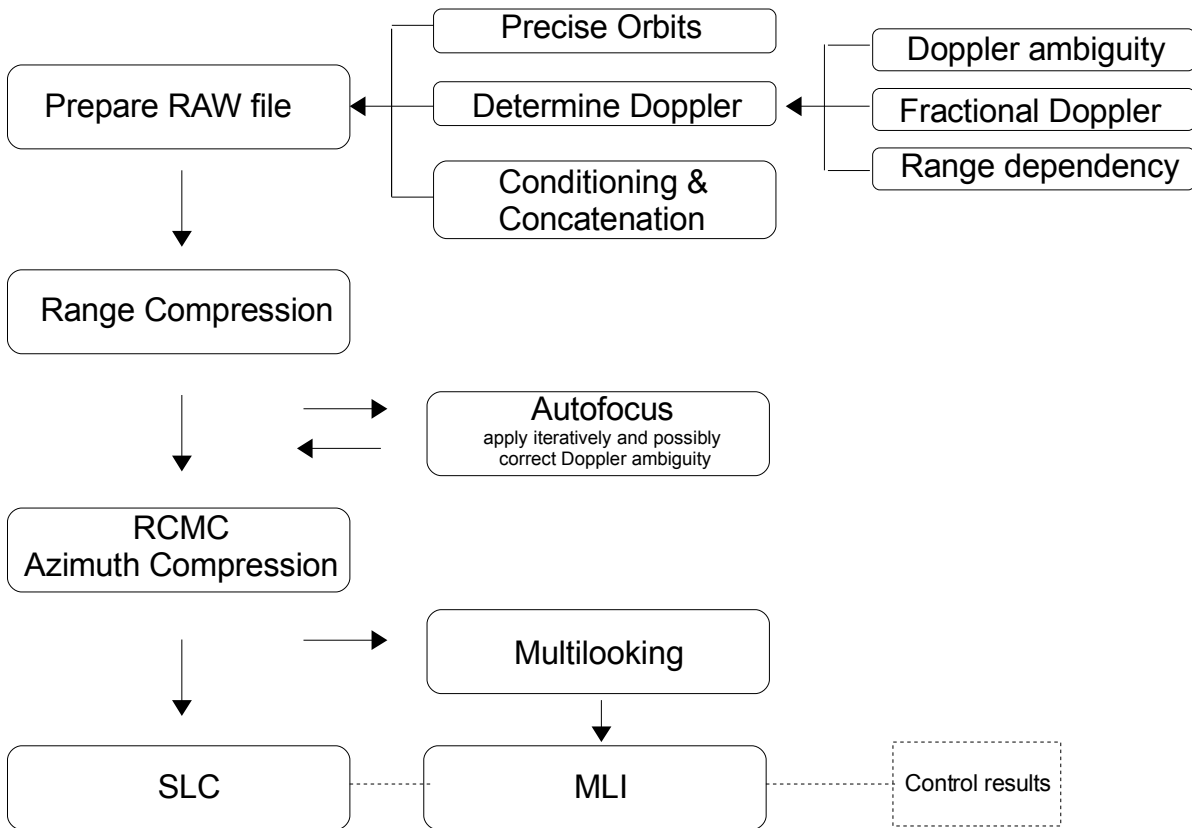
Figure 3.4: Flow chart of the raw data processing as implemented in the MSP. The output is a single look complex (SLC) or a multi-looked image (MLI). A version of the Range-Doppler-Algorithm is used. Note that with scenes of low contrast, as for example large ice sheets, it is not advisable to use the autofocus to iteratively adjust the Doppler ambiguity.

ambiguity and the fractional Doppler centroid from equation 3.21. For the estimation magnitude as well as phase based algorithms exist. It is also possible to calculate the DC from the geometry, but this is considered to be less accurate.

A magnitude based algorithm computes and averages the spectra of several range lines, and determines the DC by finding the peak of that spectra in the presence of noise (see also [IC05], chapter 12). So it is only possible to determine the fractional part of the DC. In case of a non zero ambiguity number, the absolute value of the DC is greater than $\frac{1}{2} \cdot \text{PRF}$. Therefore other algorithms, which approximately calculate an unambiguous DC, are used to find the right ambiguity number and to correct the more precise (but ambiguous) value of the magnitude based approach with multiples of the PRF. Examples for such algorithms are the multilook cross correlation (MLCC) and the multilook beat frequency (MLBF) algorithm. In a simplified view, the MLCC correlates two different range looks and calculates the change of phase between the two looks. This change is

proportional to the absolute DC. The so estimated DC is not very accurate, but mostly sufficient enough to resolve ambiguity problems from other algorithms. It also exhibits the range dependency. More information can be found for example at [ESA07], chapter 2. The MLBF algorithm is a similar phase based approach, where two looks are multiplied with each other to generate a beat signal which peaks at a point proportional to the DC (more information at [IC05], chapter 12). Usually the MLCC algorithm is more reliable in scenes with low contrast, as it is the case when larger ice sheets with no distinct features are being considered. Both algorithms will be referred to as Doppler ambiguity resolver (DAR), since the absolute DC output is usually not used.

Alternatively, it is possible to derive the DC through iterative autofocusing. There the along track velocity is estimated and, if necessary, corrected. This is done by cross correlating different range compressed looks and checking for shifts in range and azimuth. By looking at the range migration between the looks, it is possible to adjust the ambiguity number if the observed migration deviates from the expected. This method is overall reliable, but using it over featureless areas like ice sheets is asking for trouble. It hardly ever ends up with correct results.

Therefore, the magnitude based approach together with the MLCC algorithm, to resolve the expected ambiguities for the souther hemisphere, seems to be the best possibility for an accurate DC estimate. For ERS the DC at the scene center is roughly in the order of -700 Hz, which, according to equation 3.20, translates into a squint angle of about 0.14° if a relative velocity of 7500 $\frac{m}{s}$ is assumed.

Conditioning and Concatenation · If some lines in the raw file are missing, theses have to be filled in first, before the actual processing. Also all lines are aligned to the same range delay. For the user the most interesting option is the possibility to concatenate adjacent frames for simultaneous processing. Larger strips are favored for several reasons. If single frames are processed, parameters like the baseline or the Doppler centroid are estimated individually. This leads to discontinuities if, later on, individually derived DEMs are appended. It is also time-saving to process a larger strip than to individually process every single frame. Restricted is the concatenation on the one hand by available computational power. Especially the phase unwrapping of larger strips needs larger amounts of memory. On the other hand, the refinement of the baseline, which is represented linearly in slow time within the Gamma software, hits its boundary for too long strips. Here, strips with a maximal amount of 4 frames where chosen.

Range Compression · The principles of range compression are already mentioned above. Additionally, it is necessary to take sensor dependent parameters into account to correct for example changes in gain across the swath.

Autofocus · Autofocusing looks in the first line for errors in the azimuth velocity, as described as part of the DC estimation. It is possible to use it for DC estimation, but this is not done here.

RCMC and azimuth compression · The azimuth compression uses the range compressed data, and compresses in azimuth direction as mentioned above. During the work of this study it turned out, that the data is not phase corrected to zero-doppler geom-

etry, but remains centered to the satellite's footprint. This is an important difference to other SAR processors (as for example from the German Archiving and Processing Facility D-PAF), which usually compute the scene to a zero Doppler geometry. The RCMC is incorporated into the azimuth compression.

Multilooking · From an interferometrical point of view, multilooking means averaging in range and/or in azimuth direction. Since the resolution is approximately 5 times higher in azimuth direction compared to the range direction, the SLC images are not directly apparent to the observer. It is handy to average with a factor of 5 higher in azimuth direction than in range direction, in order to get square like images, which are easier to interpret and take up less space. Also the noise level in interferograms is decreased, of course at the cost of spatial resolution. All interferograms in this study are averaged with a factor of 2 in range and a factor of 10 in azimuth. Both, SLC and MLI, are complex images, which means that they store information about amplitude and phase.

Through shell scripting, the processing with the MSP can be widely automated. Despite the highly automated and ready to use functions, it is still necessary to develop a basic understanding of the process. This is necessary in order to control the results and to choose the right parameters. When processing scenes in Antarctica, special care with respect to the DC is required. Usually the DC should approximate its real value by 5 %, but if the wrong algorithm is being used, this is virtually never the case. Frames which are processed to the wrong ambiguity lead to severe errors in the derived DEM, which was discovered painfully during this study. The advantage of processing the data manually (instead of ordering the processed SLC from an archiving facility) is that several frames can be concatenated. It was also observed that some frames from processing facilities were processed to the wrong Doppler. In that case, it is impossible to correct that and the SLC is basically useless for interferometry.

The SAR focusing includes more steps than mentioned here. Especially the whole topic of motion compensation, which is more important for the airborne case, less so for the satellite borne case, has not been addressed. For more information please refer to the manual of SAR processors ([WU97]) or books ([IC05], [Hei04], [IC05]).

4 ERS SAR Interferometry over the Antarctic Ice Sheet

Interferometry in general deals with the superposition of waves and the detection of phase shifts. There is a vast amount of different applications, but in the underlying principles they are all closely related. Differences occur in the actual realization of the system and the processing of the data.

This chapter starts with an introduction to the basic principles of interferometry, which can be found in various textbooks (for example [Dem04]). It will not specifically be connected to the satellite based case, but rather aims at clarifying notation and preparing the basics for the next sections.

The realization of a satellite based approach is explained in the section of the emergence and interpretation of fringe patterns. A fringe thereby means a full transition of phase from 0 to 2π. Without going into too much detail it will be explained how fringes are formed, what restrictions exist and how the fringe pattern might be interpreted. From there on, all interferograms can be understood without further background knowledge. The two sections on image processing go into more detail. The complete processing chain:

will be clear after this. The first step focuses the raw data and creates high resolution images of phase and amplitude, which are both stored in one single look complex file (SLC). This was already explained in chapter 3. Two of these SLCs are used to form an interferogram. Dividing that interferogram with a differential approach into a DEM and a flowfield is the aim of the DInSAR processing. Critical processing parameters, as for example the Doppler centroid and baseline, will be considered in a processing example of chapter 5. Other influences, like atmospheric contributions or a varying penetration depths, will be mentioned during the geophysical evaluation of the final products in chapter 6.

4.1 Basics of Interferometry

Interferometric techniques examine the interrelation of different waves. A wave is a periodic disturbance of particles in a media. All waves are mainly characterized by their amplitude $\vec{A}$ and phase Ψ. The amplitude defines the maximum deflection of the particles. The phase characterizes the amount of deflection at time t and location $\vec{x}$ during the successive cycles. It contains the angular frequency ω and wavelength λ. A radar uses electromagnetic waves which consist of oscillating electric and magnetic fields and don't need a media to propagate. The electric field is often described with the help of a complex function:

$$\vec{E}(\vec{x}, t) = \vec{E}_0 e^{i(\Psi + \phi_0)} \tag{4.1}$$

with

$$\Psi = \vec{k}\vec{x} - wt, \qquad |\vec{k}| = \frac{2\pi}{\lambda}, \qquad \omega = |\vec{k}|c \tag{4.2}$$

The wave propagates with the phase velocity c into the direction of the wave vector $\vec{k}$. These two variables are connected with the angular frequency through the dispersion relation $\omega = |\vec{k}|c = \frac{2\pi c}{\lambda}$. Equation 4.1 is the simplest solution of the Maxwell equations. It describes the electric field in a vacuum as a plane wave. A similar equation holds for the magnetic field. The polarization is expressed in the amplitude's vector character. Basic states of polarization can be vertical or horizontal and any linear combination of these two. In both cases the amplitude points orthogonal to the direction of propagation. The arbitrary phase shift ϕ_0 characterizes the starting conditions and in the following is set to zero.

The electric field $\vec{E}$ is usually not observed. What we see is rather the beam's intensity. The intensity I is defined as the complex square $I = \vec{E}\vec{E}^* = |\vec{E}|^2$, which is a real function. When n waves $\vec{E}_k$ are superimposed, the resulting wave function $\vec{E}_{res}$ is the sum of all the single wave functions represented by equation 4.1:

$$\vec{E}_{res} = \sum_{k=1}^{n} \vec{E}_k \tag{4.3}$$

This is a consequence of the linearity of Maxwell's equations. In respect of the intensity

this means:

$$
\begin{aligned}
I_{res} &= \sum_{k=1}^{n} \vec{E}_{res,k} \sum_{k'=1}^{n} \vec{E}_{res,k'}^{*} = \sum_{k,k'=1}^{n} \vec{E}_{0,k} \vec{E}_{0,k'}^{*} e^{i(\Psi_k - \Psi_{k'})} \\
&= \sum_{k=1}^{n} |\vec{E}_k|^2 + \sum_{k \neq k'} \vec{E}_{0,k} \vec{E}_{0,k'} e^{i(\Psi_k - \Psi_{k'})} \\
&= \sum_{k=1}^{n} I_k + 2 * \sum_{k < k'} \vec{E}_{0,k} \vec{E}_{0,k'} \cos(\Psi_k - \Psi_{k'})
\end{aligned}
\tag{4.4}
$$

It becomes evident that the resulting intensity is a function of phase differences

$$
\Delta \Psi_{k,k'} = \Psi_k - \Psi_{k'} \tag{4.5}
$$

that appear in the so called interference term. This phase shift $\Delta\Psi_{k,k'}$ determines whether the superimposed wave is an attenuated or amplified version of the incoming waves. It can be an arbitrarily large number and is from now on referred to as $\Delta\Psi_{unw} = n \cdot 2\pi$ (omitting indices k and k'). Since $\vec{E}(\vec{r},t)$ is a 2π periodic function only the 'wrapped' phase shift $\Delta\Psi_w$ with

$$
\Delta\Psi_w = \Delta\Psi_{unw} \mathrm{mod} 2\pi \tag{4.6}
$$

is crucial in terms of amplification or attenuation. In fact, in most applications only Ψ_w is known to begin with. This problem is referred to as the phase ambiguity, and becomes of interest later on in phase unwrapping procedures which try to resolve this ambiguity. Since it is usually clear from the context whether $\Delta\Psi$ depicts the wrapped or the unwrapped phase the indices Ψ_w and Ψ_{unw} are not always indicated.

Two extreme cases of interferences are complete extinction and maximum amplification. The first case with $n = \frac{1}{2}, \frac{3}{2}, ...$ is called *destructive interference*, the latter with $n = 1, 2, ...$ is called *constructive interference*.

For interference experiments it is necessary to have a *coherent* light source, with a defined wavelength λ, where the signal's phase and amplitude are known at all times. A coherent radar is such a system , whereas a normal light bulb is not, since the light consists out of a mixture of different wavelengths at random phases. In the latter all the the interference terms in equation 4.4 cancel each other during the summation because phase shifts are randomly distributed in $[0, 2\pi]$. This is why coherent systems like lasers or SARs are of such high interest.

Interference experiments are based on the idea of detecting $\Delta\Psi_w$ and to extract $\Delta\Psi_{unw}$ through signal processing. The phase shift can be induced through, for example, slight surface changes or different viewpoints of the observer. The sensitivity of the procedure is influenced by the wavelength λ and the capability of relating the induced phase shift to the geometry of the system.
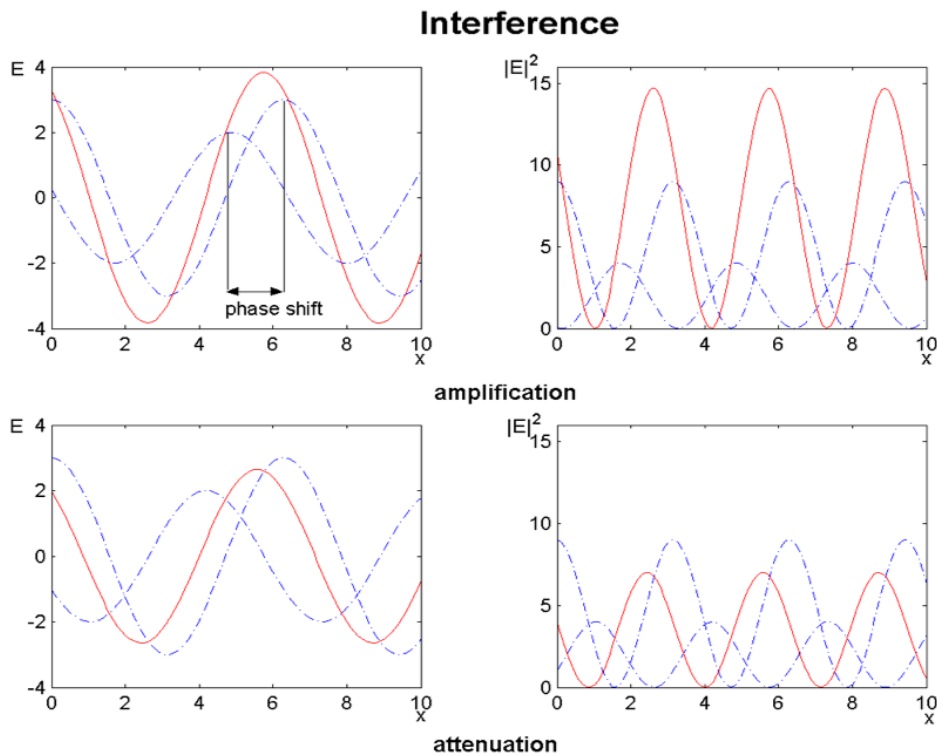
Figure 4.1: The red wave is the superposition of the two blue waves. The phase shift determines whether the resulting wave is a amplified or attenuated version of the two incoming waves.

4.2 Emergence and Interpretation of Fringe Patterns

Let's take a closer look at the radar which is used in this study. Both ERS satellites carry a coherent and side looking synthetic aperture radar (SAR), which records images at a ground sresolution of ca. 5 m along track (azimuth) and 20 m across track (range). The satellite geometry during the acquisition is sketched in figure 4.2. In terms of notation one distinguishes between slant range (along look vector) and ground range (projected onto the ground). From now on the term range always refers to slant range unless noted otherwise. A more detailed passage on how these images are recorded and focused can be found in the SAR processing section 3. For now, it is only important that each grid cell of the image contains information about the reflection's phase and amplitude.

 From the image's **intensity** ('power') some information can easily be extracted: Figure 4.3 is an example for a power image in a mountainous area, with several outflow glaciers and a traverse route. The variation of brightness within the frame is a direct consequence
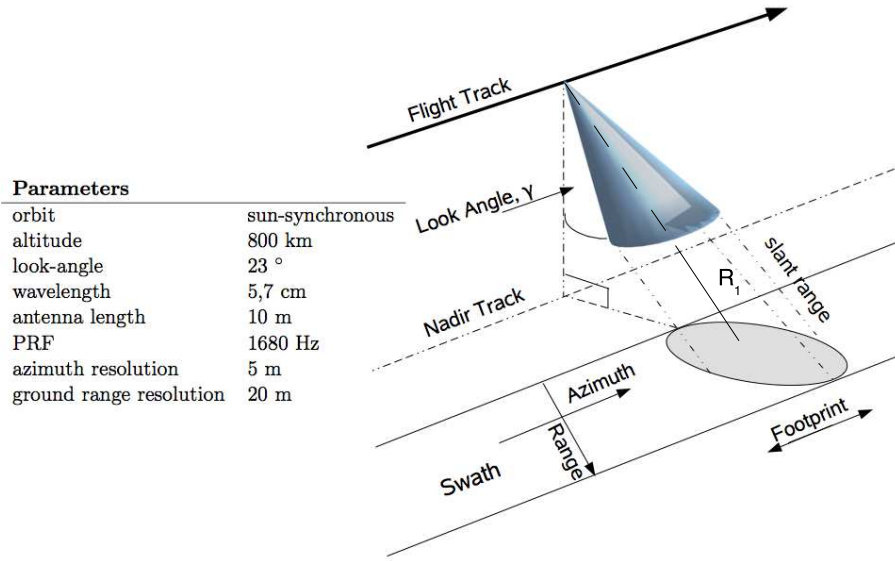
Parameters

orbit	sun-synchronous
altitude	800 km
look-angle	23 °
wavelength	5,7 cm
antenna length	10 m
PRF	1680 Hz
azimuth resolution	5 m
ground range resolution	20 m

Figure 4.2: Setup and mission parameters of the ERS 1/2 system

of the variations of reflectivity from the surface. Thereby the image intensity depends in a complex way from surface and volume scattering processes. For dry polar snow, the penetration depth in C-Band is up to 25 m [RG84].

The signal's **phase** can be split up into two parts:

$$\Psi_1 = \frac{2\pi 2 R_1}{\lambda} + \Psi_{scat.} \tag{4.7}$$

where R_1 is the look vector illustrated in figure 4.4 and λ the wavelength. The first term can be understood by looking at figure 4.2 and substituting $x = 2R_1$ in equation 4.2 (for a constant t). A factor 2 results from the two way travel distance. The second term is described in [Moh97] as:

$$\Psi_{scat.} = \Psi_{target} + \Psi_{sys.} + \Psi_{noise}. \tag{4.8}$$

Thereby Ψ_{target} represents the signal's random phase change that occurs within the grid cell during the reflection process. It can be imagined as the sum of contributions from all targets that lie within the grid cell. System delays, phase drifts, effects of processing algorithms etc. are summarized in $\Psi_{sys.}$. All thermal noise is described with Ψ_{noise}. This means that the phase of a single image is entirely random, and in itself carries no geophysical information. Only through differencing the phase of two images the random noise $\Psi_{scat.}$ can be removed.

An interferogram is formed through the combination of two acquisitions from the same scene, as pictured in figure 4.4. Therefore the wave functions y_1 and y_2 of the
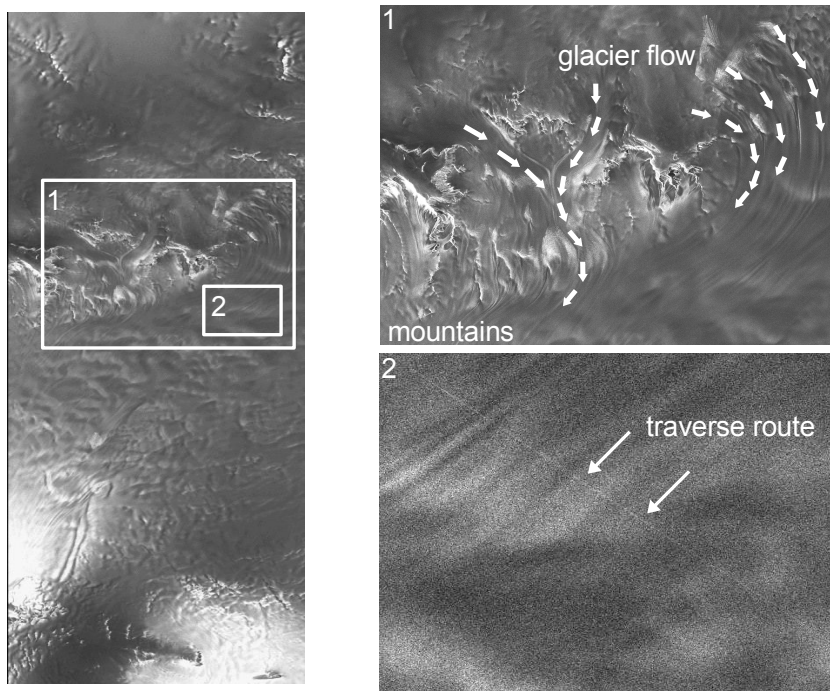
Figure 4.3: 'Power' image of the reflected amplitude. Mountains with several outflow glaciers are visible. It is also possible to track traverse routes. The dimensions of the left image are approximately (300 x 100) km.

respective grid cells are multiplied (complex) with each other, which corresponds to mere differencing of the phases:

$$y = y_1 \cdot y_2^* = |y_{1,0}||y_{2,0}|e^{i(\Psi_1 - \Psi_2)} \tag{4.9}$$

The differenced phase $\Delta\Psi$ is

$$\Delta\Psi = \frac{4\pi(R_1 - R_2)}{\lambda} + \Psi_{scat.,1} - \Psi_{scat.,2} \tag{4.10}$$

and if

$$\Psi_{scat.,1} = \Psi_{scat.,2} \tag{4.11}$$

the phase change can be associated with the optical retardation ΔR. The degree of coherence γ can be expressed by:

$$\gamma = \frac{\langle g_1 g_2^* \rangle}{\sqrt{\langle |g_1|^2 \rangle \langle |g_2|^2 \rangle}} \qquad 0 < \gamma < 1 \tag{4.12}$$

where g_1 and g_2 is the echo received at the respective antenna. The expectation values $\langle \cdot \rangle$ can be calculated using a Gaussian distribution for the received amplitude and phase.
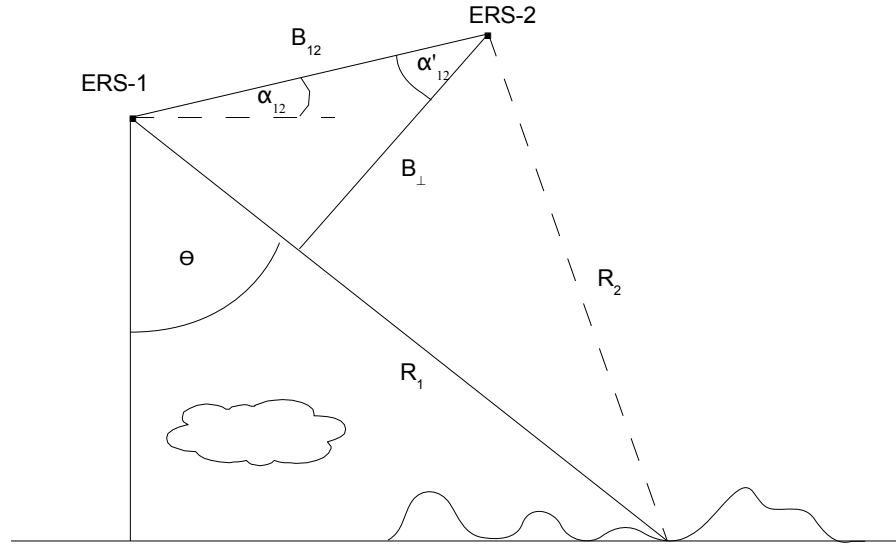
Figure 4.4: Acquiring the same scene from slightly different viewpoints. The spatial separation is described by the baseline $\vec{B}$.

If the two echos are completely independent (e.g $\Psi_{1,scat.} \neq \Psi_{2,scat.}$) the correlation $\langle g_1 g_2 \rangle$ yields zero. For a maximal interrelation of the two signals γ equals 1. There are two main factors that influence the magnitude of γ:

If the scenes are not acquired simultaneously, **stable surface conditions** are necessary to fulfill the constraint from equation 4.11 . If surface features change in-between the acquisitions, for example through melting or snow fall, the scattering characteristics Ψ_1 and Ψ_2 do not match, because scatteres become randomly rearranged. In this case the interferogram decorrelates. This is the strongest limitation for spaceborne repeat pass radar interferometry.

The **baseline decorrelation**, or Speckle decorrelation, puts an upper boundary on the spatial separation of the two viewpoints. The Speckle pattern is a grainy substructure of the images, that is caused by the random surface and volume scattering process. Different viewpoints are accompanied with slightly different incidence angles $\Delta\gamma$. Therefore, scatterers away from the center of the resolution cell contribute differently to the overall phase. Consequently, even if the scattering characteristic remains similar, the interferogram might decorrelate if the incidence angles deviate too much from each other. This effect puts a boundary, first on $\Delta\gamma$,
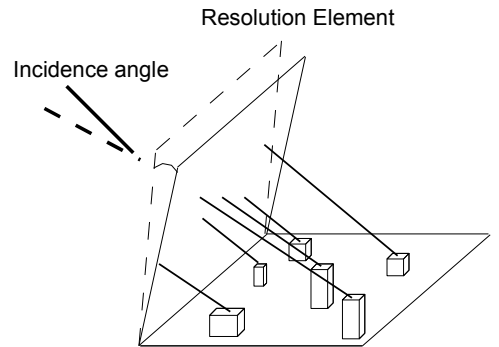

Figure 4.5: Point targets in grid cell [RR00].

and thus also on the perpendicular component of the baseline $\vec{B}$. It can be estimated [RR00] that $B_\perp$ should be less than 1km for ERS.

If the conditions of coherence are met, the phase differences have to be related to the recording geometry illustrated in figure 4.4, and expressed in known image parameters as baseline and look angle. A fully three dimensional treatment can be found in [RR00], but for simplification it is assumed here that the baseline $\vec{B}$ is in the same plane as the two look vectors. In that case is:

$$\alpha_{1,2} + (90° - \Theta) + 90° + \alpha'_{1,2} = 180° \rightarrow \alpha'_{1,2} = \Theta - \alpha_{1,2} \tag{4.13}$$

and thus the phase difference that is caused by different viewpoints is:

$$\Delta\Psi_{vp.} = \frac{4\pi}{\lambda} B_{1,2} \sin(\Theta - \alpha_{1,2}) \tag{4.14}$$

In case of a multi-pass approach, a displacement of the targets with velocity $\vec{v}$ in-between the two acquisitions induces an additional phase shift

$$\Delta\Psi_d = \frac{4\pi}{\lambda} \vec{v} \cdot \vec{R} \Delta T = \frac{4\pi}{\lambda} \Delta\rho \tag{4.15}$$

This phase shift is independent off the spatial baseline $\vec{B}$ but depends on the 'temporal baseline' ΔT. Only the displacement's projection $\vec{v} \cdot \vec{R}$ onto the line of sight is perceivable in an interferogram. Altogether, the differenced phase can be expressed as the sum:

$$\Delta\Psi = \frac{4\pi}{\lambda} B_{1,2} \sin(\Theta - \alpha_{1,2}) + \frac{4\pi}{\lambda} \Delta\rho \tag{4.16}$$

With a precise knowledge of the satellite geometry it is possible to subtract an expected phase trend for a surface with constant elevation. This phase trend is dominant in every interferogram and cross-fades other fringes caused by topography and motion. Removing these fringes, the so called 'flattening', allows to connect the resulting fringes purely to topography and displacement. After some geometric calculations [RR00], this flattened phase can be written as:

$$\boxed{\Delta\Psi = \frac{4\pi}{\lambda} \left(B_{\perp,0} \frac{z}{\rho_0 \sin(\Theta_0)} + \Delta\rho \right) = \Psi_{topo.} + \Psi_{disp.}} \tag{4.17}$$

where Θ_0 describes the incidence angle of the look vector, which points from the satellite to a constant reference surface. The distance is given by ρ_0 and $B_\perp = B \cos(\Theta_0 - \alpha_{1,2})$ is the respective perpendicular component of the baseline Bs. The target's topographic height above the reference surface is z. Equation 4.17 illustrates, that the extracted phase difference in an interferogramm is always a mixture of topography and displacement. The sensitivity to topography depends mainly on the magnitude of $B_\perp$, whereas the sensitivity towards displacement essentially only depends on the wavelength λ. From
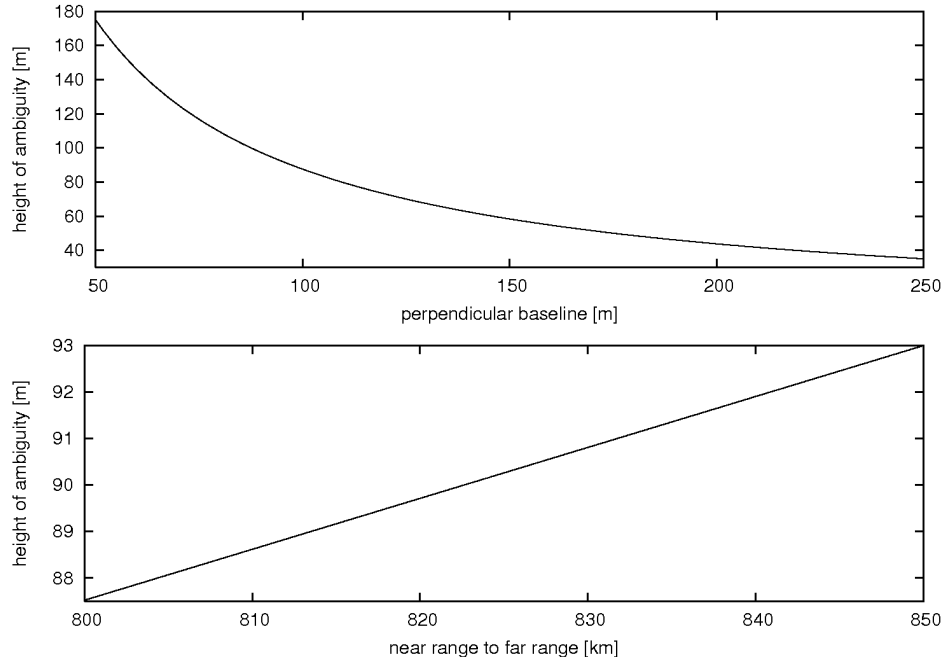
Figure 4.6: top: Baseline dependency from the height of ambiguity with $\lambda = 5.6\text{cm}$ and $\Theta = 23°$ **bottom:** Slant range dependency from the height of ambiguity with $B_\perp = 100$ km

the flattened phase in equation 4.17 one can see that for a 2π phase shift caused by topography:

$$\Delta\Psi_{topography.} + 2\pi = \frac{4\pi B_\perp}{\lambda\rho\sin(\Theta)}(z + \frac{2\pi}{\frac{4\pi B_\perp}{\lambda\rho\sin(\Theta)}}) \tag{4.18}$$

a change in height of:

$$\boxed{h_{2\pi} = \frac{\lambda\rho\sin(\Theta)}{2B_\perp}} \tag{4.19}$$

is necessary. The variable $h_{2\pi}$ is called the height of ambiguity.

For the ERS-system the wavelength λ is 5.6 cm and the height above ground $\rho \approx 800$ km with a look angle γ of about 23°. Typical perpendicular baselines range from 50 - 250 m. For example, if $|B_\perp| = 100$ m, then the height of ambiguity is 87 m. In terms of motion, only a displacement by $\rho \approx 2.5$ cm leads to the same change in phase. This shows the very high sensitivity of motion mapping. In order to raise the sensitivity to topography, large baselines are preferable, as seen in figure 4.6 (top). However, the magnitude of the baseline is restricted by the baseline decorrelation mentioned above. There is also a small change in sensitivity from near to far range (figure 4.6 (bottom)), but this effect is comparably small.

Altogether, it is now possible to understand the different contributions of orbital fringes,
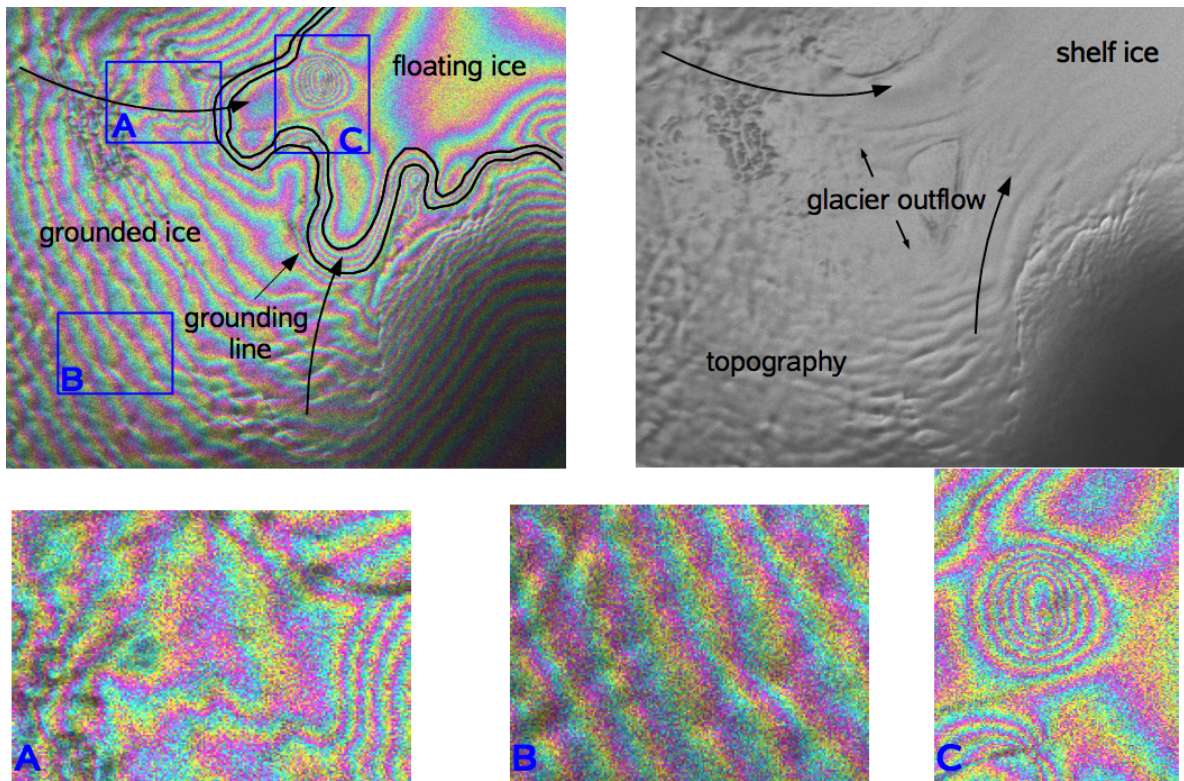
Figure 4.7: The image in the upper left corner shows a 1-day interferogram with good coherence, taken on April 15/16 1996. It covers the Ekstrøm area. On the upper right corner is the corresponding power image of the signal's amplitude. **A:** Fringes caused by a mixture of displacement from glacier flow and topography. The lines appear distorted. **B:** Smooth topographical fringes that can be connected to real topography. **C:** Fringes caused by tidal displacement with almost no topographical contribution. It is possible to mark the grounding line.

topographical fringes and motion fringes, which all influence the phase pattern of an interferogram. As a typical example serves figure 4.7, which displays an interferogram that was combined of acquisitions with a one day time difference.

In graphical representations, $\Delta\Psi$ is color coded and so a fringe is the a full transition of one color cycle. The interferogram is already flattened, so that $\Delta\Psi$ ideally only consists of a topographical part and a motion part. The phase is still wrapped in $[0, 2\pi]$, but simply from the spatial distribution of fringes it is already possible to pick geophysical information. In the lower part of the interferogram in figure 4.7 the fringes look like smooth topographical fringes, and indeed they mostly are (4.7 B). In the higher parts of the image, these fringes become increasingly distorted until they reach a region with a very high fringe density (4.7 A and C). The distortion is due to a higher contribution of motion induced fringes. This marks the area of an outflowing glacier. A high density of

motion induced fringes depicts the grounding line. The grounding line is defined as the boarder between ice which rests on solid ground and ice that floats on the ocean surface. The vertical displacement is caused by tides: The sea level is not constant in-between the two acquisitions, and the complete shelf ice is displaced with a certain contribution along the look vector's line of sight.

To summarize, each interferogram is formed out of two acquisitions, phase differences are displayed color coded and can be connected to topography or motion. Although geophysical information is visible in each interferogran, a differential approach is necessary in order to quantify the information. The complete processing chain will be explained after the presentation of the most important data sets.

4.3 InSAR

For the interferogram formation the Gamma Interferometric SAR Processor (ISP) is used. The theory of interferograms has been addressed in section 4.2. Now the basic steps of the processing are briefly explained. The flow chart 4.8 summarizes the interferogram generation.

Coregistration · Although the two acquisitions picture the same scene, the offset in range or azimuth direction can be in the order of hundreds of pixels. This is mainly due to different start and stop times. In order to prepare the images for interferometric applications, a sub pixel accuracy of the matching is needed. For performance reasons, the matching is subdivided into a coarse and a fine registration. The coarse registration determines the relative offset between the images in pixels. This data can be derived from the orbital parameters, or by visually comparing the two power images.Distinctive features can be picked in both images to calculate the offset in radar geometry. For the fine registration, which aims at matching the images with a sub-pixel accuracy, it is necessary to estimate offset polynomials in range and azimuth. For that, the image is covered with evenly distributed windows, where a cross-correlation for each window is performed. A *coherent* cross-correlation basically correlates the fringe visibility, whereas a *non-coherent* approach correlates the two power images. The latter is usually more robust, although sometimes the images do not exhibit clear features for the correlation. However, the fringe visibility is unstable with larger baselines and/or poor coherence. The result of the cross correlation algorithm is a shift in range and azimuth for all windows. This is used to fit a two-dimensional offset polynomial. After the determination of the offset polynomial, the slave image is resampled to the master's geometry. The registration of the power images can be increased if applied iteratively.

The matching with sub-pixel accuracy is critical, as poor matching leads to a decrease in coherence. However, in this study it was usually stable and will not be considered further.
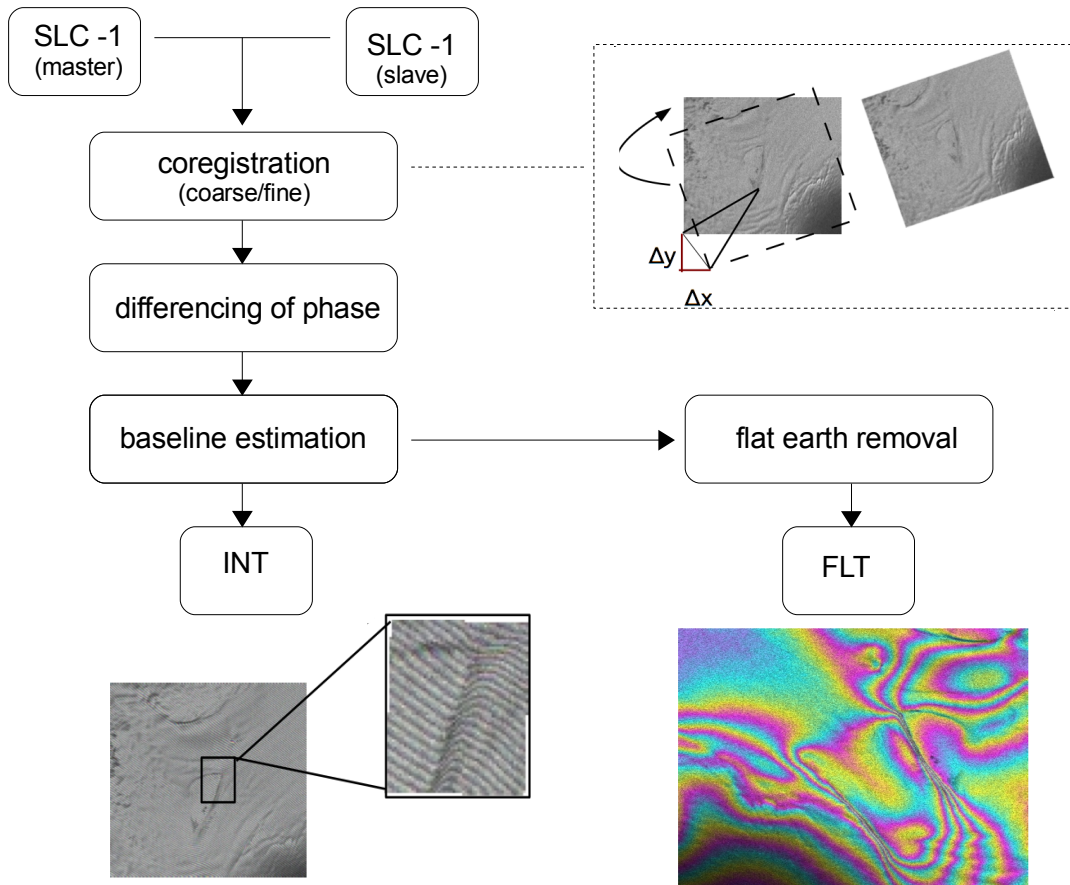
Figure 4.8: Flow chart for interferogram generation. For the DInSAR processing, the INT is preferred in order not to carry over leftover fringes. These are caused by a imprecise baseline.

Interferogram generation · As explained before, the inteferogram is generated by a point-wise complex multiplication which corresponds to a differencing in phase:

$$y = y_1 \cdot y_2^* = |y_{1,0}||y_{2,0}|e^{i(\Psi_1 - \Psi_2)}$$

In addition to that the interferogram is normalized. As mentioned in section 4.2, the phase difference contains all information about topography and displacment. Before the combination, filtering in range and azimuth can be applied to increase the SNR. Filtering in range accounts for the effect that different incidence angles lead to a spectral shift in the target response. The filtering makes sure that non overlapping parts of the spectra are removed. These appear as noise otherwise. Similar filtering is also needed in azimuth direction. There, converging orbits or different squint angles also induce a shift in spectra which needs to be accounted for. Altogether, the filtering in range and azimuth is referred to as common band filtering. For more information refer to [Han01]

chapter 2. This interferogram, which includes orbital, topographical as well as displacement fringes in $\Delta\Psi$, will be called INT. The orbital fringes are completely dominant and lead to a dense fringe pattern, which is evenly distributed over the inteferogram. For a geophysical interpretation it needs to be flattened, which premises a knowledge of the perpendicular baseline as a function of azimuth position (see section 4.2).

Baseline estimation · The baseline estimation can either rely on the orbital information or it can directily be estimated from the interferogram. The latter estimates the parallel baseline for example from the range-offset vectors, and the perpendicular baseline from the fringe frequency. If the area is flat, and orbital fringes are predominant, the perpendicular baseline can be directly estimated, and if a DEM is available it can also be done in mountainous area (see: [SK97]). For the derivation from orbital parameters the range distance of several targets is derived from the geometry for both images. Thereby, the DC which is connected to the antenna pointing angle by equation 3.20, must be taken into account. Differencing leads to a baseline which is usually represented linearly as a function of azimuth time. For more information refer to [Han01], chapter 2.

With knowledge of the baseline, the orbital fringes can be simulated and then subtracted from the image. The so flattened image is now open for geophysical interpretation. It will be referred to as the FLT. With little knowledge about the terrain, it is possible to mark areas with larger displacement (glaciers) or pure topography. However, both signals are still mixed together, and need to be separated by means of DInSAR. Without tie points or a detailed DEM it is hard to check the FLT for accuracy. Only coarse errors can be detected visually. For example, if flat regions of shelf ice, where basically no fringes are to be expected, exhibit a strong fringe pattern in form of a ramp, this points to errors in the processing. Likely is a wrong Doppler, or an imprecise estimate of the baseline (which, depending on the algorithm, could be based on the wrong DC as well). Since no DEM or other tie-points can be used for the baseline estimation, the estimate is considered to be imprecise. Therefore, INTs will be used for the DInSAR processing.

4.4 DInSAR

4.4.1 Double Differenced Interferograms

Differential Interferometric SAR processing aims at separating contributions of displacement and topography. This can be done in various ways, depending on the availability of precise DEMs or other interferograms from the same scene.

The easiest way is certainly to use an accurate external DEM and to combine it with the existing interferogram. In this so-called *two-pass* method, a second topographical

interferogram is simulated, using the geometry and baseline of the first one. A subtraction of the two interferogams results in a third interferogram containing only the displacement. A DEM can also be derived from an interferogram with no motion. This can be achieved, for example by choosing the first pair with a very short temporal and preferably large spatial baseline. This is referred to as *three-pass* or *four-pass* method, depending on whether a common master is being used or not.

However, life is not a bowl of cherries, and all of these ideas don't work in our case. This has two main reasons: On the one hand, no external DEM is available that suffices the accuracy requirements. At the time of this study three DEMs in the area of interest where available, some of them deviating hundreds of meters in coastal areas (see section 6.1). On the other hand, the displacement in the handled scenes is never small and far from being negligible. The ice-sheet is constantly moving, in some areas 0.5 - 1 meter a day. A look at the sensitivity consideration around equation 4.19 explains why this is a quite significant amount. Since only data with at least one day repeat pass is available, one can also exclude the idea of finding pairs with small temporal baselines.However, the problem is relaxed by the (often reasonable) assumption of a constant horizontal ice flow. Through so-called double differencing it is possible to cancel the displacement in both pairs. A good introduction to that procedure is given in [KR96], and the next paragraph mostly refers to that article.

Starting from equation 4.16, the phase of an interferogram from the SLCs i and j is given by:

$$\Delta\Psi_{i,j} = \frac{4\pi}{\lambda} B_{i,j} \sin(\Theta - \alpha_{i,j}) + \frac{4\pi}{\lambda}\Delta\rho_{i,j} \tag{4.20}$$

Note that Θ now stands for the look and not the squint angle. A typical situation, when dealing with scenes from ERS-1's ice phase is that three scenes are available. Thus two interferograms can be calculated with a common master. In that case the indices are (1,2) and (2,3) respectively. This is not a restriction and also two independent masters can be used (with indices being (1,2) and (3,4)). In both cases the assumption of a constant displacement means that:

$$|\rho_{1,2}| = |\rho_{2,3}| \tag{4.21}$$

To take the absolute value is only important in a three pass approach, because there one pair has a master which is acquired later than the slave. It appears as if the glaciers flow uphill, but this is only a matter of keeping track off signs. With that condition a subtraction of the two interferograms cancels the motion part:

$$\Delta\Psi_{1,2} - \Delta\Psi_{2,3} = \frac{4\pi}{\lambda} \left(B_{1,2}\sin(\Theta - \alpha_{1,2}) - B_{2,3}\sin(\Theta - \alpha_{2,3}) \right) \tag{4.22}$$

This is already a topographical interferogram, with a baseline that can be simplified further by decomposing $B_{i,j}$ into a horizontal ($B_{i,j}^z$) and vertical ($B_{i,j}^y$) part. As seen in figure 4.4, this leads to the following relation:

$$B_{i,j}\sin(\Theta - \alpha_{i,j}) = B_{i,j}^y \sin(\Theta) - B_{i,j}^z \cos(\Theta) \tag{4.23}$$

and so the double differenced phase can be expressed as:

$$
\begin{aligned}
\Delta\Psi_{1,2} - \Delta\Psi_{2,3} &= \frac{4\pi}{\lambda} \left((B_{1,2}^y - B_{2,3}^y)\sin(\Theta) - (B_{1,2}^z - B_{2,3}^z)\cos(\Theta) \right) \\
&= \frac{4\pi}{\lambda} \left(B_{1,3}\sin(\Theta - \alpha_{1,3}) \right)
\end{aligned}
\tag{4.24}
$$

which means that the baseline of the double differenced interferogram is given by the baseline between the two slaves 2 and 3, the so- called differential baseline.

Now, since no displacement is left, it is possible to use ground control points to refine the differential baseline and to turn the double differenced interferogram into a DEM. Before that can be done, the phase needs to be unwrapped to get the absolute value of the phase, which is still wrapped in $[0, 2\pi]$ at the moment (see equation 4.6). These steps will be mentioned in the following processing section.

The uncertainties of the original baseline estimates propagate into the new differential baseline. This is simply expressed through error propagation which includes differentiating equation 4.22 with respect to $B_{i,j}$. The uncertainty $s_{B_{1,3}}$ of the differential baseline $B_{1,3}$ is expressed through:

$$
s_{B_{1,3}} = 2\sqrt{\frac{\pi}{\lambda}\left(\left(s_{B_{1,2}}\sin(\Theta - \alpha_{1,2}) \right)^2 + \left(s_{B_{2,3}}\sin(\Theta - \alpha_{2,3}) \right)^2 \right)}
\tag{4.25}
$$

If additionally the condition of constant displacement in equation 4.21 is violated, in the form $|\rho_{1,2}| - |\rho_{2,3}| = s_\rho$, this leads to a leftover term after differencing:

$$
\Delta\Psi_{1,2} - \Delta\Psi_{2,3} = \frac{4\pi}{\lambda}\left(B_{1,2}\sin(\Theta - \alpha_{1,2}) - B_{2,3}\sin(\Theta - \alpha_{2,3}) \right) + s_\rho
\tag{4.26}
$$

This means that the uncertainty $s_{\Psi_{1,3}}$ of the double differenced phase is then given by:

$$
s_{\Psi_{1,3}} = 2\sqrt{\frac{\pi}{\lambda}\left(\left(\sin(\Theta - \alpha_{1,3})s_{B_{1,3}} \right)^2 \right)} + s_\rho
\tag{4.27}
$$

Looking at the phase - height relationship in equation 4.17 it can be seen how the phase error propagates into a height error s_h:

$$
s_h = \frac{\lambda}{4\pi}\frac{\rho_0 \sin(\Theta)}{B_\perp} s_{\Psi_{(1,3)}}
\tag{4.28}
$$

Through the baseline refinement, the differential baseline is adjusted with GCPs. Assuming that this works well, the error of a non-constant displacement remains. Let's assume a vertical difference s_ρ of about 7 cm a day. This induces a a phase error of approximately 2π. With a differential perpendicular baseline around 100 m this leads to a height error of 90 m. The extreme sensitivity towards displacement turns out to be a problem here, and it is worthwhile to keep an eye on that during the processing. On

the Storstrømen glacier in north-eastern Greenland a flow magnitude variability between the summer and the winter season was observed in [MJ98]. Therefore, if possible, inteferograms from the same season should be used for the double differencing in order not to violate equation 4.21. Equally important is an exact fit of the differential baseline. For now, the theoretical background of the here used DInSAR approach is set. An overview of the actual processing will conclude this section.

4.4.2 DInSAR Processing
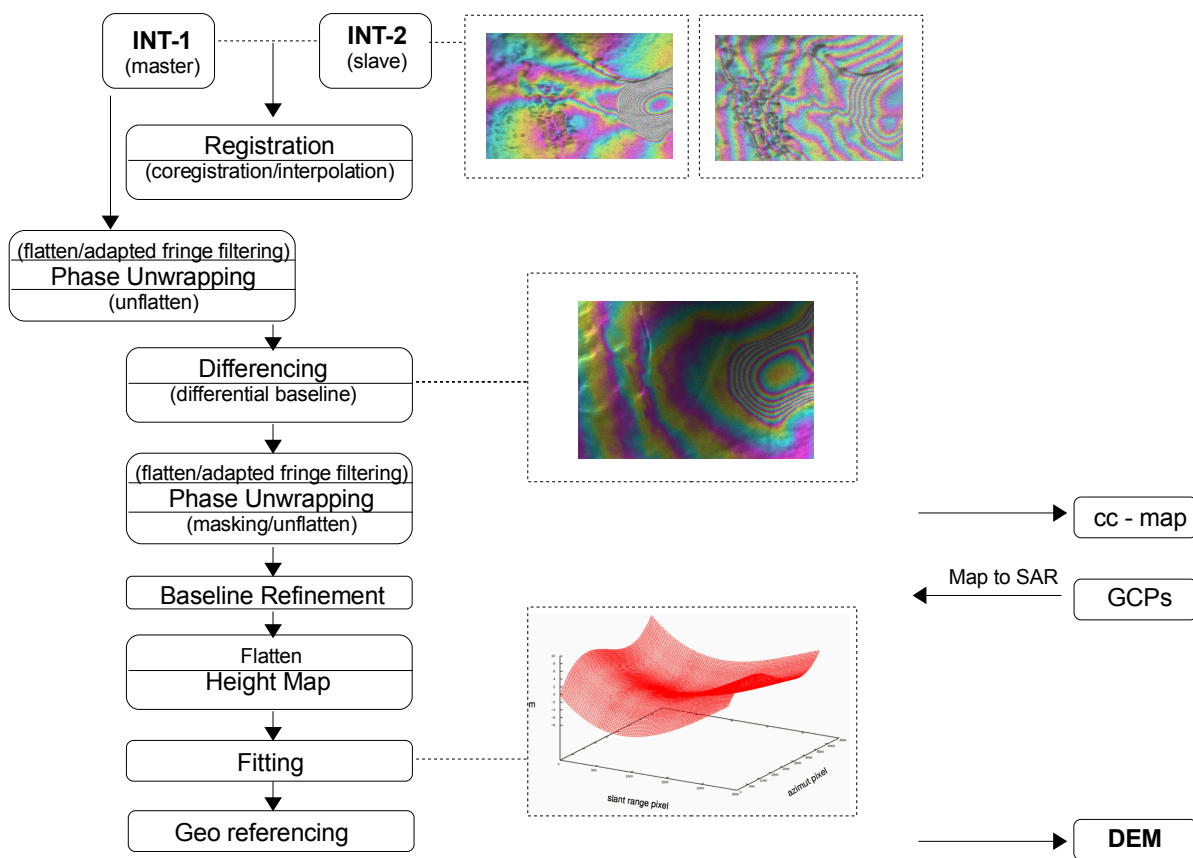
Figure 4.9: Flowchart for the DInSAR processing. Note that the beginning images illustrate the flattened interferograms. The processing is done with the unflattened ones. An alternative approach avoids the first phase unwrapping by directly subtracting the INTs

Figure 4.9 gives an overview of the individual DInSAR processing steps, which will be explained in the following. The processing starts with a **registration** of the incoming INTs (illustrated in 4.9 are the FLTs, to make it more descriptive), which is similar to

the registration process during the InSAR processing. Offsets are usually about 5 km in azimuth and about 0.5 - 1 km in range. A power-based registration is chosen. Now the master is flattened, and adapted fringe filtering is performed in order to prepare the phase unwrapping.

adapted fringe filtering · The algorithm computes the interferogram power spectrum through a fast fourier transformation (FFT). There, a narrow frequency band contains the geophysical information, and a broader frequency band contains noise. The aim is to lower the noise component and to estimate the coherence. The results is a coherence map as well as an interferogram with lowered phase noise. The coherence map (cc-map) serves as mask for the unwrapping, and it also plays and important role in the accuracy assessment later on. Through the filtering the number of residues is decreased. Residues are local regions, where a integration of phase values along a closed path does not yield zero. This becomes more clear in the phase unwrapping step. In an interferogram with overall good coherence and low noise the filtering should not be performed to strong, because some fringes might be eliminated. For more information see [GR98].

phase unwrapping · The phase unwrapping is an absolutely crucial step in the course of the whole processing. It resolves the problem that all phase values are wrapped in $[0, 2\pi]$ and finds the absolute number n of phase cycles $\phi_{unw} = \phi + n \cdot 2\pi$. A simple approach would be to add up the phase shifts between neighboring pixels under the assumption that these phase shifts are always smaller than π. If one single travel distance between pixel and sensor is known through a ground control point, then the whole phase of the interferogram can be unwrapped. As a control, the sum of phase shifts from neighboring pixels around a closed circle has to be zero. The large disadvantage of this method is that it needs an almost perfectly coherent image with no discontinuities. Additionally, errors in the phase of one pixel propagate through the whole interferogram. An example for a phase unwrapping error is shown in figure 4.10

In practice, there is a larger variety of different algorithms for this problem. Here a minimum cost flow (MCF) algorithm is used. The MCF problem is a very general problem from network theory. The idea is to calculate the minimum cost flow of goods in a network consisting out of sources and sinks. These are characterized through their capability of supplying or gathering goods respectively. The connection is via arks that have a certain arc capacity and a cost per unit flow. Nodes that are neither sources nor sinks are called transshipment nodes (or depots). The transfer from transportation problems to phase unwrapping can be made by assigning nodes to a number of pixels. If these are residues (closed sum of phase-differenes around these pixels is positive or negative), they become sources or sinks. The flow consists of 'packages' from $m \cdot 2\pi$ with $m = 1, 2, \dots$. Receiving a multiple of 2π causes a phase jump. Thus the cost per arc flow should be low close to places of discontinuities and high in areas of good coherence. To create a network a delaunay triangulation is used, where each triangle is a node in the network. The solution is based on a successive shortest path method but will not be further discussed here. For further reading please refer to [CW00]. Phase unwrapping demands the highest memory resources, and often the scene is subdivided into several
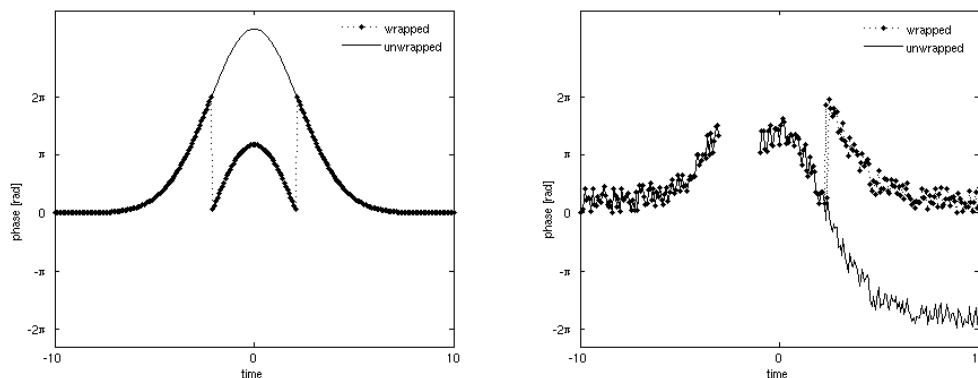
Figure 4.10: A smooth and continuous function (left) is usually easy to unwrap. More difficult are discontinuous and noisy functions (right), where unwrapping errors are more likely. In the example the unwrapping function in octave has been used.

patches to account for memory restrictions. However, if possible, the patches should be chosen as large as possible to avoid phase discontinuities. A general solution is often better than several sub solutions which are merged later on. The unwrapped scene will be called UNW.

After successful unwrapping, the UNW can be subtracted from the INT which needs to be unwrapped again. An alternative way is to subtract the INTs first. As seen in figure 4.9 the displacement was canceled by the subtraction and smooth topographical fringes are visible. After masking the ice shelf, which doesn't fulfill the constraint of constant displacement, the UNW is ready to be turned into a height map.

Baseline refinement · In order to refine the baseline estimate of the differential baseline, GCPs from IceSAT's laser altimeter are used. Ideally several IceSAT tracks cover the scene, which makes it possible to evenly reference the height map to the actual surface. This is done by adjusting the differential baseline via a non-linear least square algorithm. It is possible to adjust several components of the baseline, which is given in the TCN coordinate system. Usually all possible components are fitted. As can be seen in the processing example, this is an important step, since the differential UNW is tilted significantly and needs to be corrected with the help of GCPs. As it turns out, the baseline refinement is not always successful, and a systematic trend of deviations from the height-map to GCPs remains. This is part of the processing example as well, but for now it should only by noted that the height-map is fitted again with a second or third order polynomial. This is not necessarily part of the standard procedure.

Geo-referencing · After finding the best height map possible, the only task remaining is to map the height-model from rang-doppler coordinates into a earth fixed coordinate

system. The geo-referenced height map will be referred to as the DEM. In this study all DEMs are projected into a polar stereographic coordinate system (true latitude 71 S, central meridian 0 E, WGS-84 ellipsoid). A terrain corrected approach is chosen, where the interferometric derived height-map itself serves as an input. The accuracy of the procedure mainly depends on the accuracy of the recording geometry. But since no other external DEM is available, this is the best possible approach. The accuracy of the geo-referencing will be tested later on.

Now, the DEM is ready to use for the derivation of flowfields. During this study several partly overlapping DEMs were derived. A final DEM was created by mosaicking all single frames (see section 6.1). From now on the expression DEM refers to that mosaicked DEM.

4.5 Derivation of 3D-Flowfields

Literature

'Three-dimensional glacial flow and surface elevation measured with radar interferometry'
by Mohr J., Reeh N., Madsen S. in Nature Vol. 391, 1998

With an external (or through DInSAR) derived DEM it is relatively easy to calculate flowfields which show the displacement along the line of sight. Therefore the DEM is used to simulate a 'topography - only' interferogram with the similar geometry of the interferogram which contains the mixed contribution of topography and motion. A mere subtraction cancels the topographical part, and after another phase unwrapping step a 1D-displacment map is derived. A sample result can be seen in figure 4.11. The arrows indicate how the motion signal is lost if it contains strong perpendicular components. With a single interferogram it is not possible to map the full velocity field. However, it is possible to combine two flowfields to one 3D-Flowfield, which will be explained in the following. But first let's take a look accuracy requirements for the DEM:
 For that, the DEM, which was mosaicked from all available DInSAR scenes, is considered independent from the individual frames. An error s_h is assumed. In section 6.1 it is shown that in areas of high coherence this error is about ± 7 m. By simulating a topographical interferogram this error is scaled with the used baseline B. So, differencing not only yields the motion $\Delta\rho$, but also a residual height artifact. This introduces a residual phase (see height of ambiguity):

$$s_\Psi = \frac{4\pi}{\lambda} \frac{B_\perp}{\rho_0 \sin(\Theta)} s_h \qquad (4.29)$$
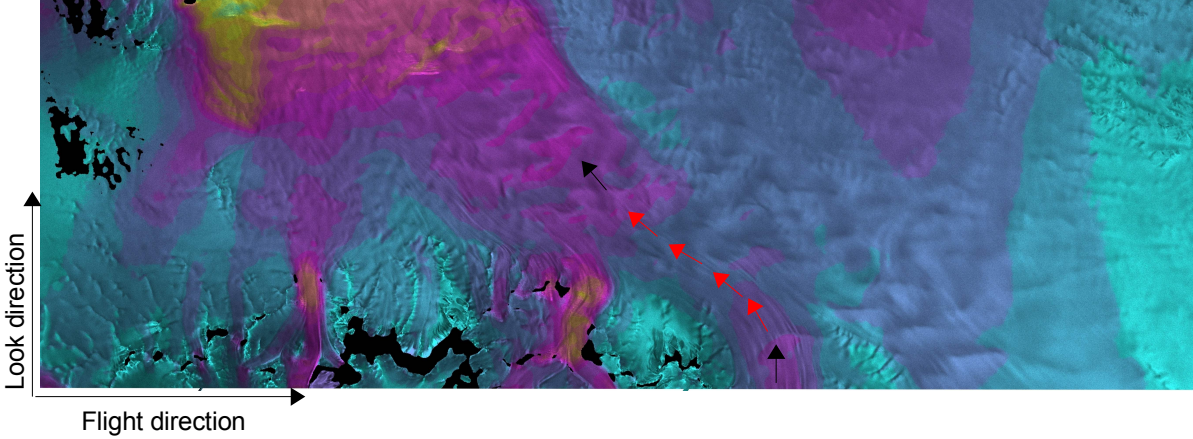
Figure 4.11: Displacement map of ascending orbit (track 035). The arrows indicate how the displacement signal is lost as it gets more perpendicular to the sensor's line of sight.

which is misinterpreted as motion. In this case the displacement d is given by:

$$d = \frac{\lambda}{4\pi}(\Delta\Psi_{mixed} - \Delta\Psi_{DEM}) = \Delta\rho \pm \frac{B_\perp}{\rho_0 \sin(\Theta)} s_h \tag{4.30}$$

which again emphasizes the importance of small baselines for motion mapping. However, assuming $B_\perp$ to be 100 m and a height error s_h of 10 m, this introduces an error in displacement of below a cm (with $\rho_0 = 800$ km and $\Theta = 23°$). If s_h is 10 to 15 times larger (which actually can be the case if other available DEMs are used) it is not negligible anymore.

However, more severe is the fact that only one component of the 3D-flowfield is known. This is addressed by the idea of combining two displacement maps from an ascending and a descending orbit [MJ98], as shown in figure 4.12.

In the overlapping areas, two components of the flowfield are known, because the look angles of ascending and descending orbits are complementary. As explained as well in [MJ97], it is easy to derive a full 3D-Flowfield with the assumption of a surface parallel flow. The corresponding linear system is given by:

$$\begin{aligned}
\Delta d_1 &= \vec{d} \cdot \hat{n}_{asc.} \\
\Delta d_2 &= \vec{d} \cdot \hat{n}_{des.} \\
\Delta d_3 &= \vec{d} \cdot \hat{n}_{surf}
\end{aligned} \tag{4.31}$$

where $\hat{n}_{asc.}$ and $\hat{n}_{des.}$ are the unit vectors along the two lines of sights and $\hat{n}_{surf}$ is the surface normal.

For the processing, the geocoded displacement maps of ascending and descending orbits are registered with a constant offset. Note that in the first case no differential pairs are
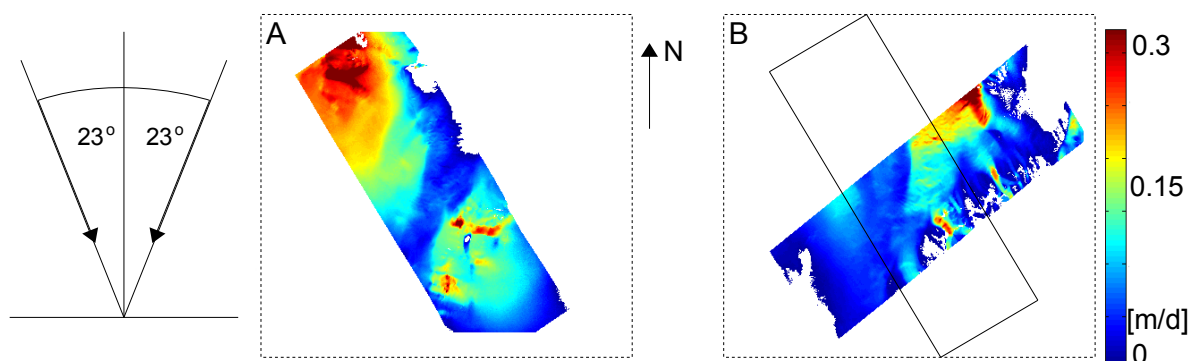
Figure 4.12: Displacement map of ascending (track 035) and descending orbit (track 017) which overlap in the vicinity of the Heimefrontfjella. Both maps comprise three frames of approximately (100 x 300) km^2.

needed for the displacement maps. It is also possible to use a single interferogram, as long as the mosaicked DEM covers the area. But despite of that, coherent pairs for that kind of combination are not as common. After the registration, the the two look vectors are calculated for each pixel. For the surface parallel flow assumption the gradient of the DEM is needed. After that the 3D-map is created.

The steep look angles of the ERS-satellites are not advantageous for that procedure, because the surface parallel component is larger then the two actually measured components. By knowing the accurate ice thickness, it is possible to replace the surface parallel flow assumption by principles of mass conservation. However, for now the surface parallel flow assumption will be used.

5 Error Propagation from the SAR Processing to the DInSAR DEM

This chapter displays some steps during the interferometric SAR processing and evaluates the estimation of critical parameters. Processing differences and errors are localized and assigned to the sources. The goal is to minimize the height difference from DInSAR-DEM and available GCPs (mostly from IceSAT's laser altimeter). These always represent the 'true' height here.

An indicator for processing errors are deviations in overlapping areas of different DEMs. If the corresponding frames rely on the same raw data, the uncertainty is entirely due to the processing. Basically every track offers the possibility to check for processing errors in that way, because tracks are subdivided in frames which overlap each other and are processed individually. Sometimes however, area is lost on the margins through filtering and phase unwrapping, and so not all frames can be used for that kind of a comparison. Especially interesting are frames which are available as SLCs from the German processing and archiving facility (D-PAF) as well as processed from Gamma's Modular SAR processor (MSP). The differences that occur in those pairs might be explained with different processing parameters during the SAR focusing step. It is also interesting to compare DEMs from different raw data sets, but there the error could be a mixture of 'internal' processing errors and 'external' errors like atmospheric phase delays.

There are several reasons why it is difficult to evaluate the complete DInSAR processing chain: The here used Gamma software is a commercial software package and the source code is not available at the AWI. It does offer a detailed documentation and support, together with the possibility to control intermediate results, however, as every software, it appears as a black box on a deeper level. It is not always straightforward to understand how the different parameters relate to each other, partly because of the black box effect and partly because of the complexity of the system. For a full understanding access to the source codes is necessary.

However, it is possible to visualize essential differeces between the processors and the resulting effects. In a first step, a small cross-compatibility test of the two different SAR processors (ESA/MSP) will be done. These differ for instance in the DC estimation, which leads to a tilt in phase as well as deviations in the geo-referencing. Possible correction are mentioned, but not tested in detail. Also the independently derived DEMs sometimes differ systematically compared with each other as well as when compared

with GCPs. The deviations thereby are usually in the order of ± 10m. In the end, the DEM was fitted to IceSAT GCPs with a third order polynomial to account for these deviations.

The quality of the DEM and flowfields is also influenced by external parameters, like atmospheric contributions, a varying penetration depths or a change in flow velocity. These contributions are difficult to handle because usually an interconnection of all external parameters leads to the observed error and it is difficult to uniquely assign them and even more difficult to think of a correction. This will be done during the evaluation of the geophysical product in the following chapter. For now the focus will be on the processing.

5.1 The Doppler Centroid and Phase Stability

In [AB96] Barmettler et al. looked at the cross compatibility of ERS-SLCs from different PAFs and their respective SAR processor. They did find differences, but as an overall result it is stated, that the user must not care which PAF processed the data. However, only two pairs were assessed and none of them was recorded on the southern hemisphere and contained large and featureless ice-sheets. This will be done now. As examples serve ESA-SLCs from the D-PAF as well as SLCs processed with the MSP, which will be referred to as Gamma-SLCs. Right from the beginning it should be stated that it is not the goal of this section to favor a certain PAF or SAR processor, but rather to raise the consciences for some problems and effects introduced through the processing.

As can be seen in table A.4 in appendix C. various parameters of the focused SLC differ: Start and stop times are not harmonized, the scene center deviates as well as the incidence angle, the range dependency of the DC is represented with different order polynomials and also state vectors are interpolated at different times. However, not all parameters can be compared directly as for example the DC is given for different scene centers. The table only serves as an example of a certain pair. From now on examples from other pairs will be chosen as well, depending on where the differences are most obvious.

As a motivation for this paragraph serves figure 5.1, which shows a profile across the overlapping area of two adjacent DEMs. The overlap consists out of exactly the same raw data and differences in the DEM can be entirely attributed to the processing. In order to explain these deviations the processing parameters for the respective SLCs are compared.

In the beginning it is thereby noticeable that the SLCs processed by ESA and the MSP have different scene centers. These are not directly comparable, as for example the MSP sometimes processes a larger cutout of the raw data then the ESA-SLCs. But still, small
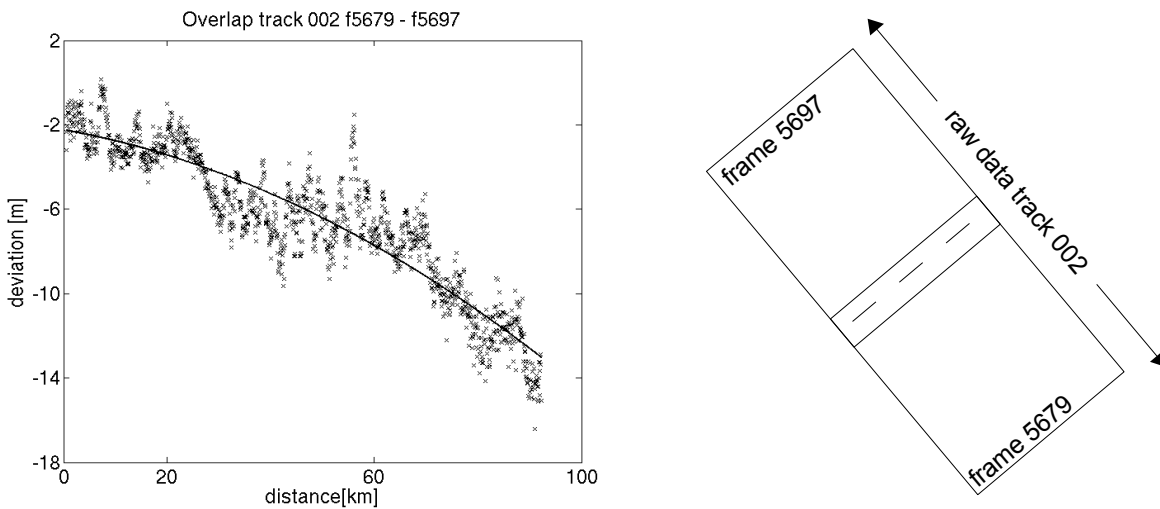
Figure 5.1: [track 002 frame 5679-5697 (ESA)]The plot shows deviations of DEMs along a profile in slant range which was taken in the overlapping area of two adjacent frames from the same raw data. This is an example for a DEM which was derived from ESA-SLCs.

differences in the geo-referenced power images are visible. As an example, two distinct points of the power image of track 460 and frame 5679 (which is available as ESA-SLC and processed from the MSP) are compared with each other and with the Radarsat Mosaic from the Antarctic mapping mission (R). The results are displayed in table 5.1. It becomes evident, that the two SLCs coincide within 100 m or less. Compared to the Radarsat Mosaic the deviation is in the order of 0.5 km. The reason for this is probably that the DEM used for the geocoding of the Mosaic is not as good as the DInSAR DEM. For a more detailed analysis more points and frames have to be looked at, but in order to assess the order of magnitude this will be enough.

The location of scene centers and so the geo-referencing depends, amongst others, on the estimation of the DC and its range dependency. For the processing with the MSP the Doppler ambiguity was estimated with the help of the MLCC algorithm, whereas the DC itself was derived by a magnitude based approach as described in section 3. The range dependency was added by a line to line correlation method which is implemented in the MSP as well. If the range dependency is neglected and only a constant value is assumed, the deviation of the geo-referenced amplitude image are in the order of 1.5 km which emphasizes the importance of a correct Doppler polynomial. The slave of the interferogram was processed to the master's Doppler polynomial (see also 3 or [Han01], chapter 2). Together with its differential partner interferogram it was used to derive the DEM, which is needed for the geocoding.

The DC polynomials (ESA/MSP) of the same track and frames are compared in figure (5.2). Since the DC is given for the scene center, it is necessary to transform the

p	$°S$(MSP)	$°W$(MSP)	$°S$(ESA)	$°W$(ESA)	$°S$(R)	$°W$(R)
1	72.1870	3.4492	72.1862	3.4475	72.1894	3.4585
2	71.9412	6.0103	71.9399	6.0085	71.9383	6.0137

p	Δ_{MSP-R}	Δ_{ESA-R}	$\Delta_{ESA-MSP}$
1	0.41km	0.51 km	<0.1 km
2	0.34 km	0.26 km	<0.1 km

Table 5.1: Deviations of two distinct geo-referenced points in track 460 frame 5679. Compared are two different SLCs from the same scene (ESA/Gamma) with each other and with the Radarsat Mosaic (R).

polynomials to the same scene centers for the comparison. If no change in azimuth directions is assumed, it suffices to transform to the same scene center in range direction. The transformation is explained in appendix B.. It alters the coefficients very little. However, since the scene center of a raw image differs from the scene center of the processed SLC it is a handy transformation in case it is required to exactly process the SLC to a certain DC.

Figure 5.2 displays that the DCs vary in their range dependency as well as in the absolute value at the scene center. Inverting equation 3.20 indicates how these differences influence the estimation of the squint angle Θ:

$$\Theta = \sin^{-1}(\frac{f_{DC}\lambda}{2v_{res}}) \tag{5.1}$$

The MSP estimates a relative velocity v_{res} of 7524.67 $\frac{m}{s}$. With a wavelength of 5.7 cm, a DC of 70 Hz corresponds to a squint angle Θ of 0.0149 °. A DC of 120 Hz corresponds to $\Theta = 0.0256°$. Looking at figure 5.2 on the right it is obvious, that different squint angles lead to a different magnitudes of the SAR look vectors. This difference can be calculated from the geometry. Assuming R_0 to be 875 km, the difference (in slant range) at the scene center is then given by

$$\Delta R(r) = R_0 \left(\frac{1}{\cos(\Theta(r))} - \frac{1}{\cos(\Theta'(r))} \right) \approx 0.058m \tag{5.2}$$

Projected onto a flat earth, the difference in azimuth direction is given by:

$$\Delta y = R_0(\tan(\Theta) - \tan(\Theta')) \approx 163m \tag{5.3}$$

It should be mentioned, that not only the squint angle Θ, but also the look angle γ shows deviations of $\gamma_{MSP} - \gamma_{ESA} = (23.476 - 23.466)° = 0.01°$. With the same equations this leads to $\Delta R = 70$ m and $\Delta x = 176$ m in range direction.

So the deviations in geo-referencing in table 5.1 can at least partly be attributed to
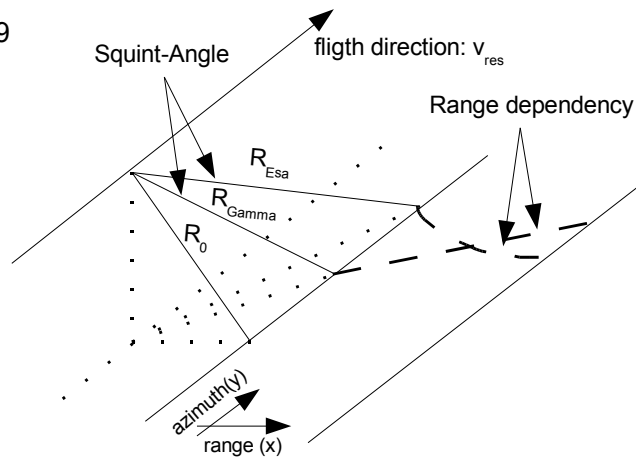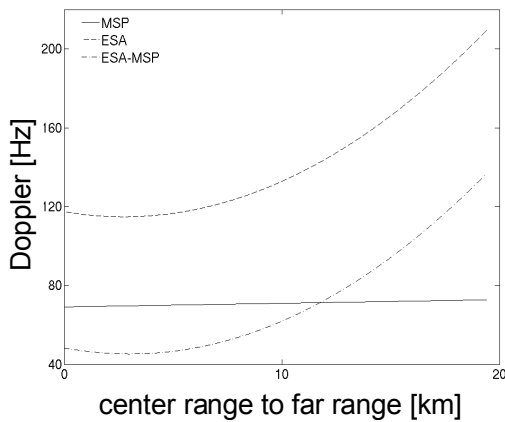
Doppler Polynomials of track 460 frame 5679

Figure 5.2: Schematic illustration how the Doppler Centroid translates directly into the squint angle.The MSP usually assumes the slant range dependency to be linear whereas the ESA-SLC is processed with a quadratic dependency, as indicated in the scheme on the right. This is an example for ERS-1.

an imprecise estimate of DC, which leads to a misplacement in azimuth. For a better estimate it would be necessary to know which relative velocity is estimated for the ESA-SLC. This parameter is not distributed with the focused D-PAF SLCs.

Other pairs show larger variations in the DC estimation, but the difference usually never exceeds more than 300 Hz, assuming the SLC is processed to the right ambiguity. If the wrong ambiguity is selected, the difference is in multiples of the PRF (1659Hz). A deviation of 300 Hz leads to misplacement in ground range of about 1 km, if the wrong ambiguity is estimated it jumps to several kilometers. This is a way to check, whether the right ambiguity is selected or not.

An offset in range direction is partly caused by different estimations of the SAR look angle γ. For this angle no range dependency exists as one of the processing parameters, but from the geometry it is clear that it varies in between 19 - 25 ° from near to far range.

How do these differences propagate into the phase information of an interferogram? This mainly depends on the internal processing of the SAR processors. The following paragraphs derive some properties from the geometry, however, it is unclear how the internal processing is actually implemented. An inquiry at the D-PAF revealed that the phase is essentially independent of the DC, because these are processed to a zero Doppler geometry. The range and azimuth spacing is thereby determined by the PRF and the range sampling rate, which in the end determines the phase values of the grid cells. This is not the case with the Gamma-SLCs. These are not processed to zero Doppler, but to the center of the footprint. In that case, a DC dependency of the image phase exists, which can be shown by manually changing the range dependency of the DC

during the processing. In the following paragraph this dependency will be derived from the geometry. It also includes a phase correction to a zero Doppler geometry, however, it is unknown, if the actual processing to zero Doppler is done in the same way.

To illustrate the observed effect of the DC to the image phase, it is helpful to remember that an interferogram displays phase differences. A constant offset, as given by a constant offset of look angles γ and γ', translates modulo 2π into a constant offset in an interferogram. This leads into difficulties if height information is to be extracted without any GCPs. However, this is not the case so far, and with the use of GCPs as tie-points this offset can be corrected easily. More interesting are parameters with a range or azimuth dependency, as the squint angles (and thus the DCs) in equation 5.2. In that case the phase difference $\Delta\Psi$ is not only $\frac{4\pi\Delta R}{\lambda}$, but it has an additional term with

$$\Delta\Psi_{\text{res}} = \frac{4\pi\Delta R(r)_{res}}{\lambda} \tag{5.4}$$

This can be pictured with the scheme in figure 5.2: A deviation in squint angle leads to a different length of the SAR look vector and so ΔR changes to $R + \Delta R_{res}$. This needs to be multiplied by 2 to account for two way travel time.

If the difference in range dependency is linear, the residual phase is observed as a ramp in range. Strong non linear components introduce a non linear residual phase pattern in an interferogram.

This can be visualized in so called *Auto-interferograms* (A-INTs). where an interferogram is formed from two SLCs of the same raw data. In theory this means that $\frac{4\pi\Delta R}{\lambda} = 0$, and in an ideal world no fringes should be visible. The fringe pattern that remains in the INT can be entirely attributed to differences in the raw processing. If fringes are seen in the FLT, a non zero baseline was subtracted during the flattening. This points to difficulties in the choice of state-vectors, where the baseline is derived from and belongs to the InSAR processing. The dependency of the image phase with the DC in case of Gamma-SLCs can be shown with these A-INTs.

The A-INT in this example, is generated from an ESA-SLC and a Gamma-SLC of track 460 and frame 5679. The FLT of the A-INT from track 460 is zero with a zero baseline as expected. This shows that the choice of state vectors is a more stable step, because the ESA-SLC and the Gamma-SLC have different state vectors interpolated at different times, but it leads to essentially the same baseline.

The A-INT of the Gamma-SLC with the ESA-SLC shows a residual phase ramp in range with no azimuth dependency (see figure 5.3 on the right). This phase ramp can be possibly explained by the two estimated DCs and their range dependency:

The difference off the DCs in figure 5.2 shows a quadratic range dependence, after both DCs were transformed to same scene center. This means that the difference in magnitude of the SAR look vector, which can be calculated with equation 5.2, shows a non linear behavior along range as well. The induced residual phase difference is calculated with equation 5.4 and also shows a non linear behavior. The magnitude thereby changes from near range to far range in the order of 0.6 fringes. This is an extremely small value
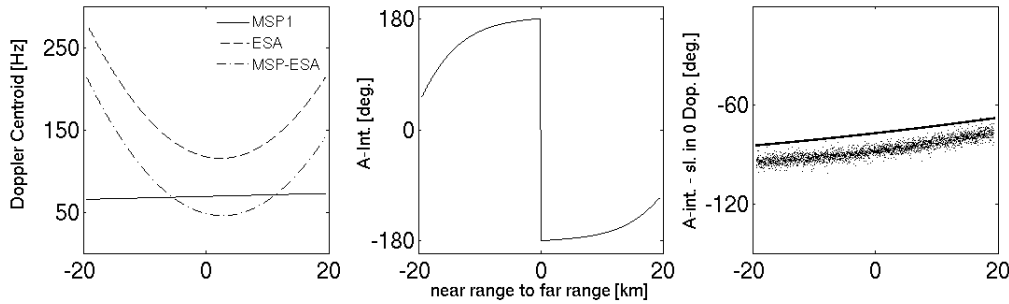
Figure 5.3: [t460 f5679] **left:**Differences in DC from near to far (slant) range. **middle:** Residual phase centered in footprint. **right:** residual phase ramp, with slave in zero-Doppler geometry. The continuous line is the predicted result for a flat earth, the dots the actual A-Int.

considering the magnitude of the various look vectors, but on the other hand the procedure is very sensitive with respect to changes in phase. The so calculated residual phase only includes deviations in the DC polynomials and exhibits a somewhat quadratic range dependency (see figure 5.3 in the middle). It does not match the actually observed phase ramp in the A-INT. For a better approximation, it needs to be taken into account that the ESA-SLC is processed to zero Doppler. In order to analytically explain the form of an A-INT from ESA-SLC with Gamma-SLC, the phase of the Gamma SLC needs to be corrected to zero Doppler geometry as well. This can be done with the same equations mentioned above. After this, the analytically calculated phase matches the observed residual phase of the A-INT quite well. This is displayed in figure 5.3 on the right.

The fact that no azimuth dependency is observed, justifies the assumption of a basically constant DC in azimuth direction (or at least both SAR processors estimate equal azimuth dependencies). For the analytical derivation of the residual phase in range a flat earth was assumed so far. In order to improve the result, the earth curvature needs to be taken into account. Also differences in the estimated relative velocities between platform and earth were not taken into account because it is not available for the ESA-SLC. However, the analytical derived phase ramp and the actually observed phase ramp are very similar. This suggests that the DC is the main parameter in terms of the phase stability, but as mentioned above, the derivation from the geometry not necessarily represents the way it is implemented in the SAR processors. Since the DC of the ESA-SLCs cannot be altered, it was not possible to check whether the image phase is actually independent of the DC or not. However, this was done in case of the Gamma-SLCs and the derivation from the geometry proved to be a good way to describe the observed phase ramps in the corresponding A-INTs.

In real life no A-INTs are formed but INTs from ERS-1 and ERS-2. It is suggested, to process both SLCs to the same Doppler as mentioned before, however, if the already processed SLCs from the PAFs are used, this is not the case. So, under the assumption

that each SLC is afflicted with a certain residual phase (because of the DC estimation or because of other processing errors), the residual phase of the corresponding INT can be written as:

$$\Delta\Psi = \frac{4\pi\Delta R}{\lambda} + (\Psi_{m,res} - \Psi_{s,res}) \tag{5.5}$$

where the indices for m and s depict master and slave. This means that the individual residual phase patterns of the single SLCs are combined and lead to a general tilt of the interferogram. In order to assess if this effect causes the systematic deviation in figure 5.1, also the baseline has to be taken into account. This is done in section 5.2. In the remaining part of this section it will be discussed if the DC estimate can be iteratively improved using GCPs. The implementation and evaluation remains however a possible task for the future.

The **deviation in phase** and the **deviation in ground range** location offer, at least in principle, the option to iteratively improve the DC estimate. The tilt in phase can be exemplified by transforming GCPs into expected phase values. A 2D - interpolation of the residuals with the unwrapped phase of the INT, illustrates the tilt. The problem is that a single INT has a mixed phase of topography and displacement. The displacement might be distributed over the complete frame and before a DInSAR approach no GCPs can be chosen. However, the tilt of the differential INT is interesting as well. It is displayed in figure 5.4 for an MSP pair and for an ESA pair of the same scene. The plot displays the differential tilt as the differenced single tilts from the two incoming INTs. These single tilts are again caused by the individual tilts of the single SLCs. So all together 4 individual tilts lead to the tilt observed in the figure 5.4. It is not self-explanatory how to assign individual corrections to every single tilt, but the the differential INT could be fitted to the GCPs.

Another options could be to adjusted the incoming INTs. Therefore it is necessary to derive in a first run a displacement field in order to mark the areas of high displacement. Then, GCPs can be chosen with a threshold so that only areas with no or very little displacement remain covered. Depending on the amount of leftover GCPs, a fit of a polynomial in range can be used to to determine the theoretical offset from the original DC estimations. One problem is that usually not mainy GCPs remain and it is questionable if the fit is precise enough to improve the DC estimate.

As a second approach the deviations in geo-referencing could be used for an adaption. This is definitely suitable to check the doppler ambiguity number. The assessment done above shows, that in the case of a wrong ambiguity the offset is in the order of kilometers. A simple comparison to the Radarsat Mosaic for example reveals these differences. More difficult seems the adaption of the fractional part. There the differences in the geo-referencing are in the order of 100 m. In order to compare landmarks, it is preferable to sample the image to a higher pixel spacing (50x50). So the offset is in the order of a few pixels. The geo-referencing of the Radarsat Mosaic is not precise for a comparison, and other points with GPS measurements have to be used.
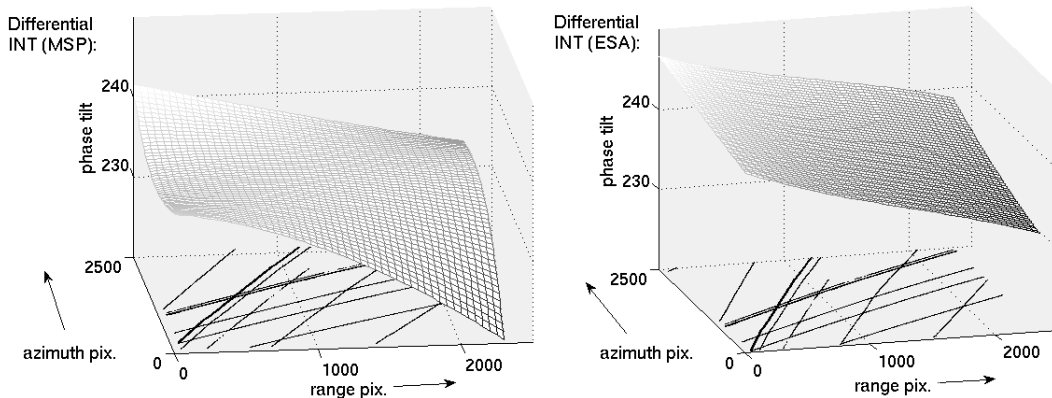
Figure 5.4: [t460 f5679] **left:**Tilt of differential unwrapped INT from MSP pair **right:** Tilt of differential unwrapped INT from ESA pair. Available IceSAT tracks are projected onto the ground.

The question, whether to pursue the idea of an iterative approach or not also depends on the accuracy requirements of the DC. As a rule of thumb the DC-estimate should approximate its real value by 5 % of the PRF ([IC05] on page 492). So in our case a deviation of more than 83 Hz should be avoided. For the small data set here where two different Doppler estimators are available, this is virtually never the case. This could be partly due to the larger squint in the southern hemisphere, and the large number of scenes with low contrast.

What certainly always calls for a correction is if one of the SLCs is processed to the wrong ambiguity. This not only affects the geo-referencing but also the quality of the overall DEM deteriorates with deviations up to 60 m. Such an error can be visualized by the error in geo-referencing, but for the correction it seem easier to use a different DAR (or to manually adjust the ambiguity number), instead of an analytical correction from the offset in space or phase. But also if the right ambiguity is selected, some interferograms seem to have a ramp in range over several fringes. It resembles the ramp from figure 5.3. It becomes evident if explicit flat areas (such as shelf ice) are covered with several fringes. Depending on the baseline this could be theoretically caused by a real tilt through tides, but it also often indicates a wrong Doppler.

So does an error in the fractional DC propagate into the final DEM? Or is it corrected entirely through the baseline refinement? It was shown, that the DC estimation can lead to a residual phase behavior in range direction. The original plot of deviations in the DEM in figure 5.1 also exhibits a strong range characteristic. In order to relate that, the baseline needs to be included.

5.2 Mixing of phase ramps and baseline errors

In order to see how phase ramps or imprecise baseline models propagate into an error in height z, it is helpful to invert equation 4.16 under the assumption of zero displacement:

$$z = \frac{\lambda \rho(r) \sin(\gamma(r))}{4\pi} \frac{\Delta\Psi}{B_\perp} \tag{5.6}$$

where $\gamma(r)$ is the look angle and $\rho(r)$ the length of the look vector. This allows to convert phase information into height information. Lets assume that baseline as well as phase are flawed to a certain extent. The deviation in height, that is caused by a deviation between 'true' baseline B and estimated baseline B' as well as 'true' phase $\Delta\Psi$ and estimated phase $\Delta\Psi'$, is then given by:

$$\Delta z = z - z' = c(r) \cdot \left(\frac{\Delta\Psi B'_\perp - \Delta\Psi' B_\perp}{B_\perp B'_\perp} \right)(r) \tag{5.7}$$

The factor c(r) is thereby given as:

$$c(r) = \frac{\lambda \rho(r) \sin(\gamma(r))}{4\pi} \tag{5.8}$$

and it is assumed that it is not affiliated with errors. The parameter r depicts the range dependency. For small errors of $\Psi_{res} = \Delta\Psi - \Delta\Psi' \approx 0$ or $B_{\perp,res} = B_\perp - B'_\perp \approx 0$ equation 5.7 decouples to:

$$\Delta z = c(r) \frac{\Delta\Psi_{res}}{B_\perp} \tag{5.9a}$$

$$\Delta z = c(r) \Delta\Psi \frac{B_{\perp,res}}{B_\perp B'_\perp} \tag{5.9b}$$

So in principle it should be possible to estimate errors in the height model due to an imprecise baseline and a residual phase ramp. These parameters are directly accessible in the situation depicted in the beginning of the chapter in figure 5.1: Two overlapping frames from the same track should have the same phase and baseline model in their shared raw data. The overall residual phase (which consists out of the contributions from 8 SLCs) can be obtained by differencing the flattened, unwrapped differential FLTs in the overlapping area. The two baselines are given in an earth fixed coordinate system (TCN) with a linear parameterization over time in azimuth. The perpendicular baselines have a range dependency due to the range dependency of the corresponding angles. For this test case, the perpendicular baseline was calculated for a series of points with the Gamma software, and the linearly interpolated in both directions. As test data serves again track 460 with its frames 5679 and 5697, in this case processed from the D-PAF. The perpendicular baseline is approximately 160 m.
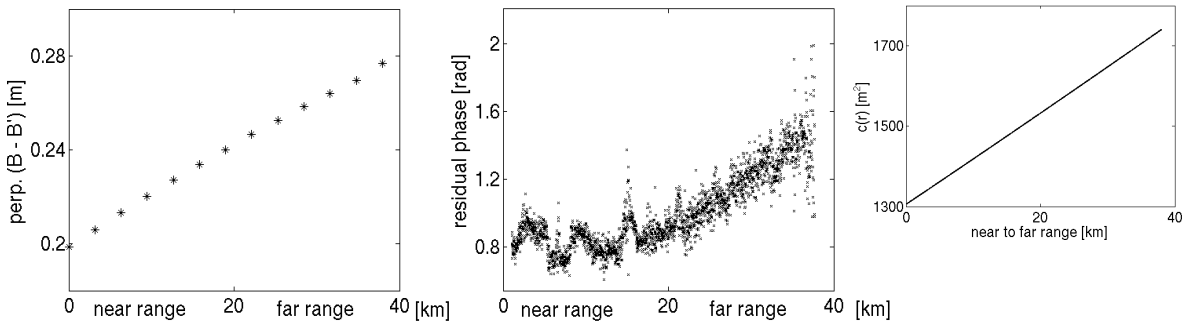
Figure 5.5: [t460 f5679 and f5697] Absolute differences in perpendicular baseline and residual phase along range. Profiles are in overlapping area from different frames of the same track. The top right plot shows the factor c(r) in range.

The comparison is performed in radar coordinates. Therefore it is necessary to first calculate the offset of frames in pixels. In principle this can be done with a cross-correlation of the power images, but since the overlapping area is often too small for this (typical values are 80 x 2450 pixels with a 2x10 multi-looked power image), the offset can also be estimated from orbital parameters. This results in a constant offset. As a control the power images can be appended with that offset. Usually the resulting discontinuities are hardly visible and in the order of a few pixels. Since the terrain height varies only slowly in this example, this is for sure a good enough fit to avoid phase differences due to an imprecise offset estimation. The offset of frame 5697 relative to frame 5679 is here estimated to be 2507 pix. in azimuth and -44 pix. in range, whereby all images are multi-looked with 2 looks in range and 10 looks in azimuth. The extent of the overlap is (80 x 2406) pixels.

In terms of the baseline the refined and the original baseline can be used for a comparison. In plot 5.5, the refined baseline was taken. It is the result of the least square estimator *base-ls*, which is implemented in the Gamma software. It uses GCPs to adapt the baseline and to calculate a phase unwrap constant.

In order to calculate c(r) a look angle of 23.15° was assumed at the scene center. The look vector varies from 855.646 km in near range to 894.372 kilometers in far range. A simple geometric calculation tells then that the look angle γ varies from 19.9° to 25.9°. Together with the fixed wave length of 5.6 cm this defines c(r). Now it is possible to compare the theoretical height error from equation 5.7 to the actual height error which was extracted in the same way as the residual phase.

Figure 5.5 displays the residual phase ramp (right) as well as differences in the perpendicular baseline (left) for one range line in the overlapping area. The two refined baselines have an offset of about 20 cm and vary 8 cm along range. The residual phase is noisy, but exhibits an almost linear range characteristic of approximately 0.13 fringes. The azimuth extent of the overlap is small, and in that interval no azimuth dependency
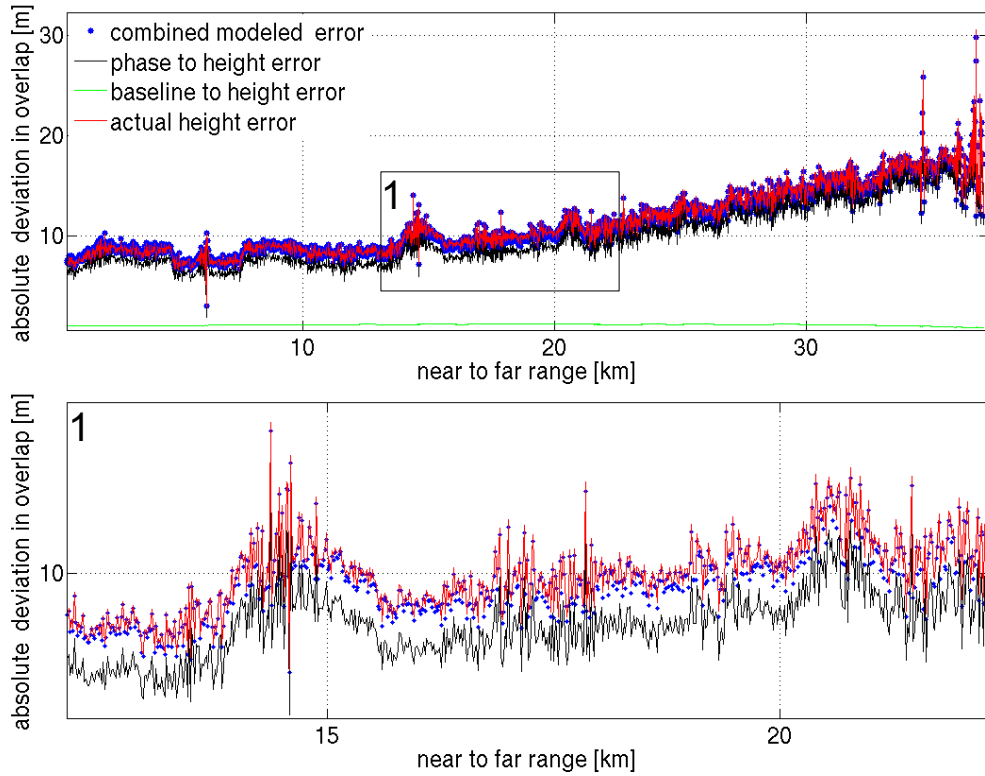
Figure 5.6: [t460 f5679 and f5697] Deviations in overlapping area from different frames of the same track (red). The blue dots represent the modeled error according to equation 5.7. The green line is the introduced error due to differences in the baseline model, the black line represents the error introduced through a residual phase of the two unwrapped differential FLTs. It becomes obvious, that the phase is the dominant factor for the overall error.

is observed. Therefore the discussion focuses now only on range dependencies.

With the equations 5.9a and 5.9b it is possible to simulate indvidual erros due to baseline and residual phase. With equation 5.7 the combined error can be calculated. Figure 5.6 illustrates the results for the used example of track 460. It is visible that the actually observed error fits very well to the modeled error. The phase error thereby dominates to a large extent the shape and magnitude of the deviation. The error introduced through the baseline basically results in a constant offset with an almost negligible range dependency. This can be understood by looking at the magnitude of c(r) and at the equations in 5.9: A relative change in phase of 0.8 rad results with a perpendicular baseline of 160 m in a factor of $5m^{-1} * 10^{-3} * c(r)$ which is about 6.5 meter. A relative change in baseline of 20 cm however only leads to $1m^{-1} * 10^{-4} * c(r) \sim 1m$ deviation. However, this also depends on the actual terrain height which is represented in the unwrapped phase of $\Delta\Psi$. It can vary over several order of magnitudes. The factor c(r) generally

has an amplifying function from near range to far range.

Theoretically it is possible to model the residual phase pattern, which is observed in figure 5.5. Therefore one needs to calculate every single tilt as it was done in the preceding section. If this is done for this example an overall residual phase ramp of 0.08 fringes is actually calculated, which is slightly lower than the observed value. The problem with this estimation, apart from a possible azimuth dependency of the DC, is that only an approximate relative velocity v_{res} is known. This parameter influences the slope of the ramp and so the ramp cannot be modeled exactly.

So far only range dependencies were considered. During a comparison to GCPs also a systematic azimuth dependency is sometimes visible. This is harder to examine, because the approach of using overlapping areas for the evaluation is not possible. However, the same two parameters baseline and DC are likely to be the reason for that as well.

In order to deal with this effect, either a better baseline model or DC estimate have to be used, or the systematic trend is visualized with a comparison of GCPs. This enables a fit of the height model which will be done in the following.

5.3 Correction with Using Ground Control Points
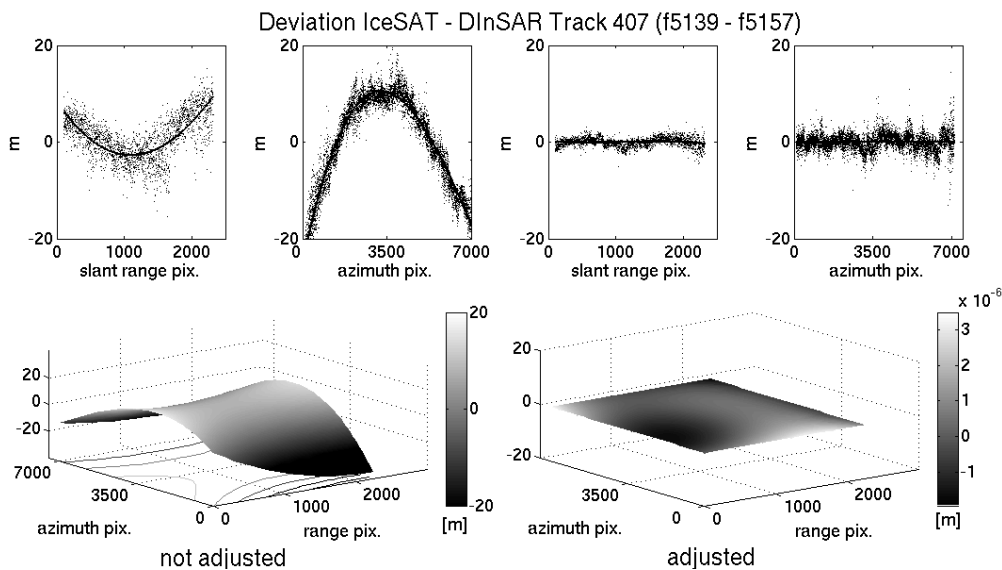

Figure 5.7: [t407 f5139 - f5175] Systematic deviations in azimuth as well as in range are observed when comparing this height model to GCPs (left). In both directions quadratic dependencies exist and a 2D-polynomial is used to adjust the height model (left). This is an extreme example, in other frames the azimuth dependency is usually smaller than the range dependency

As discussed in the last sections, a systematic error can be introduced through the processing due to incorrect DC estimates and baseline models. Only a range dependency was considered, but also azimuth dependencies can be observed. In order to account for these deviations the height model was fitted to the available GCPs within the scene. An extreme example is shown in figure 5.7. The deviations in range vary between ± 5 m in azimuth the deviations are 4 times as large. It should be noted that these deviations are the largest observed in the complete data set. Other height models sometimes show no, or only very little deviations in azimuth and the fit basically only affects the range direction. It should be noted that the fit globally adjusts the model, local deviations towards the GCP profiles remain and are only changed in their magnitude. The original height map is stored for later considerations on this topic.

For the fit, all GCPs within the same range bin are averaged, and an average error for every range line is assigned. The same is done in azimuth direction. These averaged errors are used for the fit of a third order 2D-polynomial. Most of the time a second order polynomial would be enough, however, some scenes (for example track 002 f5697) show two turning points and so for the general case a third order polynomial is assumed. By fitting the data to the GCPs it is possible that actual physical reasons for the deviations are flattened and not visible later on. Therefore it is necessary to emphasize that the procedure only makes sense if systematic trends are visible, which are believed to be rooted in the processing, or if the only goal is a precise DEM.

In the case of track 407 above, the deviations clearly show a systematic nature. It could be a connection between imprecise baseline and DC, together with a quadratic phase error mentioned in [IC05] on page 586. Later on track 031 is considered, and there also a residual pattern is observed, but in this case it is more likely that the problem is introduced through atmospheric contributions. A too strong flattening with a polynomial of higher order would remove this effect and valuable information is lost. So generally this step should be done with care, and if adjusting the processing parameters is feasible this should be preferred. However, in most case the removal of lower order trends in the height model improves its quality which can also be shown if a second set of GCPs (for example GPS measurements) is compared to the DEM before and after adjusting.

After the fit of the height model to the GCPs, the deviations are still not entirely random as could be suspected by looking at the two top right plots of figure 5.7. This is the topic of the next section.

5.4 Local Deviations in a Global Fit to GCPs

A perfect height model should exhibit no systematic deviations to the corresponding GCPs, and only deviations due to random noise should be visible. This is not always the case here, even after the DEM was fitted with a 2D-polynomial to account for differ-
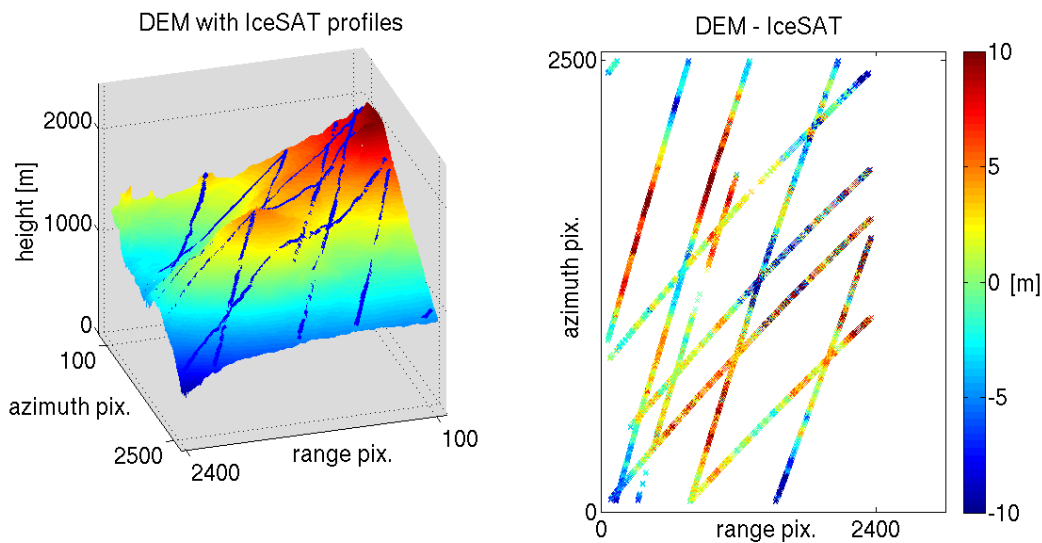
Figure 5.8: [t460 f5679] After fitting the frame to the GCPs localized deviations remain. On the right longer strips of positive deviations are followed by longer stripes of negative ones. The color coding is chosen to emphasize that effect, the scene covers about (100x100) km^2

ences in the processing. This becomes evident when looking at figure 5.8. If the single IceSAT profiles are being considered, longer stripes of positive deviations are followed by longer stripes of negative deviations. This is a wavelike structure on smaller scales. Two reasons are likely for a explanation:

First, the differences can be attributed to a local change in penetration depths. This is also topic of the following chapter. A local change of penetration depths can be caused by a local change of snow morphology. The penetrations depth varies in between 0-20 meters and depends mostly on the snow's water content. The order of magnitude could explain this localized deviations.

Secondly it could be caused by an actual change of height, since the IceSAT profiles are from 2003 and the DEM is from 1996. However, although accumulation rates are higher on the coast than further inland, an actual change of height in that order of magnitude seems rather unlikely.

The problem is to distinguish between these two effects. An analysis of the reflectivity pattern which is visible in the power image could help for such a distinction. However, this is not the focus of this study and it will not be done here. What needs to be kept in mind is, that an average value of deviations between IceSAT profiles and the DEM may be small, but averaging is not the best way of assessing the overall accuracy. It is better to really look at the available GCP profiles and estimate the error according to those. In the case of figure 5.8 an overall error of ± 10 m should be assumed.

5.5 Summary

Let's summarize the result of the last sections: Through an example it was shown, that a systematic height error can be introduced through the processing. The height error was observed with SLCs processed with the MSP as well as with SLCs from D-PAF. It is caused by a residual phase pattern which is likely to be introduced through an imprecise estimate of the DC. Together with deviations in the baseline model, this error can be in the order of 10-15 m in far range. The DC should be accurate within 80Hz, and through the comparison of different Doppler estimators it became evident that this is usually not the case with scenes considered in this study. This might be connected with the higher squint of the ERS satellites in the southern hemisphere, as well as with the limitation to fewer Doppler estimators because scenes with relatively low contrast are being considered. Possible ideas to iteratively improve the DC estimate were given and might be tested in the future.

During this study other parameters where examined as well: It was checked whether it matters which GCPs are chosen or not because it could be possible that GCPs in areas of high displacement are not preferable even after the double differencing. However, no real effect was observed and so only GCPs over the ice shelf were masked.

By means of a cross-correlation it was investigated if the transformation of GCPs from map to radar coordinates which is needed for the baseline refinement was good. Therefore the GCPs were first shifted with a constant value and then rotated for every shift and compared to the existing DEM. However, for the examples available the best result was always with no shift and zero degrees rotation.

In order to check the assumption of constant displacement and other sub-steps in the double-differencing, the whole DInSAR procedure was performed iteratively. Therefore a height model was derived in the first run, which was then used to simulate topography only interferograms for master and slave. These were then used as input for the next DInSAR procedure. Already after the second step the procedure should stop, because topography only interferograms are subtracted from each other. In case the DEM contains leftover displacement fringes, this would be scaled into the topography only interferograms and should be visible in the outcome of the second step. However, usually a residual ramp is carried through, but no specific deviations in the surrounding of glaciers were visible. This approach was also thought of as a possibility to automate the choice of GCPs and might be taken up again later on. In this study it didn't proof to be a very effective tool.

As a summary of the processing example, it can be said that baseline and DC are the most important parameters. If these are correct, and the DEM is fitted to the GCPs the

error should be below 7 meters. It then probably only depends on external effects. What was not mentioned so far is, that In scenes with low coherence the phase unwrapping might lead to discontinuities as well. This can mostly be corrected if the range and azimuth patches are chosen large enough.

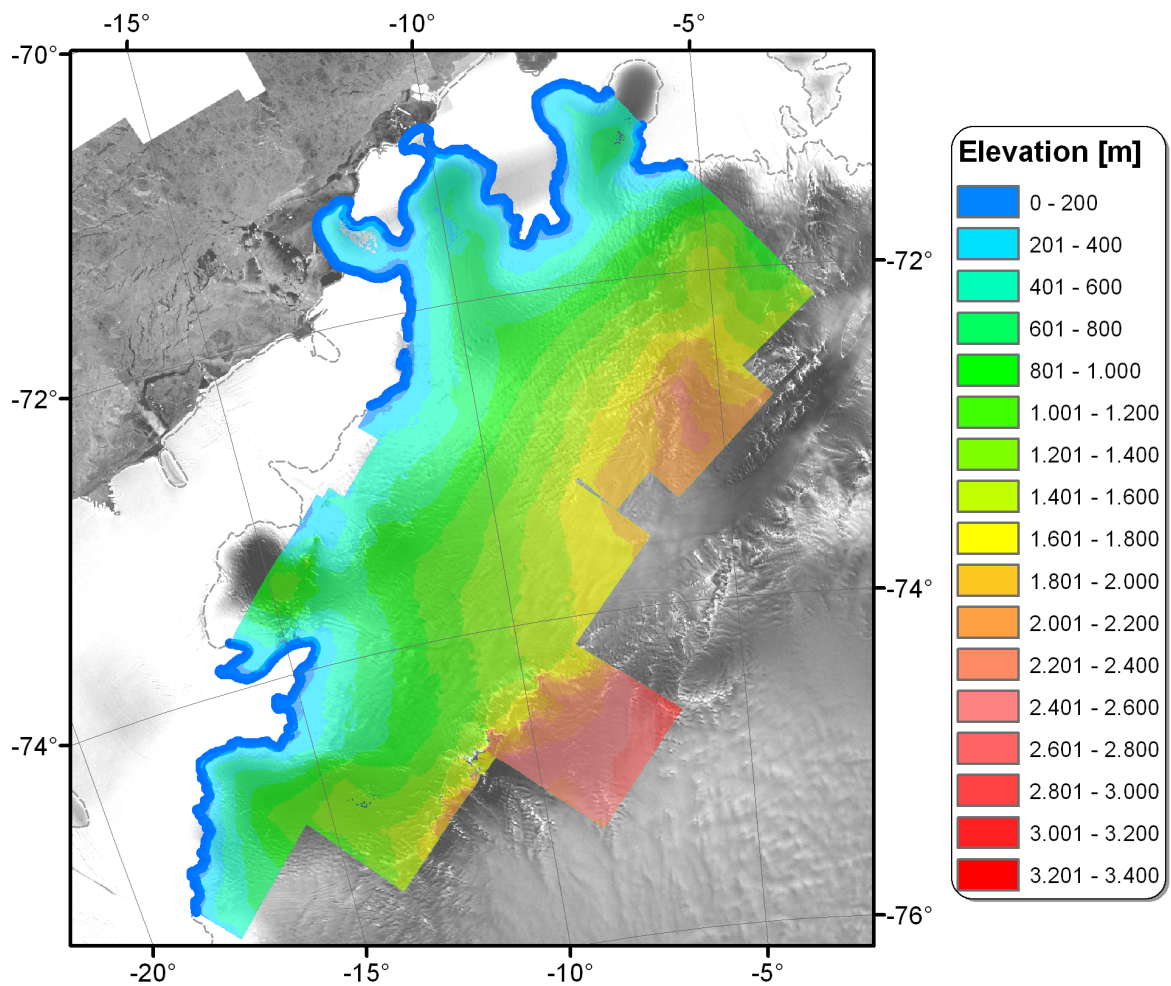# 6 Surface Elevation and Ice Dynamics

Figure 6.1: Overview of the mosaicked DEM with the DInSAR grounding line (blue) and the grounding line from the ADD 4.0 (grey). Th mosaic of the Radarsat Antarctic Mapping mission is seen in the background.

This chapter presents the evaluation of geophysical information that can be extracted from the complete set of processed frames. It includes the comparison of the DEM with external data as well as an internal differencing of overlapping frames. The detected grounding line will be compared to data available from the Antarctic Digital Database. At the end the flowfields will be evaluated and used for considerations on mass balance as well as an estimation of accumulation rate.

6.1 Evaluation of the final DEM

The final DEM is derived by mosaicking the individual georeferenced DEMs from all single frames (Appendix table A.1) . Since the quality of the individual DEMs depends strongly on the respective coherence a weighted mean is chosen to average in overlapping areas. The (i,j) - Pixel of the mosaicked DEM is given by:

$$\text{DEM}_{(i,j)} = \frac{\sum_k^N cc_{(i,j)}^k \text{dem}_{(i,j)}^k}{\sum_k^N cc_{(i,j)}^k} \tag{6.1}$$

With

$$cc_{i,j}^k = \left\{ \begin{array}{cc} cc_{i,j}^k & \text{if} \quad cc_{i,j}^k > 0.6 \\ 0 & \text{otherwise.} \end{array} \right\}$$

This step function is chosen, because with a lower coherence value the DEM deteriorates too much. Mostly the noise level is too high and phase unwrapping errors are likely. The exact value of the threshold is somewhat arbitrary and was set after comparing the deviations of IceSAT profiles and DEM with the corresponding coherence (see 6.4). Sometimes it is still possible to track the grounding line, although the coherence is lower than the threshold. If this is the case the respective DEM is included for the grounding line detection.

Generally there are other parameters as well, which could be incorporated into the fusion process. For example DEMs with a larger differential baseline are usually more reliable, and too small baselines ($< 20m$) should be excluded. This was not done here, since not enough pairs with a sufficient coherence were available to allow for such an exclusion. Another interesting point is to account for systematic errors (as for example imprecise geo referencing) with a special fusion technique mentioned in [MC05]. This might be done at a later point. For now the weighted averaging should suffice. Usually not more than three DEMs ($N = 3$) overlapp at the same time, but over most parts at least two DEMs do overlap and so it is possible to lower the noise level in large areas.

The final DEM covers approximately $1.35 \cdot 10^5$ square kilometers, which would blanket about 40 percent of Germany. Altogether 19 different DEMs (29 frames) are merged. The height model is compared to IceSAT and GPS ground control points where available. Overlapping parts of the various frames are differenced to see deviations. At the
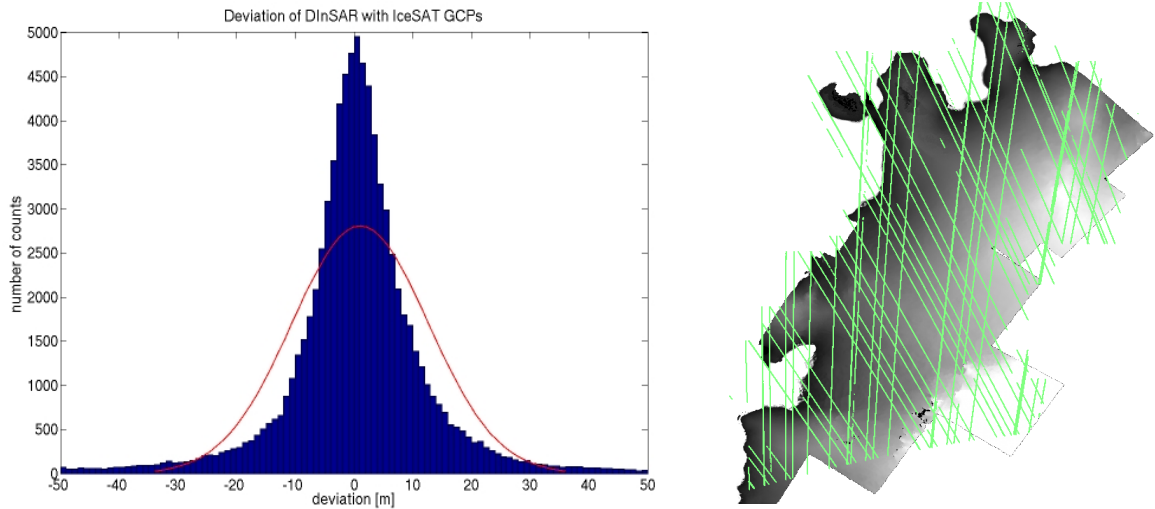
Figure 6.2: Histogram of deviation from IceSAT minus DInSAR (left) and position of IceSAT tracks (right). The red line in the histogram represents a Gauss function

end, a comparison to the existing height models in the regions is performed. Therefore the RAMPv2 model from the Radarsat Antarctic Mapping Project ([HL01]) , the model JLB97 by Bamber and Bindschadler ([JB01]) and the newest GLAS/IceSAT DEM [JD07] are being used.

6.1.1 Comparison with IceSAT

For the comparison, all available IceSAT points were used. These do not include points over regions where the DInSAR model shows low coherence or over shelf ice. The points that were masked because of low coherence are less than one percent of the total amount. The mean deviation $\bar{s}_{Ice}$ from DInSAR height to IceSAT ground contol points is:

$$\bar{s}_{Ice} = (-1.76 \pm 12)m \tag{6.2}$$

The relatively low mean deviation should not be overestimated, since every single frame was adjusted with a third order polynomial to the respective IceSAT profiles within the frame (see section 5.3). The comparison was performed with the DInSAR model sampled to (50x50) m/pixel. In this high spatial resolution the model is noisy, as can be seen in the large standard deviation. Sampling to a larger grid cell size reduces this effect. However, the deviations do not follow the expected standard Gauss function (see figure 6.2). A small amount of ground control points shows larger deviations than expected,
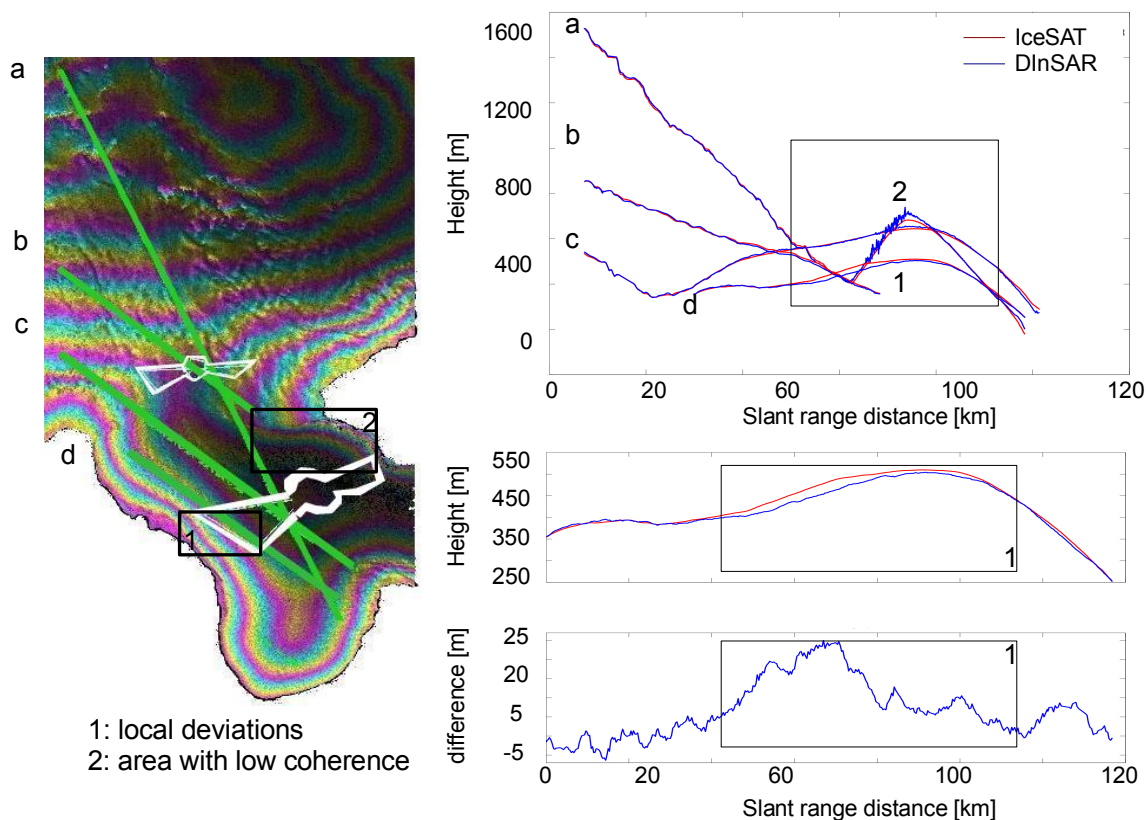
Figure 6.3: Example for low coherence and local deviations from DInSAR model. The green tracks (a,b,c and d) represent available IceSAT profiles, the white lines GPS measurements.

which leads to heavy tails on both sides. A similar effect was observed by Bamber et al. [JB05] during the comparison of JLB97 and RAMPv2 with IceSAT data. There, the negative part of the tail is attributed to the fact that the radar altimeter resolves only sub-kilometer undulations, whereas IceSAT recognizes small scale features like rifts and crevasses. Here, additional effects are observed: Primarily, the extent of the heavy tails depends on the threshold of coherence that is chosen for the comparison. Areas with lower coherence show point-wise large deviations in the positive and negative domain. Secondly, although the DEM was globally fitted to the IceSAT ground control points, one can still observe localized differences as can be seen in figure 6.3.

These localized deviations may be caused by varying penetration depths as already mentioned in section 5.4. In the example of figure 6.3 it is visible that the DInSAR model locally underestimates the actual height given by the ground control points. At first sight, the underestimation could be generally associated with the larger penetration depths of the ERS-radar signal compared to IceSAT's laser altimeter. However, this ef-
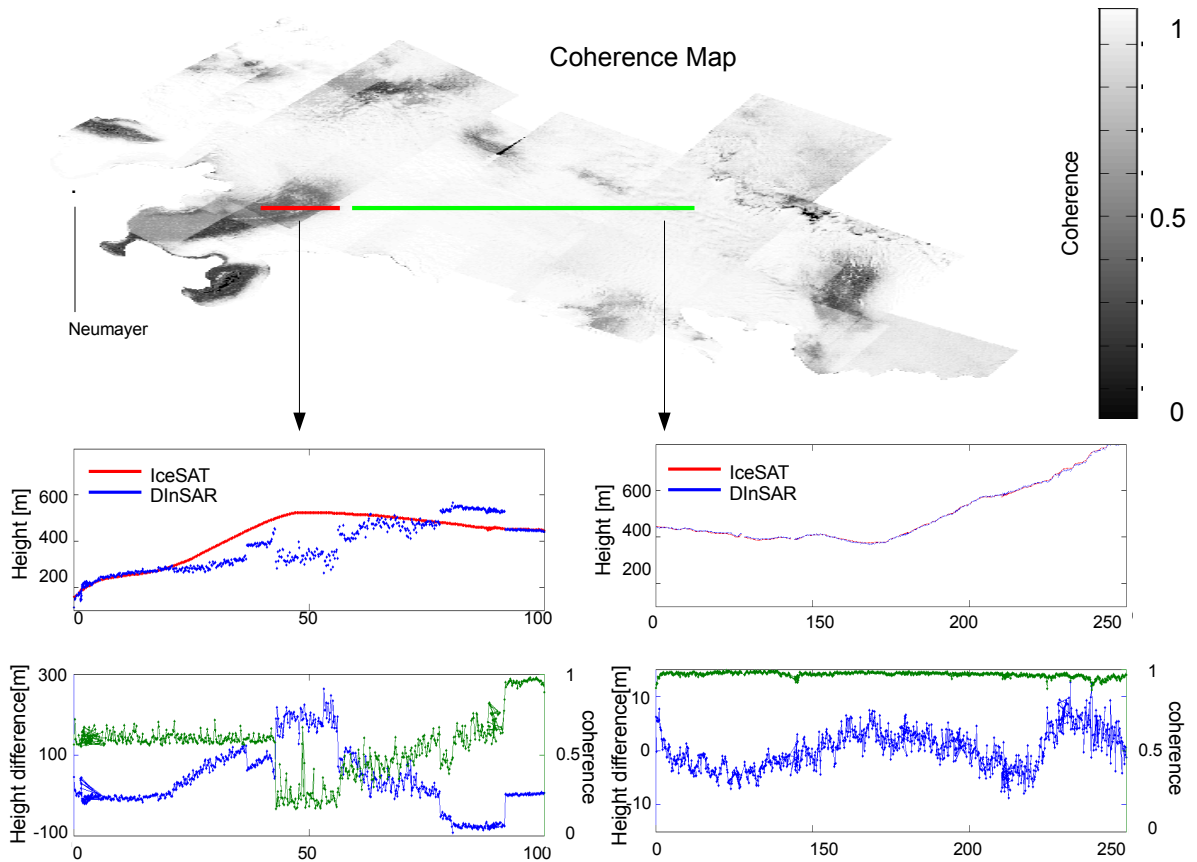
65

Figure 6.4: Overall coherence map with an example profile from IceSAT. The green profile is in areas with good coherence and only small deviations within the general noise level are observed. In areas of low coherence (red profile) the deviations increase extensively, mostly due to errors in phase unwrapping. The two lower plots magnify the deviations, left the area of low coherence, right the area of high coherence.

fect is already corrected by the baseline refinement which globally adjusts the DInSAR model, together with the fit of the DEM to the GCPs. If the radar signal is always reflected from the same layer, no differences should be visible. But if the snow morphology locally changes (e.g. melting), the radar signal is locally reflected from a different layer. In this case the global adjustment could locally lead to over- or understimation, depending on the snow morphology. The relatively low coherence close to the area of local deviations possibly indicates such a local change in snow morphology.

To demonstrate the influence of coherence an example profile, crossing 300 km of the final DEM through all zones of coherence, is chosen in figure 6.4. In areas of good coherence the deviations toward this IceSAT profile are in the order of (-0.05 ± 5.4) m with a grid cell size of (50×50)m. In areas with low coherence (< 0.5) the DEM is
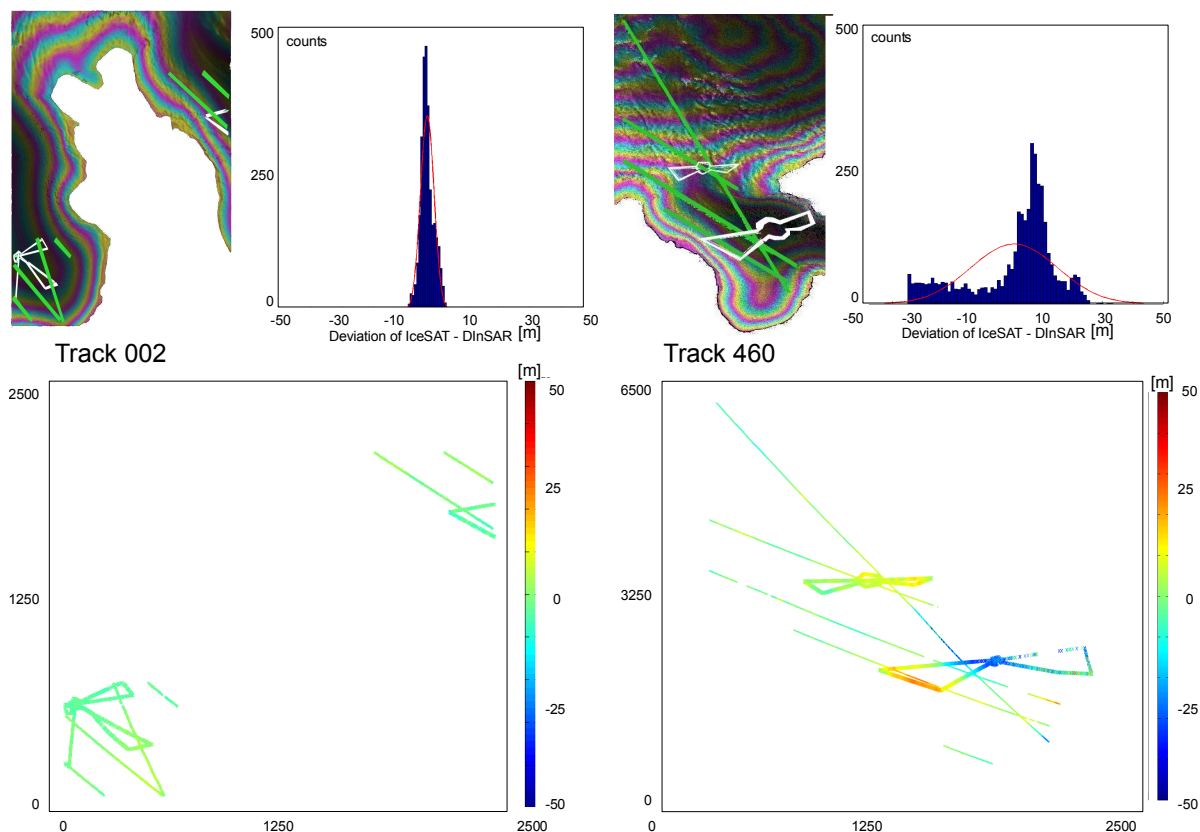
Figure 6.5: Difference of GPS data with DInSAR model. Both tracks overlap but track 002 performs significantly better compared to track 460. The thinner streaks represent the available IceSAT profiles in the area.

basically invalid. Mostly because a too high noise level leads to problems in the phase unwrapping. Fortunately these areas are well documented in the coherence map of figure 6.4, and areas of an appropriate coherence level outbalance those of too low coherence. The dominating role of coherence in the DEM's quality also justifies the weighted averaging from equation 6.1.

6.1.2 Comparison with GPS

The GPS data was collected by C. Wesche and D. Steinhage during a CryoSAT calibration and validation campaign in early 2007. The profiles were recorded in the vicinity of Neumayer. The investigated areas cover mostly the Halfgarryggen and Søråsen, southeast and south-west of the german overwintering station. The accuracy of GPS data is

in the order of cm to dcm. The spacing is originally about 3 m, but it is sampled to the same pixel spacing as the DInSAR model (50x50 m) for the comparison. The GPS data only covers a small part of the complete DInSAR DEM, but the comparison is instructive, since it is an independent data set. It was not used to derive the DInSAR DEM. The region, where GPS data is available, is partially covered by two overlapping tracks (track 460 and track 002). GPS values in areas of low coherence were excluded in both tracks during the comparison. As can be seen in figure 6.5 the results are ambiguous. Track 460 shows a mean deviation $\bar{s}_{gps}$ from:

$$\bar{s}_{gps} = (3.8 \pm 10)m \tag{6.3}$$

whereas track 002 shows a mean deviations $\bar{s}_{gps'}$ of

$$\bar{s}_{gps'} = (-2.8 \pm 2)m \tag{6.4}$$

Again a local change of penetration depths, as already observed during the comparison with IceSAT profiles, might be responsible for the large deviations on track 460. On the right side of figure 6.5 the largest deviations are exhibited condensed and locally. In this area the IceSAT profiles show larger deviations as well. It seems that the quality of track 460 is not as good as track 002's quality if it comes to the DEM generation, but if the differences really relate to a change in penetration depth, interesting conclusions can be drawn for the corresponding snow morphology.
The deviations could also be attributed for example to atmospheric delays or a real change of height, but therefore the deviations almost seem to locally arranged.
Since both frames show a reasonable coherence in the area of interest, the averaged final DEM does not account for the deviations in track 460 except for averaging the differences. So deviations in the same order of magnitude when comparing the final DEM with the GPS profiles can be seen as well. However, the good results of track 002 definitely show the potential of the method.

6.1.3 Comparison of Overlapping Areas

Comparing overlapping areas of different frames but equal tracks can give insight into errors during the processing. This is considered in section 5. If different tracks are compared, the difference cannot be attributed to a single source, but it gives a good impression of the overall accuracy as well. As an example for independent tracks , a relatively large overlapping area of track 407 and track 035 was chosen in figure 6.6. The mean deviation in the overlapping area $\bar{s}_{overlap}$ in this case is given by:

$$\bar{s}_{overlap} = (-0.004 \pm 11)m \tag{6.5}$$

For the most part, no systematic error is observable, and the scattering around zero
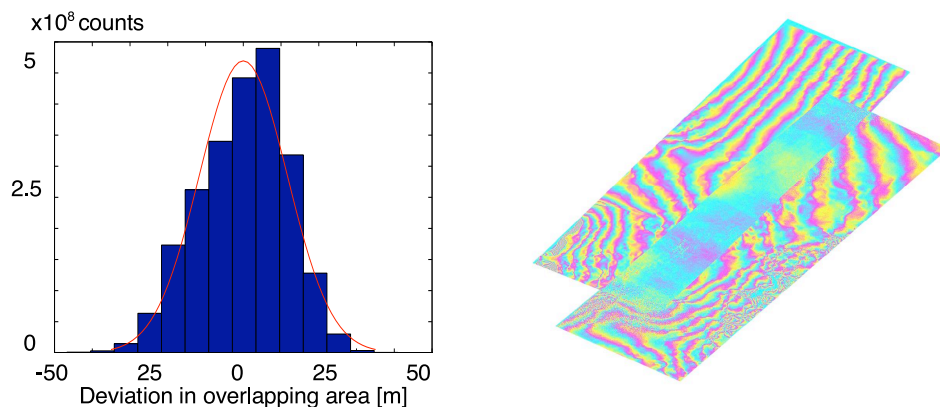
Figure 6.6: Difference of overlapping area from frame track 035 and track 407. The heights are color coded with 100 m per cc.
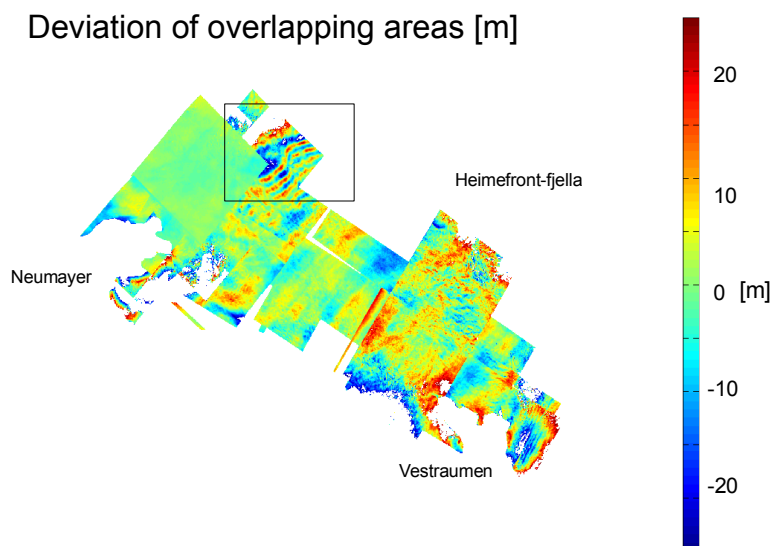
Figure 6.7: Difference map of all overlapping areas. In the most part no systematic differences are visible. The box marks a wavelike structure that could be caused by weather patterns.

resembles the expected gaussian form. In figure 6.7 a map of all overlapping areas is displayed. The major part of the differenced regions shows a random scattering around zero with a variation from ±20 m. This error is in the expected magnitude, considering the average noise level on a 50x50 m grid. The deviations are especially large in frames

with a relatively low coherence (as for example track 017) and in mountainous areas like the Heimefrontfjella. In the latter, errors are in the order of 50 m and were masked out in the overall difference map. However, this part is small and not representative for the complete DInSAR DEM.

A small area (see figure 6.7 in box) shows systematic deviations, which are investigated further in the following seciton.

6.1.4 Atmospheric disturbances

Figure 6.8(a) examines the systematic differences which were observed in the difference map of figure 6.7. These systematic differences have a wavelike form and are in the order of almost 30 meters and so well above the general noise level. It becomes visible when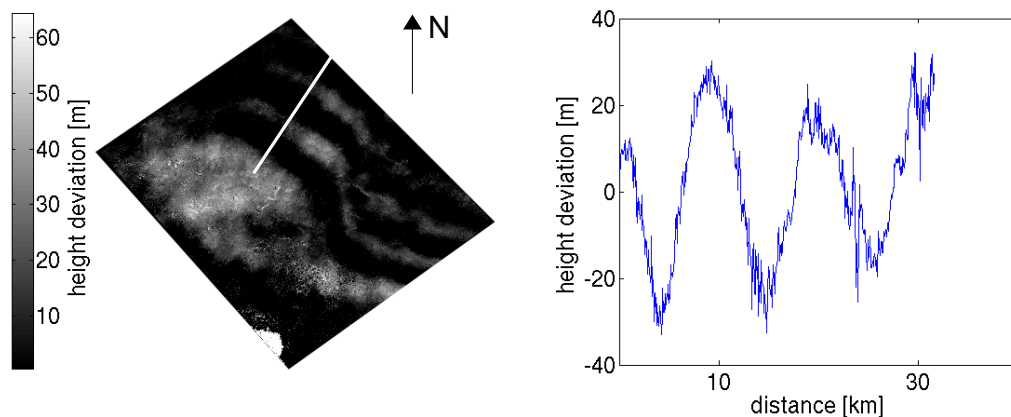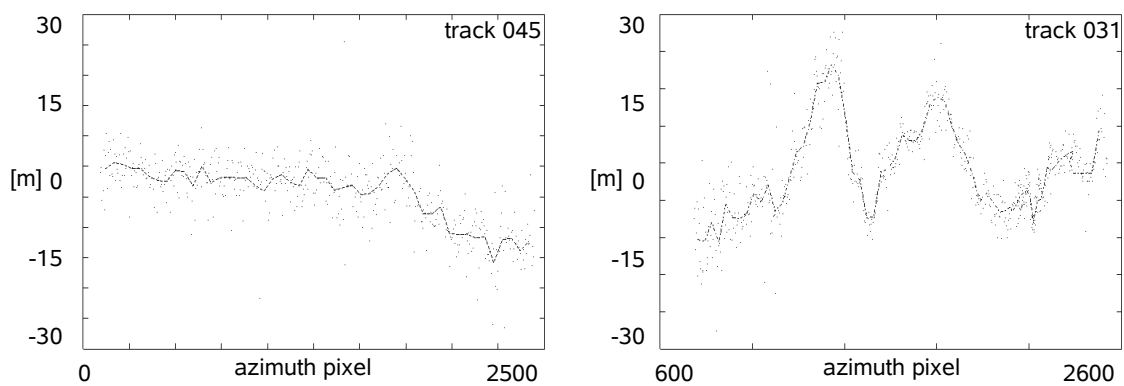 the DEMs of track 031 and track 045 are differenced. The effect can be attributed to track 031 and not to track 045. This is clear if displacement fields are calculated with the corresponding DEMs from the single frames. The wave like pattern only appears in the displacement field of track 031. Both frames have a gradient from north to south and are almost constant from east to west. So the expected main flow direction, apart from the south east corner, is from the bottom to the top and not across the frame. The flow field of track 031 looks very much like the difference map in figure 6.8(a), except for a different scale, and does not show the expected flow direction. On the other hand, the flow field of track 045 looks alright. Figure 6.8(b) fortifies that impression. There, deviations to a common IceSAT profile are displayed and in track 031 the same pattern appears again.

The respective dates of the two frames are March 1994 (track 031) and March 1997 (track 045). It seems unlikely, that an actual change of topography (which took place within three years) is responsible for that kind of a deviation. It seems more likely, that this is a good example for an atmospheric effect. The wavelike pattern could be atmospheric waves in the troposphere which is known for its possible impact on SAR Interferometry (see for example [JV03]). Generally the atmosphere has two effects: the path or the signal can be bend and/or it can induce a delay of the signal. The latter might lead to the observed wavelike pattern.

(a) Systematic differences of track 031 and track 045 in frame 5661(right). The profile on the right side (marked with white line on left) is taken across the wave like structure. The scale and form of the differences hint to atmospheric waves. North is up.

(b) When compared to a common IceSAT profile, Only track 031(right) shows the wavelike deviations as well.

Figure 6.8: Possible influences of atmospheric effects, observed which differencing the DEMs of track 031 and track 045.
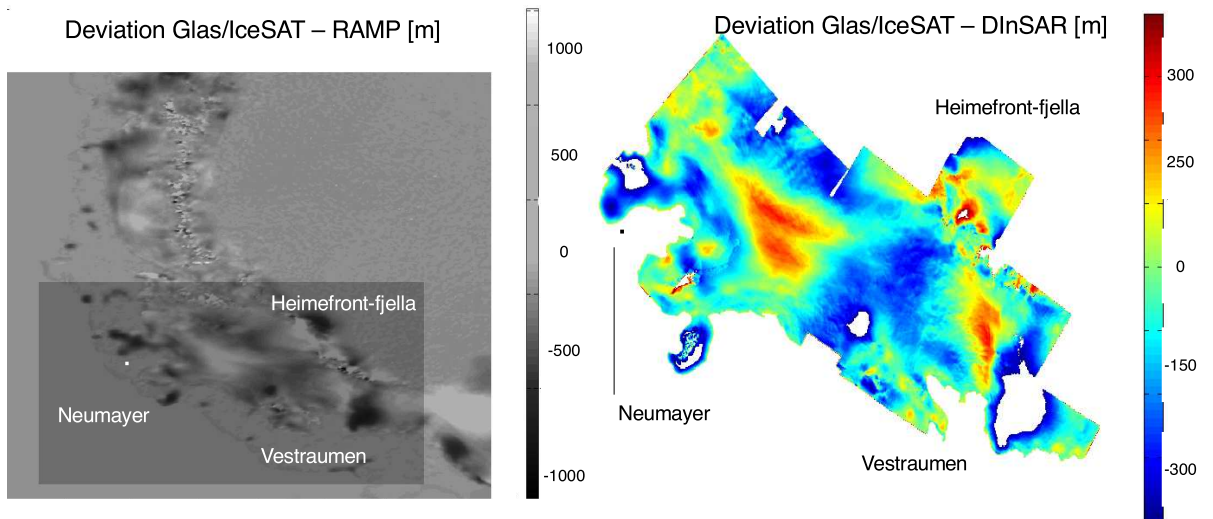
Figure 6.9: left-Towards the inland GLAS/IceSAT and RAMPv2 show agreement in the order of 10 m. On coastal areas the deviation reaches sometimes more than 200 m. **right**- Comparable difference between RAMPv2 and the DInSAR DEM.

6.1.5 Comparison with other DEMs

Existing height models in the region are the RAMPv2 [HL01], JBL97 [JB01] and the GLAS/IceSAT [JD07] model. RAMPv2 and JBL97 rely mostly on the radar altimeter onboard the ERS1. JBL97 uses this data to derive a DEM with 5 km postings. In areas of steep relief it was combined with terrestrially derived data. RAMPv2 includes the radar altimeter but also various other data sources as for example GPS measurements, airborne radar or data from the Antarctica Digital Database (ADD). In its highest resolution it offers a pixels spacing of (200x200)m. Both models were calculated with a different set of algorithms and substantial differences, even in areas were solely the radar altimeter was available, are observed.

The GLAS/IceSAT model was compiled out of IceSAT's laser altimeter in 2007. Whereas the laser altimeter is advantageous in terms of penetration depths (~ 0 meters), it is more vulnerable by for example cloud coverage or foggy conditions. Other error sources include track mislocations and artifacts of gridding algorithms. The quality of the models decreases with increasing track spacing towards the equator. The model comprises the complete Antarctic continent with a pixel spacing of 500 m.

At first a point-wise comparison of the JBL97 with the DInSAR DEM is performed (figure 6.10,right). The mean deviaton $\bar{s}_{JBL97}$ is:

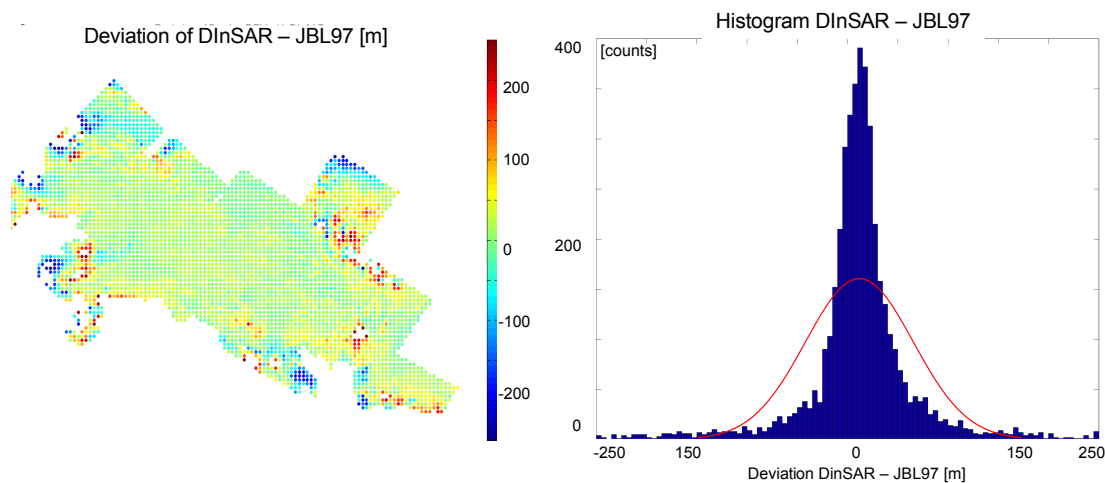$$\bar{s}_{JBL97} = (11.7 \pm 53.6)m \tag{6.6}$$

72

Figure 6.10: left-Difference of the JBL97 and the DInSAR model at a 5 km pixelspacing **right:** Histogram of deviation with mean value at +11.7 meters.

The error distribution is non gaussian, for the same reasons as explained during the comparisons with IceSAT profiles. Noticeable is the large positive displacement of the mean value. This can be attributed to the penetration depth of the radar altimeter in JBL97 which was not corrected with surface near GCPs as the DInSAR model was. Thus, a positive displacement of the mean value is to be expected. A spatial comparison (figure 6.6,left) reveals that deviations are small in planar areas and increase with slope towards the coast. These slope induced errors occur when the altimeter receives an echo from an off nadir point. However, from an interferometric point of view the crude resolution is the biggest problem of the JBL97. Therefore the comparison will now focus on models with a higher spatial resolution.

To get an idea of the deviation from higher resolved models in the area of interest, the GLAS/IceSAT model is subtracted from the RAMPv2. In figure 6.9 (left) it becomes evident that these two models disagree especially in coastal areas, since coastal features can be seen in the differenced image. The disagreement on the Halfgarryggen and Søråsen close to Neumayer is in the order of more than 200 m. Inwards the deviations are significantly smaller. This can be expected, as the track spacing for the GLAS/Ice-SAT model decreases and at the same time RAMPv2 is less affected by slope induced errors of ERS1's radar altimeter and needs no auxiliary data.

Compared to the DInSAR DEM, RAMPv2 shows equally large variances on coastal areas (figure 6.9, right). It seems that the RAMPv2 model is adequate inbound, but shows quite significant deviations on the rims. This is also confirmed by a comparison with an airborne radar altimeter as well as ground base GPS measurements. Now the question arises, how the GLAS/IceSAT model relates to the new DInSAR DEM.

A comparison from the GLAS/IceSAT model with the DInSAR model can be seen in the
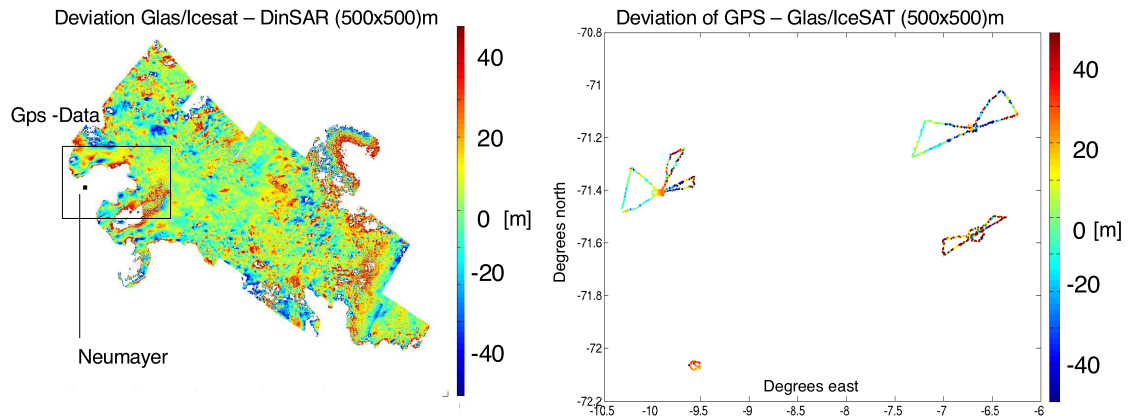
Figure 6.11: left - Difference of the Glas/IceSAT model and the DInSAR DEM. Deviations are especially large close to the coast around the Vestraumen and in mountainous areas as the Heimfront-fjella. **right** - Comparison with GPS data at a (500x500)m cell size. Some GPS measurements are not close to available IceSAT tracks, and interpolation errors in these regions are in the order of 30 meters, pointwise up to 40 m. In areas close to IceSAT tracks the deviations decrease.

map of figure 6.11 (left). The major part of differences is in the order of ±20m. Again, in mountainous are larger and masked out, but this is not representative for the complete area. Significant deviations on Halfvarryggen or Søråsen, as seen during the comparison with RAMPv2, are not observed. The GLAS/IceSAT model is also compared with the same GPS measurements as the DInSAR model in figure 6.5.

Masking because of low coherence is obviously not necessary and thus all GPS profiles can be used for the comparison and are sampled to a (500x500)m grid. Figure 6.11 displays the results: In areas far away from available IceSAT tracks the interpolation error reaches up to 30 meters. Especially the most southerly set of GPS measurements fall in such a 'gap' between IceSAT profile. In regions where more tracks were available the deviations are significantly smaller.

As a summary of all the comparisons it can be said that the DInSAR approach, in combination with IceSAT ground control points, offers the most precise DEM in highest resolution. As indicators of how errors are spatially distributed serves the difference map of overlapping areas from figure 6.7 as well as the coherence map from figure 6.4. Especially frames from the ice phase, with a three day repeat pass period show lower coherence and thus an increased noise level.
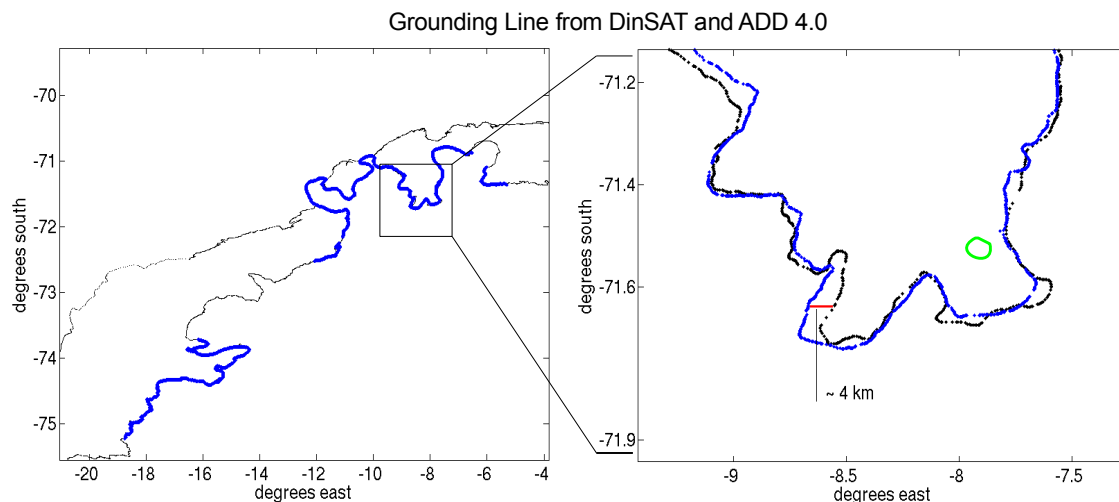
6.2 Grounding Line Detection

Figure 6.12: Grounding line from DInSAR (blue) and the Antarctic Digital Database (ADD) version 4.0. As can bee seen in the more detailed representation on the right, deviations reach up to 4 km. ADD does not include all islands off shore, whereas the DInSAR grounding line reveals all touch down points of the shelf ice clearly (green).

The grounding line is the boarder, where ice that is attached to solid ground passes over to ice which floats on the ocean. In order to model the dynamics of the marine ice sheets, a precise knowledge of the grounding line serves as an important input factor. An advance or retreat of the grounding line might indicate changes in the local flowfields and thus in the local mass balance as well.

Approximately $1.35 \cdot 10^4$ km of grounding line could be derived from the available data. The grounding line was extracted visually, by following the shear zones between shelf ice and grounded ice which are clearly visible in every interferogram that boarders the coastline. The spatial extent of the shear zone varies in average between 1 - 4 km. For defining the grounding line, the inner boundary was chosen in order to exclude all height artifacts because of the residual tidal displacement. To choose the inner boundary is also appropriate, because the shear zone can mostly be considered to be above water. Above land, the ice is frozen to the ground and only very little vertical displacement is possible.

The Antarctic Digital Database (ADD) contains a variety of geophysical information derived from different sources. It is compiled by the Scientific Committee on Antarctic Research (SCAR) and mostly managed by the British Antarctic Survey. The grounding line catalogued in the ADD version 4.0 relies mainly on the interpretation of optical images from the Landsat satellite and it covers the complete coastline of the continent. Figure 6.12 illustrates the comparison of the two grounding lines. As observed in [TY99]

as well, the DinSAR grounding line offers a more detailed model of the coastline. It reveals also small islands buried below the iceshelf that are not catalogued in the ADD. Deviations between the two models reach up to 5 km.

6.3 Evaluation of Flowfields

Each frame that is covered by the mosaicked DEM offers a flow field. So, not only all frames from table A.1, but also non-differential frames as in table A.3 can be used. In the latter, the mosaicked DEM serves as external DEM for a two pass approach. Each differential frame offers two flowfields (one for the master and one for the slave) which basically overlap fully. In that case, the flowfield with the smaller baseline as well as the higher coherence should be chosen.

For the 3D-flowfield model, overlapping frames of ascending and descending orbits have to be found in order to combine them as explained in section 4.5. This was possible in some areas, particularly for the catchment basins of the Ekstrømisen and the Vest-straumen. The mosaicking was done in the same way as the merging of the DEMs. An overview of these areas is seen in figure 6.13. Together with the ice thickness model from D. Steinhage, it is possible to use the motion maps for instance for mass balance and accumulation considerations, which will be done in the following.

The daily flux f_d through an area below a profile on the surface (assumed to be in x direction) can be calculated by integrating the velocity field $\vec{v}$ together with the ice thickness map $I(\vec{x})$ along the profile:

$$f_d = \int dz \int dx \quad I(x) \cdot \vec{v}(x,z) \cdot \vec{n} \approx 0.95 \sum_{i=1}^{n} I(\vec{x}_i) \vec{v}(\vec{x}_i) \vec{n} \Delta x \qquad [\frac{m^3}{d}] \tag{6.7}$$

thereby the vector $\vec{n}$ depicts the surface normal. Two approximations are being made: The first one due to a discrete sampling, the second one because only the velocities on the surface are known. For a first approximation a step function in z direction is assumed, which models 5 percent of the ice frozen to the ground whereas the rest moves with a constant velocity which is given by the velocity on the surface. The annual massflux m_f can be extrapolated from the daily flux by assuming a constant density ρ for ice (about $990 \frac{kg}{m^3}$) and so:

$$m_f = 365 \cdot \rho \cdot m_d \tag{6.8}$$

The main iceflux in the Ekstrøm region is dominated by three inlet glaciers from which two are covered by the motion map. For the third glacier only one velocity component is known and the mass flux must be calculated with further approximations. For the two glaciers that are fully resolved, profiles can be taken right in front of the grounding line and aligned perpendicular to the main flow direction (red profiles in figure 6.13,
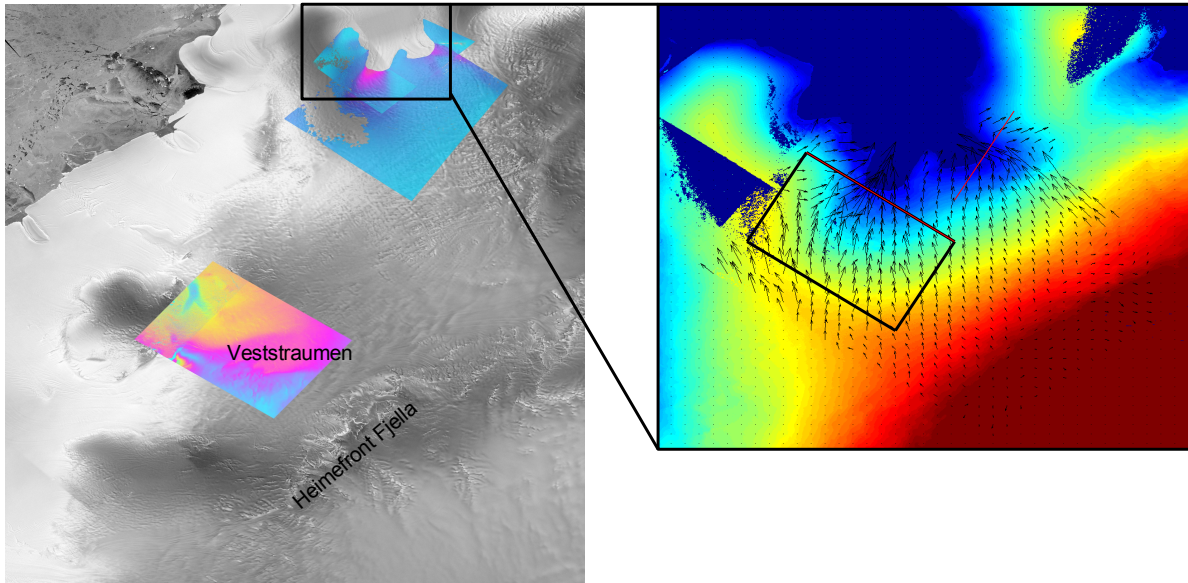
Figure 6.13: left: Overview of 3D-velocity fields. Mostly the drainage areas of the Ekstrømisen as well as the Veststraumen are covered. The colors represent 1 m per color cycle, 1 m/d is the peak velocity at the bottom of the Veststraumen. **right:** Zoom to the Ekstømisen with parts of the velocity field. Color coded is the height model. The black box has an area of approximately 840 km² and marks the area for accumulation estimation.

right). The flow fields converge towards these profiles and a significant amount of ice from higher elevated areas must pass through them. So a good amount of the total annual massflux into the Ekstrømisen can be estimated:

$$m_{f,total} = m_{f,1} + m_{f,2} = (1,26 + 2.19) \cdot 10^3 \frac{GT}{a} = 3.45 \cdot 10^3 \frac{GT}{a} \qquad (6.9)$$

How exact are these results? As mentioned before, from a DInSAR point of view, this depends on the one hand on the quality of the DEM in the region and on the other hand on the sensitivity towards motion, given by the size of the differential baselines. If the quality of the DEM is good, this cancels several effects like change in penetration depths or atmospheric influences. If they were present, the DEM would not be good. As a consequence, the quality of the DEM is a direct measure of the quality of the displacement maps. A change of flow velocity could be expected, since the profile is taken close to the grounding line and tides could possibly influence the glacier dynamic. However, in that case a rather steep, artificial hill or valley in the DEM should be visible. All this is not the case here. Profiles of the DEM are smooth and the coherence relatively high so that the average height error can be estimated to be in the order of seven meters. That leads to a negligible error in the flow field (see section 4.5). Errors in the velocity field are then mostly introduced through an imprecise baseline model, which is needed
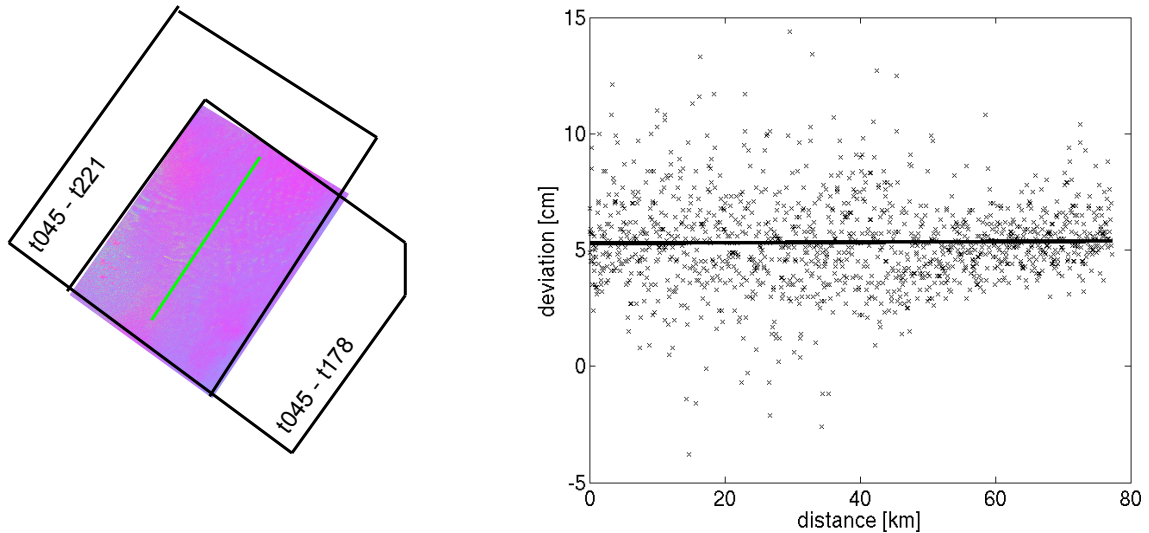
Figure 6.14: Overlapping parts of 3d displacement fields are differenced to see deviations. In this example combinations with track 045 (f5661) were taken. The ascending counterparts were track 221 (f5103-5121) and track 178 (f5103).

for a topographical interferogram generation in the flow field derivation. So if the flux is calculated, the accuracy of the result depends mostly on the accuracy of the baseline as well as the accuracy of the ice thickness model.

However, for the yearly mass balance this is different. The assumption of a constant ice density as well as the approximation of the constant vertical velocity profile leads inevitably to higher error margins. Also it is not clear how the glacier velocities vary over the different seasons of a year. This can at least partly be checked by looking at the deviations from velocity fields of different dates. This is done in figure 6.14. This example shows differences with 3D combinations of track 045 with its ascending counterparts of track 221 and track 178.

The color coded difference map of figure 6.14 reveals a constant offset of about 5 cm/d, but changes in the flow directions are not visible. The constant offset could be introduced through the processing chain or through an actual change of flow velocity. An actual change in flow velocity of 5 cm a day should reveal deviations in the DInSAR pair of track 045 with a temporal separation of 1 year. However, if this offset is constant over the complete frame it will not be visible in the DEM after tie-points are being used. Only local changes, can be clearly determined in terms of a local deviation in the DEM. A hint that the deviation is artificially introduced through the processing is, that the other available difference maps in the region show a constant offset as well. They all range from 3-6 cm and for now it should suffice, that the norm of the velocity field is accurate to the order of 3-6 cm and changes in the flow direction are not visible. Since

it is not clear whether the error is due to the processing or not, it must be considered in the daily balance as well.

If an absolute error 5 cm of the velocity field is assumed, it depends on the absolute glacier velocities on how this error propagates. For the medium fast Ekstrøm inlet glacier it leads to a yearly uncertainty of about 30 percent.

Another problem is to derive mass flux estimates for areas where no ascending and descending orbit can be found for a combination. In this case, only one component of the velocity field is known and a reasonable approach needs to be developed. One possibility is the combination with a theoretical ice flow model. Another option is a simplified look-angle dependent estimate on how much displacement is lost. This is necessary in order to evaluate the complete mass flux in the area which is covered by the DEM, but this is not done here. Also the 3D-displacement field close to the Veststraumen is not evaluated further at the moment. Later on it is planned to compare results with M. Bäßler at the "Institut für Planetare Geodäsie" from the Technical University in Dresden, who works in the same area.

6.3.1 Estimation of Accumulation Rate

The goal of this section is to estimate the accumulation rate by calculating incoming and outgoing mass flux of a certain area. This area is marked in 6.13 with the black box on the right. It is chosen because a 3D displacement field is available and at the same time a higher resolved ice thickness model exists. This is due to the dense track spacing of the RES - System in the closer neighborhood of the Neumeyer station (see section 2). It is reasonable to sample it to a (500x500) m grid. In this case it was even sampled to a (50 x 50) m grid (in order to match the grid of the flow field). Figure 6.15 sketches the theory of the approach: Incoming and outgoing fluxes of a closed box are calculated to determine the overall flux:

$$m_{f,total} = m_{f,out-y} - m_{f,in-y} + m_{f,out-x} - m_{f,in-x} \qquad (6.10)$$

The signs are chosen to match the actual direction of the main flowfield. If no sources or sinks exist, the overall mass balance should be zero. A negative mass balance (more outgoing than incoming flux) is caused by a source. This source is connected with accumulation within the box. Correspondingly a positive mass balance (more incoming than outgoing) indicates sublimation or ablation. Note that in that approach the actual value of the velocity is of lesser importance than the relative values between the incoming and outgoing fluxes. If the velocity field is shifted with a constant factor (as indicated in figure 6.14), the difference of incoming and outgoing flux is not affected. Only changes in the velocity direction and amount within the box really influence this model. However, such a change was not observed yet.
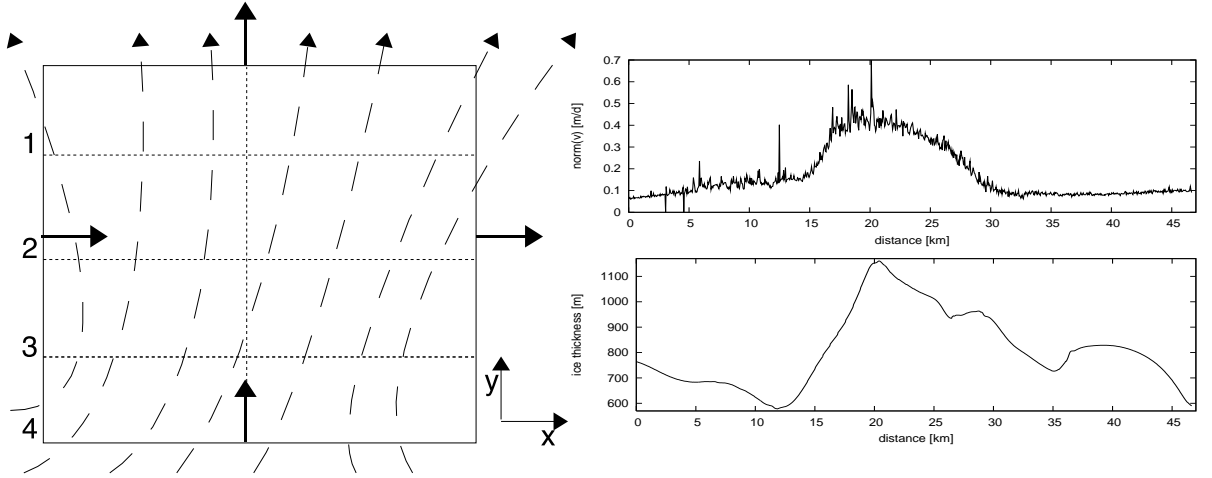
Figure 6.15: Box model that is assumed to estimate the accumulation rate. The dashed vectors represent a sample velocity field, the bold vectors mark the orientation of the surface normal. On the right, a sample profile from the outgoing velocity field of box 1 is displayed together with the corresponding ice thickness.

The box comprises an area A of 840 km^2 and is subdivided into four sub-boxes. The overall mass flux of the complete box results in:

$$m_{f,res} = (2.128 - 2.214 - 0.077 - 0.047)\frac{km^3}{a} = -0.211\frac{km^3}{a} \tag{6.11}$$

and is negative. If that is to be explained with a constant accumulation rate $\dot{a}$ over the area A, the deviation from zero ($m_{f,res}$) can be modeled by:

$$\dot{a} = \rho\frac{m_{f,res}}{A} = 990\frac{kg}{m^3}\frac{2.11 \cdot 10^8\frac{m^3}{a}}{840 \cdot 10^6 m^2} = 248\frac{kg}{am^2} \tag{6.12}$$

To see if this is a reasonable accumulation rate, a comparison with external data is necessary. An accumulation map for Dronning Maud Land was compiled by Rotschky and others (AWI) in [RG07]. It was mostly interpolated from point data, which was retrieved from firn and ice core drillings in combination with snowpits. The accumulation rate in the area of interest is believed to be in between (250 - 300) kg(am^2)$^{-1}$ which means that the estimated accumulation rate from equation 6.12 is in the right order of magnitude. Figure 6.16 shows the results for the individual sub-boxes from the scheme in figure 6.15, together with the estimated solution for a constant accumulation rate of 250 kg(am^2)$^{-1}$. It becomes evident, that the gain of mass is not constantly distributed over the 4 sub-boxes. Especially box number three actually shows a positive mass balance. There is different explanations. A positive mass balance could be caused by sublimation of snow. On the other hand, also the vertical velocity profile could be altered in that
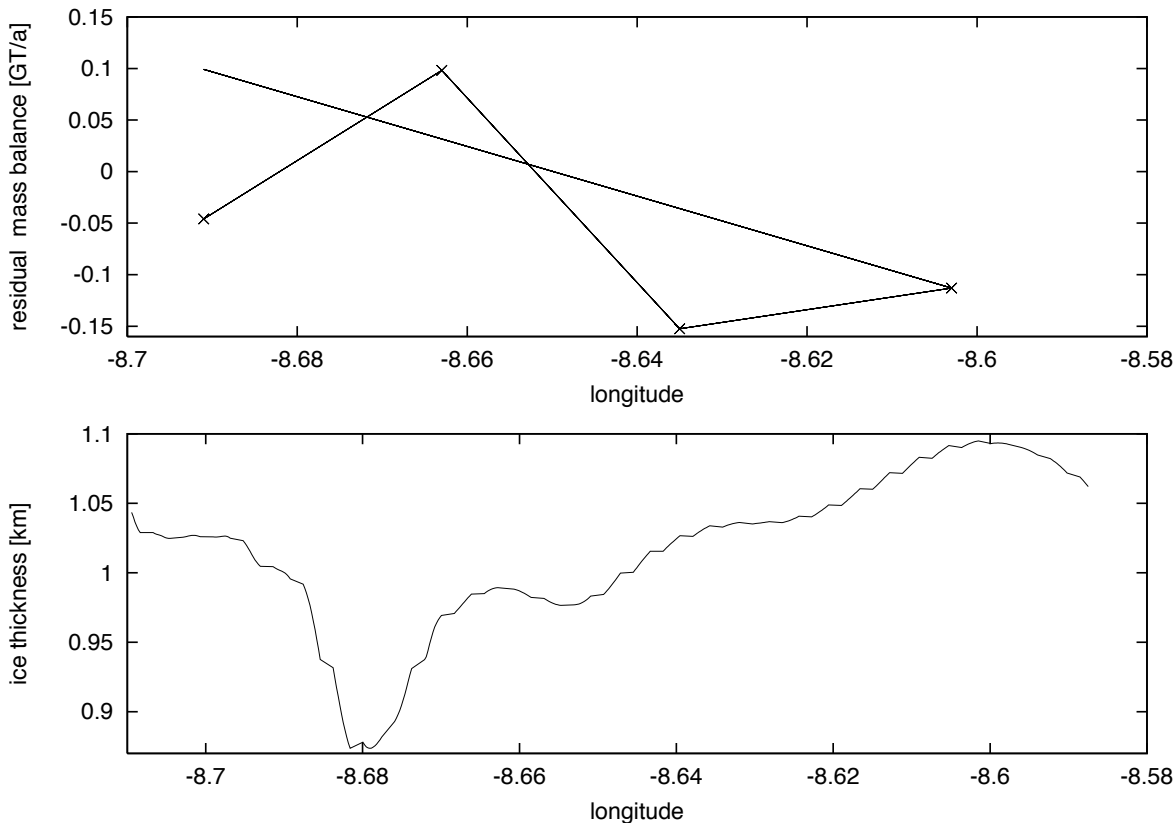
Figure 6.16: top: Overall mass balance for the different sub-boxes. The straight line represents the expected result for a constant accumulation. **bottom:** Ice thickness profile along the main flow direction.

area. In the bottom part of figure 6.16 is the corresponding ice-thickness displayed, a profile that was taken along the main flow velocity (dotted line in the middle of box in figure 6.15). Between the fourth and the third box the ice thickness indicates a bumb in the bedrock topography. It is unlikely, that the velocity profile remains constant while flowing over such an obstacle.

So the model offers the possibilty to discuss two parameters, first on a larger scale the accumulation rates, and second on a smaller scale the variance of the vertical velocity profile. In combination with the accumulation map of [RG07] it would be possible to focus the entire discussion on adjusting the vertical velocity profile. This might be a task for the future.

For now it should be retained, that through a DInSAR approach it is possible to derive accumulation maps as long as the bedrock topography is sufficiently smooth. If accumulation is known in detail, the vertical velocity profile can be adjusted vice versa.

7 Summary and future prospects

During this study a DEM was compiled out of 9 tracks (with 29 different frames) of the ERS satellites. Fully three dimensional velocity fields could be derived for the catchment area of the Ekstømisen as well as partly for the Vestsraumen. In terms of the accuracy evaluation it became evident that between internal and external error sources, can be distinguished.

Internal effects emerge during the processing and are believed to be mainly due to an imprecise estimation of the Doppler Centroid and deviations in the baseline model. In the first part of the study, it could be shown that minimal residual phase patterns which remain after the double differencing, can be held responsible for a systematic tilt of the DEM in the scope of 0 -10 m. This tilt usually increases from near range to far range. It explains the observed discontinuities when appending different SLCs of the same track, and serves a good indicator for the processing accuracy. It also explains the systematic part of deviations, which are observed during the comparison with available IceSAT profiles.

External parameters are given by local changes of the penetration depths or by an actual change of the local height which was measured by the IceSAT profiles from 2003 and the InSAR data from 1994-1996. These deviations are usually distributed in a 10-20 km interval and reach up to 20 m. On the other hand, atmospheric disturbances operate on a larger scale in terms of deviation as well as spatial distribution. This was observed in a smaller subset of data, which exhibited wave like patterns that could be due to fluctuations in the ionosphere or due to tropospheric delays. A change of flow velocity, which violates the used DinSAR approach, was not directly observed and the DEM seems as trustworthy in areas of high displacement as it does in areas with low displacement. The decisive factor of the DEM's quality is governed by the corresponding coherence. In areas of good coherence the error on a (50x50) m grid is around ± 7 m, in areas of low coherence the error can be significantly larger due to a high noise level and errors in the phase unwrapping. These areas are fortunately well mapped and play only a minor role in the mosaicked DEM. During the evaluation it was shown that the here derived DEM is probably the best DEM currently available for this region.

The tracing back of internal errors to essentially two parameters, the Doppler Centroid and the baseline, opens the possibility of an iterative refinement. This would be preferable to fitting DEM to IceSAT GCPs or future CryoSAT-2 data. In other studies these deviations, which sometimes stretch over the complete frame, are also considered to be

local ([BS05]) and attributed to varying penetration depths. However, here it seems as if they are mostly due to the raw data processing. This leads to the new thought of especially adapting the raw data processing to frames in Antarctica. But this is a sophisticated topic and it is not clear if this is feasible.

As a side effect, parts of the grounding line in the area of interest could be extracted and compared to available information in the Antarctic Digital Database (ADD). The InSAR derived grounding line reveals a more sophisticated shape, which also exhibits off shore islands that were not mapped in the ADD. The grounding line dynamic is a good factor for the modeling of tides. The lifting and lowering of the ice shelf must also influence the velocity fields of glaciers close to the grounding line. It is unclear how far this effect propagates land inwards, but a closer examination might reveal interesting effects.

The flowfields picture a high resolution image of glacier dynamics. The areal coverage is thereby restricted by fewer available combinations of ascending and descending orbits. Together with an external ice thickness model, it is possible to derive the overall mass flux of the respective catchment areas. With the help of a box model, it was possible to estimate accumulation rates and the results are in good agreement with other accumulation estimates in that area. To estimate accumulation through DInSAR was never done before. This could be a promising approach in a more detailed project on accumulation. Vice versa it might be possible to refine the assumption of a constant horizontal velocity with depth, if a precise ice thickness model is used in combination with an external accumulation map.

Generally it became evident that the relatively old ERS-data still contains valuable information, especially in combination with the newer IceSAT data. A potential comparison of the DEM with CryoSAT-2 measurements is certainly interesting, and if needed a spatial extension of the DEM and the corresponding velocity fields is possible.

A Appendix

A. Data for DEM and Flowfields

track	frame	date	mi.	data	$\mathbf{B}_\perp[m]$	$\bar{\mathbf{c}}$	$\bar{\mathbf{s}}[m]$	$\sigma[m]$
002	5679 (1)	15/16 01-19/20 02 1996	t	slc	227.1	0.85	0.41	6.0
002	5697 (1)	15/16 01-19/20 02 1996	t	slc	236	0.82	-0.39	17.1
017	5607-5643 (3)	14/17/20 03 1994	i	r	26.5	0.71	-0.35	39.7
031	5661 (1)	06/09/12 03 1994	i	m	80.7	0.89	-0.00	14.3
031	5679 (1)	06/09/12 03 1994	i	m	80.7	0.59	-0.31	24.1
031	5697 (1)	06/09/12 03 1994	i	m	81.0	0.15	0.04	16.7
035	5157-5193 (3)	12/15/18 03 1994	i	r	100.5	0.74	- 0.04	14.8
045	5661 (1)	22/23 03-13/14 03 96/97	t	m	193.4	0.58	- 0.00	6.7
045	5679 (1)	22/23 03-13/14 03 96/97	t	m	193.8	0.58	- 0.20	17.4
045	5697 (*)	22/23 03-13/14 03 96/97	t	m	193.4	0.74	- 12.7	53.9
221	5103-5121 (2)	05/06 03-09/10 04 1996	t	r	234.1	0.78	- 0.00	3.9
221	5139 [cut]	05/06 03-09/10 04 1996	t	r	232.6	0.89	- 0.00	15.0
221	5157-5175 (2)	17/18 10-09/10 04 95/96	t	r	86.3	0.87	- 0.35	16.6
407	5139-5175 (3)	30/31 10-18/19 03 95/96	t	r	235	0.87	- 0.00	2.4
450	5139 (1)	02/03 11-23/24 03 95/96	t	m	67.0	0.78	- 0.28	8.4
450	5156 (1)	02/03 11-23/24 03 95/96	t	m	66.7	0.82	- 0.00	8.1
450	5175 (1)	30/31 10-18/19 03 95/96	t	m	68.2	0.71	- 0.40	18.6
450	5193 (1)	30/31 10-18/19 03 95/96	t	m	66.2	0.64	- 0.00	10.8
460	5679-5715 (3)	16/17 02-22/23 03 1996	t	r	159.6	0.79	- 0.00	6.6

Table A.1: Table of individually derived height models. The following abbreviations are being used: mission ([i]ce [t]andem); data: [r]aw, [m]ixed, esa-[slc]; $[B_\perp]$: absolute value of perpendicular Baseline at start of frame; $[\bar{c}]$: mean coherence value; $[\bar{s}]$: mean deviation to IceSAT profiles; $[\sigma]$: standard deviation to IceSAT profiles. The mean coherence is calculated of the coherence map after differencing.*Track 045, frame 5697 is only used for detection of the grounding line because of too low coherence otherwise.

track	frame	date	mi.	data	$\mathbf{B}_\perp[m]$	$\bar{c}$
178	5103 (1)	06/07 04 1996	t	slc	61.1	- (*)
178	5121 (1)	06/07 04 1996	t	slc	59.3	0.79

Table A.2: Table of interferograms which were additionally processed for flowfield generation. The same abbreviations are used as in the table above. (*) has large parts of missing lines.

track	frame	date	track	frame	date	region
002	5679 (1)	01 1996	221	5103-5121 (2)	03 1996	Ekstrømisen
031	5679 (1)	03 1994	221	5103-5121 (2)	03 1996	Ekstrømisen
045	5103 (1)	04 1996	178	5103 (1)	04 1996	Ekstrømisen
045	5121 (1)	04 1996	221	5103-5121 (2)	03 1996	Ekstrømisen
017	5625 (1)	03 1994	035	5157-5193 (3)	03 1994	Veststraumen
017	5625 (1)	03 1994	407	5139-5175 (3)	03 1995	Veststraumen
017	5625 (1)	03 1994	450	5175 (1)	03 1995	Veststraumen
017	5625 (1)	03 1994	221	5157 - 5175 (2)	03 1996	Veststraumen

Table A.3: Input 1D displacement maps for the 3D-flow field generation. Left are descending and right the ascending orbits.

B. Scene center transformation for DC(r)

Assuming that the DC is given for a certain scene center with the polynomial:

$$DC(x) = ax^2 + bx + c \tag{A.1}$$

so that c is the DC at the scene center (x=0). In order to transfer the DC to a different scene center $x \mapsto x + s$ the equation

$$ax^2 + bx + c = a'(x+s)^2 + b'(x+s) + c' \qquad \forall x \tag{A.2}$$

must hold for all x. Especially for $x = -s$:

$$c' = as^2 - bs + c \tag{A.3}$$

The other parameters can be found by solving for specific x_1 and x_2:

$$\begin{pmatrix} (x_1 - s) & (x_1 - s)^2 \\ (x_2 - s) & (x_2 - s)^2 \end{pmatrix} \begin{pmatrix} DC(x_1) \\ DC(x_1) \end{pmatrix} = \begin{pmatrix} a' \\ b' \end{pmatrix} \tag{A.4}$$

If scene center is shifted in x and y direction this transformation can be applied twice (first in x- and than in y-direction).

C. Parameters of different SAR processors

Parameter	Gamma-SLC	ESA-SLC
start time [s]	30912.82815	30912.83900
center time [s]	30920.92000	30920.69500
end time [s]	30929.01185	30928.55100
center latitude [°]	-70.8407940	-70.8290000
center longitude [°]	-6.6190150	-6.606000
incidence angle [°]	23.4156	23.4090
doppler centroid (DC) [Hz]	-838.78860	-842.04241
DC range dependency	linear	quadratic
near-range-slc [m]	855576.2755	855646.1985
center-range-slc [m]	874986.7329	875005.2964
far-range-slc [m]	894397.1903	894372.1890
time-of-first-state-vector [s]	30891.00000	30890.00000
state-vector-position-1 [m]	2366452.2781	2372506.1282
state-vector-velocity-1 [m/s]	-6055.4008	-6052.2957
.	.	.
.	.	.
state-vector-position-7 [m]	1997784.4106	2004012.5511
state-vector-velocity-7 [m/s]	-6229.4896	-6226.7873

Table A.4: Excerpt of some parameters originating from the same raw data (ERS-1 track 493, orbit 24028, frame 5085 on 18-02-1996) but estimated slightly different by the two SAR - processors. For the state-vectors only the first component is shown.

Abbreviations

DAR	Doppler ambiguity resolver
DC	Doppler Centroid
DEM	Digital Elevation Model
DInSAR	Differential Interferometric SAR
ERS	European Remote Sensing Satellite
ESA	European Space Agency
FLT	flattened interferogram
GCP	Ground control point
GLAS	Geoscience Laser altimeter System
GPS	Global Positioning System
IceSAT	Ice, Cloud and Land elevation Satellite
InSAR	Interferometric SAR
INT	unflattened interferogram
ISP	Interferometric SAR processor
MLBF	Multilook Bear Frequency
MLCC	Multilook Cross Correlation
MSP	Modular SAR processor
PAF	Processing and Archiving Facility
RAMP	Radarsat Antarctic Mapping Mission
RES	Radio Echo Sounding
SAR	Synthetic Aperture Radar
SLC	Single Look Complex
SNR	Signal to Noise ratio
UNW	unwrapped interferogram

Acknowledgments

My supervisor *Wolfgang Rack* helped me continously and with a lot of patience through every single step of this project. His mentoring not only includes on-the-spot support for all technical questions, but also covers extensive outdoor activities and a thorough introduction into the Austrian way of life. As a supervisor he is absolutely recommandable, and potential applicants can expect, amongst others, a sincere improvement of gardening skills. Thank you very much 'Wulfgäng' for a great experience in New Zealand.

The whole team from *Gateway Antarctica* made me feel welcome right from the beginning. In particular I thank *Bryan Storey* and *Michelle Rogan-Finnemore* for their support and approval of my six months internship. Without the help of *Irfon Jones* I would have spent countless hours more in trying to setup the various Linux systems. This is why I found time to write this thesis in english. I hope that some of the results are of interest for you.

I also thank *Charles Werner* from Gamma Remote Sensing for his support during the processing.

Auf deutscher Seite bedanke ich mich beim evangelischen Studienwerk *Villigst* für die besondere finanzielle Unterstützung des Auslandsaufenthaltes.

Es ist auch eine Freude ein Teil der lustigen Arbeitsgruppe für Glaziologie am Alfred-Wegener-Institut zu sein. Insbesondere bedanke ich mich dabei bei *Christine Wesche* für die Bereitstelllung von IceSAT-Daten und Hilfe bei ArcGIS sowie bei *Daniel Steinhage* für die Eisdicken und die Ideen zum Boxmodell.

Prof. Dr. P. Lemke sowie *Prof. Dr. J. Notholt* danke ich für das Übernehmen der Gutachten.

Sebastian Ruhman, *Adriana Visser* und *Katharina Kubo* haben die mühsame Aufgabe des Korrekturlesens übernommen. Vielen Dank für Eure Vorschläge, und, die Geduld, bei der vermaledeiten, Kommasetzung.

Zum Schluß möchte ich mich bei meinen Eltern *Ute* und *Ulrich Drews* für das ganze Studium bedanken. Ob in Freiburg, Wolfville, Bremen oder Christchurch - ich war eigentlich nie weit weg von zu Hause.

Bibliography

[AB96]   A. Barmettler, P. Pasquali, D.Small D. Nuesch: *Cross-Compatibility of ERS-SLC-Products.* Proceedings FRINGE SAR Interferometry Working Group: 2nd Workshop, Zürich, October 1996.

[AF00]   A. Freeman, W. Johnson, B. Huneycutt R. Jordan S. Hensley P. Siqueira J. Curlander: *The 'Myth' of the minimum SAR antenna area constraint.* IEEE Transactions on Geoscience and Remote Sensing, 38, Jan 2000.

[BS05]   Baek S., Kwoun O., Braun A. Zhong L. Shum C.: *Digital Elevation Model of King Edward VII Peninsula, West Antarctica, from SAR Interferometry and IceSAT Laser Altimetry.* IEEE Geoscience and Remote Sensing Letters, 2(4):413–417, Oct. 2005.

[CW00]   C. Werner, U. Wegmüller, T. Strozzi A. Wiesmann: *Processing strategies for phase unwrapping for InSAR applications.* Gamma Remote Sensing, Technical Report, October 2000.

[CW02]   C. Werner, U. Wegmüller, T. Strozzi A. Wiesmann: *Gamma SAR and Interferometric Processing Software.* ERS-EnviSAT Symposium, Gotheburg, Sweden, May 2002.

[CW07]   C. Wesche, D. Steinhage, R. Drews W. Rack: *Precise surface topography in Dronning Maud Land, Antarctica, based on ground based kinematic GPS measurements,* September 2007. at the International symposium of snow and ice (Moscow).

[Dem04]   Demtröder, W.: *Elektrizität und Optik.* Springer, 2004.

[ESA07]   *ESA:Envisat Product Handbooks, ASAR Product Handbook, issue 2.2,* February 2007.

[GAM06]   *GAMMA Remote Sensing Modular SAR processor (MSP), Documentation - User's guide,* November 2006.

[GR98]   Goldstein R., Werner C.: *Radar interferogram filtering for geophysical applications.* Geophysical Research Letters, 25(21):4035–4038, 1998.

[Han01]   Hanssen, R.: *Radar Interferometry, Data Interpretation and Error Analysis.* Kluwer Academic Publishers, 2001.

[Hei04]   HEIN, ACHIM: *Processing of SAR Data.* Springer, 2004.

[HL01]   H. LIU, K. JEZEK, B.LI Z.ZHAO: *Radarsat Antarctic Mapping Project digital elevation model version 2.* Boulder, CO: National Snow and Ice Data Center. Digital media., 2001.

[IC05]   I. CUMMING, F. WONG: *digital processing of Synthetic Aperture Radar data.* Artech House, 2005.

[JB01]   J. BAMBER, R. BINDSCHADLER: *An improved elevation dataset for climate and ice-sheet modelling: validation with satellite imagery.* Annals of Glaciology, 25:438–444, 2001.

[JB05]   J. BAMBER, J. GOMEZ-DANS: *The accuracy of digital elevation models of the Antarctic continent.* Earth and Planetary Science Letters, 237:516–523, sep 2005.

[JCC91]   JOHN C. CURLANDER, ROBERT N. MCDONOUGH: *Synthetic Aperture Radar.* Wiley Series in Remote Sensing, 1991.

[JD07]   J. DIMARZIO, A. BRENNER, R. SCHUTZ C. SHUMAN H. ZWALLY: *GLAS/ICESat 500 m laser altimetry digital elevation model of Antarctica.* Boulder, Colorado USA: National Snow and Ice Data Center. Digital media., 2007.

[JV03]   JANSSEN V., LINLIN GE., RIZOS CHRIS: *Tropospheric delay corrections for differential InSAR results from GPS observations.* Proc. 6th int. Symp. on Satellite Navigation Technology Including Mobile Positioning and Location Services (Melbourne), July 2003.

[KR96]   KWOK R., FAHNESTOCK M.: *Ice sheet motion and topography from radar interferometry.* IEEE Transactions on Geoscience and Remote Sensing, 34(1):189–200, Januar 1996.

[MC05]   M. CONSTANTINI, MALVAROSA F., MINATI F. ET AL.: *A data fusion technique for Mosaicking of Different Sources Digital Elevation Models.* Fringe 2005 Workshop (Frascati, Italy), November 2005.

[MJ97]   MOHR J., REEH N., MADSEN S.: *ERS Tandem Study of Glacier Dynamics In NE - Greenland.* Proceedings of the 3rd ERS symposium Florence (Italy), March 1997.

[MJ98]   MOHR J., REEH N., MADSEN S.: *Three-dimensional glacial flow and urface elevation measured with radar interferometry.* Nature, 391, January 1998.

[Moh97]   MOHR, J.: *PHD: Repeat Track SAR Interferometry - An Investigation of its Utility for Studies of Glacier Dynamics*, mai 1997.

[RG84]   R. GOLDSTEIN, H. ZEBKER: *Topographic mapping from interferometric synthetic aperture radar observations.* Journal of geophysical research, 91, 1984.

[RG07]   ROTSCHKY G., HOLMLUND P., ISAKSSON E. MULVANEY R. OERTER H.
          VAN DEN BROEKE M. WINTHER J.: *A new surface accumulation map for
          western Dronning Maus Land, Antarctica, from interpolation of point mea-
          surments.* Journal of Glaciology, 2007.

[RR00]   R. ROSEN, S. HENSLEY, I. JOUGHIN F. LI S.MADSEN E. RODRÍGUEZ
          R. GOLDSTEIN: *Synthetic Aperture Radar Interferometry.* Proceedings of
          the IEEE, 88 No. 3, march 2000.

[SK97]   SINGH K., STUSSI N., KEONG K. HOCK L.: *Baseline Estimation in In-
          terferometric SAR.* Third ERS Symposium on Space at the Service of our
          Environment, held in Florence (Italy)., March 1997.

[Sou99]   SOUMEKH, MEHRDAD: *Synthetic Aperture Radar - Signal Processing with
          Matlab Algorithms.* Wiley Interscience, 1999.

[SR93]   SCHARROO R., VISSER P.: *Precise Orbit determination and gravity field
          improvement for the ERS satellites.* Journal of Geophysical Research, 103,
          April 1993.

[TY99]   T. YMANOKUCHI, K. DOI, K. SHIBUYA: *Extracting Grounding Line of the
          Antarctic Ice Sheet from ERS - 1/2 Interferometric SAR Data.* Geoscience
          and Remote Sensing Symposium, 2005. IGARSS '05. Proceedings. 2005 IEEE
          International, 7, June 1999.

[UN05]   U. NIXDORF, D. STEINHAGE, U MEYER L. HEMPEL M. JENETT P.WACHS
          H. MILLER: *The newly developed airborne radio-echo sounding system of the
          AWI as a glaciological tool.* Annals of Glaciology, 29, July 2005.

[Wil95]   WILEY, C.: *Pulsed Doppler Radar Methods and Aparatus*, 1995. United States
          Patent Nr. 3196436.

[WU97]   WEGMÜLLER U., WERNER, C.: *Gamma SAR processor and interferometry
          software.* Third ERS Symposium on Space at the Service of our Environment,
          held in Florence (Italy). Compiled by Guyenne T. and Danesy D., March
          1997.